Electrospun Carbon Nanofiber Electrodes Decorated with Palladium Metal Nanoparticles: Fabrication and Characterization

by

John Paul Kurpiewski

Bachelor of Science in Mechanical Engineering
Columbia University Fu Foundation School of Engineering and Applied Science
May 2003

SUBMITTED TO THE DEPARTMENT OF MECHANICAL ENGINEERING IN PARTIAL FULFILLMENT OF THE REQUIREMENTS FOR THE DEGREE OF

MASTER OF SCIENCE IN MECHANICAL ENGINEERING

at the

MASSACHUSETTS INSTITUTE OF TECHNOLOGY

June 2005

Signature of Author: _____
Department of Mechanical Engineering
May 2005

Certified By: _____
Yang Shao-Horn
Atlantic Richfield Career Development Assistant Professor of Mechanical Engineering
Thesis Supervisor

Accepted by: _____
Lallit Anand
Professor of Mechanical Engineering
Chairman, Department Graduate Committee

Electrospun Carbon Nanofiber Electrodes Decorated with Palladium Metal Nanoparticles: Fabrication and Characterization

by

John Paul Kurpiewski

Submitted to the Department of Mechanical Engineering in May 2005 in Partial Fulfillment of the Requirements for the Degree of Master of Science in Mechanical Engineering

ABSTRACT

A new method was investigated to produce a novel oxygen reduction electrode comprised of carbon nanofibers for use in polymer electrolyte membrane (PEM) fuel cells and metal-air batteries. The process involved electrospinning a solution of polymer (polyacrylonitrile), noble metal salt (palladium (II) acetate), and organic solvent (n,n-dimethylformamide) to fabricate a porous, non-woven, free-standing nanofiber mesh. Through experimentation with multiple variables, the optimal electrospinning parameters were quantified. Post-process heating of the electrospun nanofibers included stabilization in air environment at 280°C for 2 hours, followed by carbonization in grade 5.0 argon environment to temperatures between 800 and 1100 °C for times varying between 1 minute to 1.5 hours. The carbonization step served the purpose of converting insulating polymer into conductive amorphous carbon and precipitating nanoparticles of palladium in a homogeneous distribution throughout the electrode. The electrode was characterized using scanning electron microscopy (SEM), x-ray diffraction (XRD), transmission electron microscopy (TEM), microprobe station, and x-ray adsorption near edge structure (XANES). Electrochemical performance was characterized using cyclic voltammetry (CV), rotating disk electrode (RDE), and testing in a PEM fuel cell. It was demonstrated that palladium crystal size and particle size increased with heat treatment time and temperature. Lower concentrations of PAN in solution had the effect of thinner nanofibers (100-400nm diameters), which led to faster particle growth. Particle sizes were often distributed in a bimodal Gaussian distribution, centered around values on the order of 10nm and 100nm. In-situ TEM allowed for particle formation and growth to be investigated. Cross-sectional TEM showed that particle nucleation occurred within the fibers. Electrodes were spun as thin as 7 microns, and contained no significant amounts of graphite or palladium oxide. Electrochemical surface area was 7.17 m^2/g catalyst, and the performance was comparable to commercially available E-TEK electrodes on a catalyst cost per power basis. It was shown platinum salts worked well in the process, allowing platinum electrodes to be fabricated.

Thesis Supervisor: Yang Shao-Horn
Title: Atlantic Richfield Career Development Assistant Professor of Mechanical Engineering

ACKNOWLEDGEMENTS

The research findings presented in the following pages would not be possible without the financial assistance of The Deshpande Center for Technological Innovation's MIT Deshpande Ignition Grant 2003-2004 and the Office of Naval Research's Award No. N000140410400 2004-2007.

The author would like to thank Academic Research Advisor Yang Shao-Horn for her direction and guidance on the project, as well as securing funding for the research and having me as part of the first graduating class of the Electrochemcial Energy Lab (EEL) she founded and directs. I am very thankful for the time Professor Shao-Horn has taken to advise this research and to review this thesis, and help me become a better experimentalist and technical writer.

Much credit is due to Simcha Singer, who assisted throughout the second year of this project. The results presented on the analysis of RDE in oxygen-saturated solutions were the fruits of his efforts. Simcha was also instrumental in executing sample heat treatments, investigating literature background on RDE, assisting in electrospinning, and conducting general lab labor.

I am extremely appreciative of the help from Dr. Quinn Horn regarding his advice on experimentation, for his additional microscopy efforts, and for formatting and drafting the manuscript on this work that is being submitted for publication. His role in the patent application was instrumental.

I would also like to thank Jungik Kim for his help in operating the H_2/O_2 PEM fuel cell and reporting results on the performance of my fuel cell electrodes in a functional MEA.

Elisa Alonso has earned her recognition here through her hard work during the summer of 2003, laying the foundation for my efforts on this endeavor. She constructed the electrospinning setup before I arrived at MIT, and had some of the first electrospinning results on pure carbon nanofibers.

I am very thankful for the help of G.J. LaO on the TEM during my first months with the group before I received training, as well as his assistance during the in-situ TEM experiments.

I thank Dr. Paulo Ferreira, a visiting professor from the University of Texas at Austin for taking his time to image the electrode under high-resolution TEM.

Other members of the scientific community who had input on this research were Dr. Kevin White from Physical Sciences, Inc (Andover, Massachusetts) on experimental setup, Dr. Azzam Mansour of the Naval Warfare Center for his work with XANES, Professor Bora Mikic for his expertise with the heat transfer calculations on the lab tube

furnace, and Professor Ahmed Ghoniem for his advice regarding fluids and mass transfer modeling in fuel cell systems.

Special thanks goes to the members of the I-teams group who are working to commercialize the technology presented in this thesis. Their efforts resulted in winning the $1K competition and placing second in the MIT $50K competition. Nanocell's Board of Directors includes:

Art Goldstein, Business Plan Advisor & $50K Mentor,
Chairman and CEO (Retired), Ionics, Inc.
David Gammell, Legal and Intellectual Property Advisor, Partner, Brown Rudnick
Norman Strate, Market Advisor, Past President & CEO, Protonex
Krisztina Holly, Strategy Advisor, Executive Director, Deshpande Center

The Nanocell team members are:

Jeff Baer, President (Acting)
Dr. Yang Shao-Horn, Chief Technology Officer
Ian MacDonald, Chief Operations Officer
Howard Tang, Chief Financial Officer (Acting)
Dr. Jin Yi, V.P. of Engineering
Brett Prince, V.P. of Sales (Acting)
Matt Ziskin, V.P. of Marketing (Acting)
J.P. Kurpiewski, Director of Technology Development

Beyond those who directly worked on the nanofiber project were my labmates who assisted in other aspects of our small community. My gratitude for making the EEL a memorable experience goes to: Anjuli Appapillai, Anne Clemencon, Ethan Crumlin, Markus Duelks, Manolis Kasseris, Sundeep Kumar, and Bilge Yildiz. I doubt I'll have the opportunity again to work with such a talented group of people from such vastly different backgrounds.

Looking fondly back upon my time at Columbia, there are several people I am forever indebted for making my experience at The Institute a reality. Most prominent among them is Prof. Luc Frechette, who served as my academic advisor, research advisor, SAE advisor, and professor of Heat Transfer and ME Lab II. Without his guidance and teachings, I would not have been prepared for the challenge ahead. My gratitude is for the entire faculty of the Mechanical Engineering department professors at Columbia, in particular Professor Vijay Modi, Professor Rene Chevray, Professor Jeff Kysar, Professor Gerard Ateshian, Professor Lawrence Yao, and Professor Scott Barton (Chem. E.) for creating a small community that nurtured its students, encouraging learning and balance, and conveying the fundamentals of engineering that helped me succeed. "In lumine tuo videbimus lumen." I also thank my good friend Veru Narula for always being there and keeping in touch all these years, and Evangeline Geskos for being one of the best listeners I know.

From the first week arriving at MIT until the walk down the aisle at graduation and hopefully long afterwards, there have been many people close to me who I've had the pleasure of knowing through MIT. They gave me their friendship, their hearts, their inspiration on "p-sets", and their precious time in the past two years when I needed it most. I thank you for your friendship.

Thank you, Heather, for making me smile and being such an important part of my life through the Boston seasons. You taught me the value of life and other lessons that are not found in any textbook or assignment.

Last and most importantly, I would like to thank my family for their enduring love and strong emotional support. Of everyone mentioned here, you were the most important in seeing me through. For what you gave, I owe you the most, but you always ask for the least in return.

TABLE OF CONTENTS

LIST OF FIGURES

LIST OF TABLES

1 INTRODUCTION

1.1 Energy

Energy is a scalar quantity associated with a state of one or more objects, and is defined as the ability to do work. It exists in numerous forms throughout the universe, and is a requirement of life. Energy can be categorized into two main types: Kinetic energy, associated with the state of motion of an object, or potential energy, a stored form associated with the configuration of a system of objects that exert forces on one another [1].

Further categories can be distinguished. Nuclear energy is potential stored in the binding forces of subatomic particles in the nucleus of an atom. Thermal energy, or heat, is the collective potential and kinetic energies associated with random motions of atoms and molecules. Sound energy is present in the motion of waves through a medium. Mechanical energy is a form of potential energy stored in springs. By lifting a mass, work is done against gravity, and the mass gains gravitational potential energy. Electrical energy is defined by the position of an electric charge in an electromagnetic field [2]. Chemical energy is stored in bonds between atoms of a molecule.

Energy is often stored and distributed to later be converted at locations where in demand. Currently, the most popular sources of energy in the US are fossil fuels, as seen below in Table 1-1. Fossil fuels contain energy in a chemical form, with distribution often in the form of electrical energy through transmission lines.

Table 1-1: Projected US Energy Consumption by Source for the year 2003. Data published in the Annual Energy Review by the Energy Information Administration [3].

Category	Energy Source	Consumption (Bil BTU)
Fossil Fuels	Coal	22,707,069
	Coke Net Imports	50,518
	Natural Gas	22,506,690
	Petroleum	39,074,104
	FOSSIL FUELS TOTAL	**84,338,381**
Nuclear Electric Power		7,972,521
Hydroelectric Pumped Storage		-87,606
Renewable Energy	Conventional Hydroelectric Power	2,779,495
	Wood, Waste, Alcohol	2,883,960
	Geothermal	314,235
	Solar	63,412
	Wind	108,434
	RENEWABLE ENERGY TOTAL	**6,149,537**
Electricity Net Imports		21,896
ENERGY CONSUMPTION TOTAL		**98,155,587**

In 2003, the energy stored in the bonds of chemicals and materials such as crude oil, natural gas, wood, waste, and alcohol accounted for 8.7222×10^{16} BTUs (or 88.9%), out of the 9.8155×10^{16} BTUs of total energy consumption for the US [3]. Poor energy conversion efficiency leads to increased economic costs, waste of resources, and negative environmental impacts, such as increased greenhouse gasses and pollutants. Thus, efficient large scale chemical energy storage and conversion is a key issue for the functionality of society and the US economy.

On a smaller scale, the use of portable electronics continues to have growing impact on society. Commercial applications include laptops, hand-held computers, personal digital assistants (PDAs), digital cameras, video recorders, portable music devices, and cell phones. Military applications include handheld global positioning systems (GPS),

tactical radios, and other communication devices. The importance of portable, long-lasting energy cannot be understated. The worldwide market for rechargeable battery packs (lithium-ion, lithium-polymer, nickel-metal hydride, and nickel cadmium) for portable devices is expected to reach 1.1 billion units in 2005, with the majority of sales being for cell phones. Lithium-ion batteries are the most popular type, with output expected to grow from 664 million units in 2005 to 1.2 billion units in 2010 [4]. The developmental technology of micro fuel cells, which has the potential to exceed lithium-ion performance, was forecasted in 2003 to be 463.8 million unit sales by 2009, if the right price points could be achieved [5]. Much like large scale energy conversion systems, small scale energy storage systems have a broad social impact and require efficient chemical energy conversion.

1.2 Energy Conversion

The two main pathways of chemical energy conversion to useful work are through heat engines or electrochemical devices. Examples of heat engines (and the cycles they operate) are: Gas turbine power plants (Brayton cycle), automobile engines (Otto cycle), truck and rail engines (Diesel cycle), and steam turbine power plants (Rankine cycle). Heat engines convert the chemical energy in gasoline, coal, oil, or biomass into heat, and then transform the heat into mechanical work. The mechanical work is generally used as shaft work or to drive an electric generator. A schematic of a heat engine is shown below in Figure 1-1.

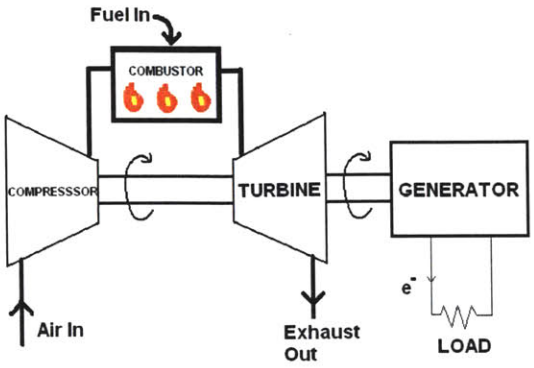

Figure 1-1: Schematic of a gas turbine heat engine that converts chemical energy to heat, which drives the turbine to produce shaft work that is converted to electricity.

Dictated by the second law of thermodynamics, all heat engines are limited by the Carnot efficiency:

$$\eta_{Carnot} = \eta_{thermal} = \frac{W_{out}}{Q_{in}} = 1 - \frac{T_L}{T_H} \tag{1.1}$$

where $\eta_{thermal}$ is the thermal (Carnot) efficiency, W_{out} is the work output, Q_{in} is the heat input, T_L is the system's absolute low temperature, and T_H is the heat engine's absolute high temperature. The system's low temperature is often fixed by the surrounding environment. This indicates for maximum efficiency, T_H must be as high as possible, limited by fuel flame temperatures or material properties. Heat engines require appropriate insulation, heat flow management, and safety engineering to operate under high temperature conditions.

In contrast to heat engines, electrochemical devices, such as batteries and fuel cells, convert chemical energy directly to electrical energy, avoiding the losses that occur in heat engines from the chemical-thermal-mechanical-electrical conversion. The efficiency of an electrochemical cell is given as follows:

$$\eta_{electrochem,\max} = \frac{W_{\max}}{Q_{in}} = \left| \frac{\Delta G_r}{\Delta H_r} \right| \tag{1.2}$$

where W_{max} is the maximum work output, Q_{in} is the heat input, ΔH_r is the enthalpy change per mole of reactants in the reaction. ΔG_r is the Gibbs free energy per mole reactants, and is defined as:

$$\Delta G_r = \Delta H_r - T\Delta S_r = -n_e F \varepsilon_r \tag{1.3}$$

where T is the temperature of the reaction, ΔS is the change in entropy, n_e is the number of moles of electrons, F is Faraday's constant, and ε_r is the electric potential. Plugging in Equation (1.3) into (1.2), the efficiency simplifies to:

$$\eta_{electrochem,\max} = \left|\frac{\Delta G_r}{\Delta H_r}\right| = \frac{\Delta H_r - T\Delta S_r}{\Delta H_r} = 1 - \frac{T\Delta S}{\Delta H_r} \tag{1.4}$$

In Equation 1.4, it can be assumed that the enthalpy of reaction, ΔH_r, and the entropy change, ΔS, are more or less constant for the hydrogen/oxygen (H_2/O_2) reaction of a typical fuel cell [6]. Plotted below in Figure 1-2 is a comparison between the theoretical maximum efficiencies for H_2/O_2 fuel cells and heat engines.

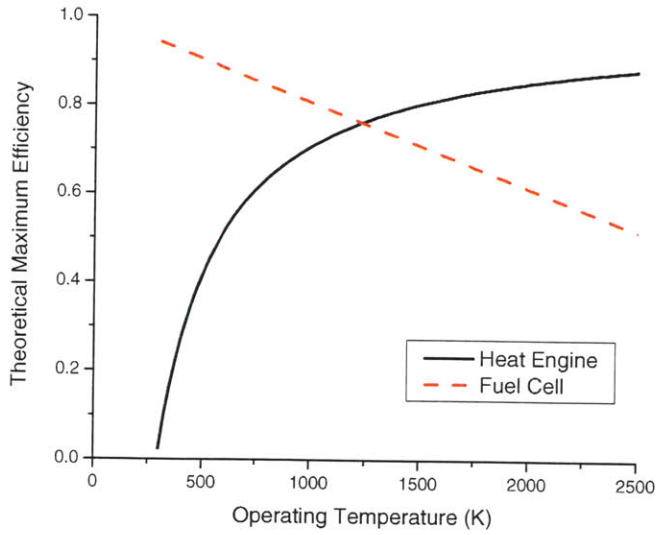

Figure 1-2: A comparison of the theoretical maximum efficiencies as a function of operating temperature for a heat engine and a H_2/O_2 fuel cell given ambient temperature of 300K (27 °C) and fuel cell exhaust in steam form.

It is clear from Figure 1-2 that at temperatures between 300 K (room temperature, 27°C) and 1225 K (952 °C), where the lines intersect, a fuel cell's efficiency is superior to that of a heat engine. Lower operating temperatures closer to room temperature allow the discrepancy to be quite large. It should be noted that these efficiencies are theoretical, and not realized.

1.3 Electrochemical Cells

There are four basic components to an electrochemical circuit: Two electrodes (the anode and cathode), electrolyte, and external load. The two electrodes are typically made of metals, semiconductors, or composites of both. A schematic of an electrochemical cell is shown below in Figure 1-3. The chemical energy contained in the active materials is converted to electrical energy directly by means of an oxidation-reduction (redox) reaction. As diagrammed in Figure 1-3, during discharge, oxidation, or the loss of electrons, occurs at the anode. Reduction, or the gain of electrons, occurs at the cathode. The circuit is completed by the flow of ions through solution and electrons through the external load.

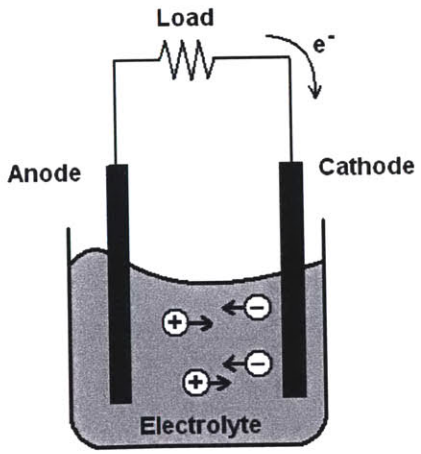

Figure 1-3: Schematic of an electochemical cell discharging and converting chemical energy directly to electricity. Electrons travel from the anode to the cathode through the external circuit and load. The negatively charged ions (anions) flow from the cathode to anode in solution. The positively charged ions (cations) flow from the anode to the cathode. In the case where the cell is charged to store energy, the load is replaced by a voltage source.

The two main categories of electrochemical devices are batteries and fuel cells.

1.3.1 Batteries

Batteries are closed systems with a finite amount of energy stored chemically in an encasing. When a typical battery, or primary cell, is connected to a resistance, an internal chemical reaction forces a current to flow by establishing an electric potential across terminals of the battery. The reaction will continue until the reactant species are depleted. In a rechargeable battery, or secondary cell, the battery undergoes the reverse process during charging and electrical work is transferred into the battery when the chemical reactions are reversed.

There are many classes of primary batteries based on their chemistry. These include, but are not limited to: Zinc-carbon, magnesium and aluminum, alkaline-manganese dioxide, mercuric oxide, silver oxide, zinc-air, lithium, and solid electrolyte batteries. Some secondary batteries include, but are not limited to: Lead-acid, iron electrode, zinc-air, nickel-cadmium, nickel-zinc batteries, and the commercially popular lithium-ion.

In industry, zinc-air electrically rechargeable systems are very attractive because of zinc's high theoretical energy density. Zinc is relatively stabile in alkaline electrolytes and is the most active metal that can be electrodeposited from an aqueous solution. Higher energy density, flat discharge voltage, long shelf life, environmental friendliness, reasonable cost, and capacity independence from load and temperature are all characteristics that make the zinc-air cell attractive [7].

Zinc-air cells are commonly used in miner's lamps, hazard warning lights, off-shore markers, lighted buoys, navigation aides, railway signal installations, remote places where A/C power is unavailable, and hearing aides. They can easily be made compact and spill-proof and are best at applications that require a slow, steady drain [8].

However, problems exist with dendrite formation, non-uniform zinc distribution, water management, and most importantly, poor air electrode performance [7].

1.3.1.1 Conventional Metal-Air Battery Oxygen Reduction Electrodes

The half reaction at the cathode of a Zn-air cell is:

$$O_2 + 2H_2O + 4e^- \rightarrow 4OH^- \tag{1.5}$$

The oxygen reduction reaction that occurs in Equation 1.5 can result from either of two pathways: The direct 4-electron pathway, which follows Equation 1.5, or the less efficient, two electron peroxide pathway, as shown in Equation 1.6.

$$O_2 + H_2O + 2e^- \rightarrow HO_2^- + OH^- \tag{1.6}$$

The reaction in Equation 1.6 is either followed by the reduction of peroxide or the decomposition of peroxide, to result in the final products of Equation 1.5. Oxygen reduction is a multielectron process that may involve a variety of elementary steps including series and parallel paths. Due to the complexity, the rate of reaction is generally sluggish and can be expressed as follows:

$$i = k\left[P_{O_2}\right]^n\left[H^+\right]^m \exp\left(\frac{-\alpha FE}{RT}\right) \tag{1.7}$$

Equation 1.7 assumes the generalized rate-determining step is the first electron transfer, and that i is the current density, k is the reaction constant, $[P_{O2}]$ is the partial pressure of oxygen, $[H^+]$ is the concentration of protons, n and m are the reaction orders, α is the symmetry factor (usually 1), F is Faraday's constant, R is the universal gas constant, and T is the temperature of solution [9].

The air cathode must be engineered well to reduce the effects of the sluggish reaction and address water management. Typically, the air cathode of a conventional zinc-air cell is made of porous carbon, nickel mesh to conduct electrons and give structural stability, and occasionally a less expensive catalyst such as manganese. A conventional air cathode is constructed of sheets and usually has multiple layers. A carbon layer, nickel metal mesh, a second carbon layer, and a Teflon layer are laminated together to form the cathode, as

shown in Figure 1-4 and Figure 1-5. Non-woven carbon fibers are prepared as active layers by dipping them in a slurry of catalyst. The nickel metal mesh provides structure and acts as a conductor to siphon the electrons. Teflon films or coatings assist in water management by acting as a hydrophobic layer.

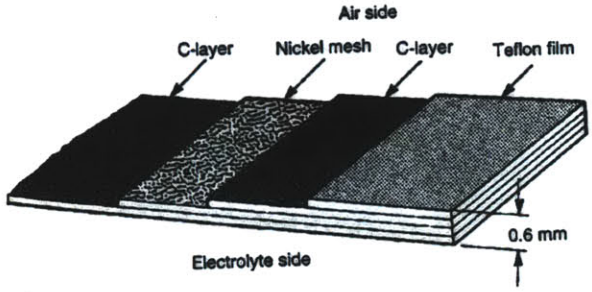

Figure 1-4: Schematic of the layered, laminated air cathode of a metal-air cell. Figure from the Handbook of Batteries [7].

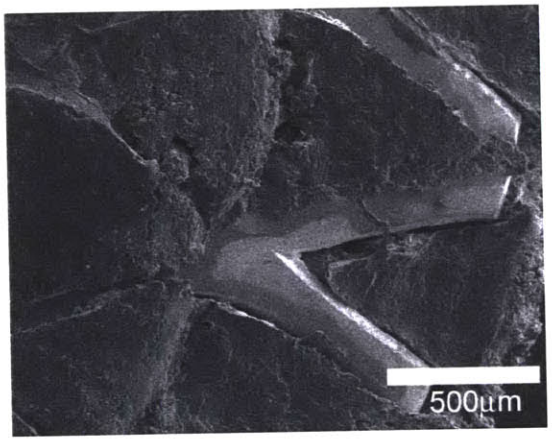

Figure 1-5: Scanning electron microscope (SEM) image of a nickel metal mesh sandwiched by two carbon layers, comprising an air cathode in a 1.4V Renata ZA 675 commercial zinc-air cell.

There are several disadvantages to the metal air cell resulting from the cathode performance. The cell is very sensitive to the environmental conditions. Water management issues are problematic for extended cell life. The effect of humidity on a zinc-air cell is illustrated below in Figure 1-6.

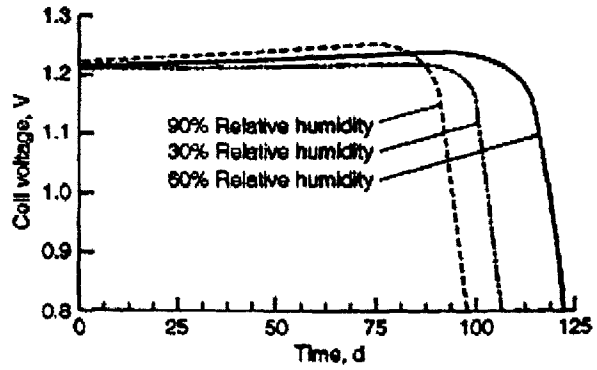

Figure 1-6: Plot of cell voltage vs. time demonstrates the affect of relative humidity on the zinc-air cell. Environmental sensitivity is a major obstacle. Figure found in the Handbook of Batteries [7].

Power is limited by the flooding or the drying of the cathode. Catalyst degradation due to poisoning is a performance limiting occurrence as well. Hydrogen may be produced at the anode, causing the cell to crack open or explode. The cell is limited to operation at low temperatures. In addition, the battery needs to be entirely replaced when discharged. Fuel cells address some of these issues.

1.3.2 Fuel Cells

A fuel cell is an electrochemical energy conversion device that functions similarly to a battery. The difference between a fuel cell and a battery is that generally, the reactants in a fuel cell are passed over the electrode by use of ducts and/or channels, thereby making the fuel cell an open system. Sometimes in large scale fuel cell design, pumps, heat exchangers, and water management systems may be implemented. The fuel is generally stored in a tank separate from where the reaction takes place. In contrast, a battery is a closed system in a sealed container that holds a specific amount of reactant. Simply, a battery is an energy storage device while a fuel cell is an energy conversion device with external energy storage capabilities. Fuel cells are easily kept running by the replacement of the fuel cartridges or whatever methods are required to maintain fuel flow over the electrodes. With a continuous flow of reactants, a fuel cell will last as long as it structurally is able.

There are many types of fuel cells that operate over a wide range of temperatures and on a variety of fuels for distinct applications. These are generally classified by the electrolyte used. Some examples are: Polymer electrolyte membrane (PEMFC), alkaline (AFC), phosphoric acid (PAFC), molten carbonate (MCFC), and solid oxide fuel cells (SOFC) [10]. One of the most popular and promising types of fuel cells is the polymer electrolyte membrane (PEM) fuel cell. It is sometimes referred to as proton exchange membrane. The PEM cell chemically combines hydrogen and oxygen or air to form water. Due to low operating temperatures around or below 100 °C, there are no NO_x or SO_x emissions. A PEM schematic is shown below in Figure 1-7.

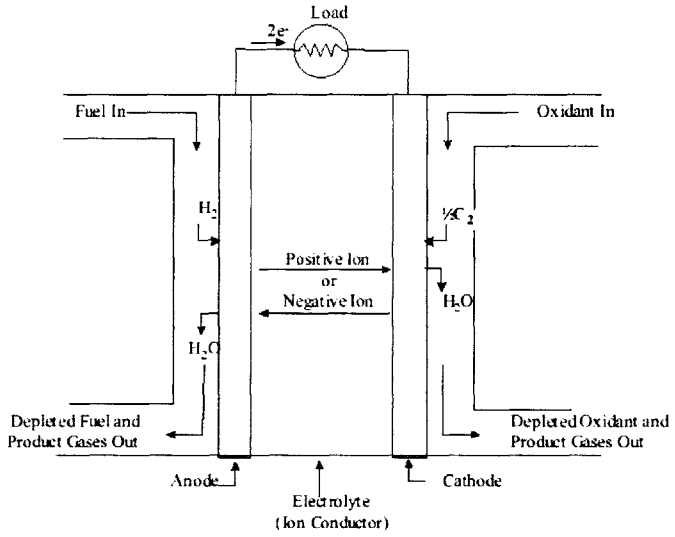

Figure 1-7: Schematic of a PEM fuel cell with electrodes and species flux detailed through channels, electrodes, and electrolyte [10].

In a PEM fuel cell, the chemical activity and energy conversion occurs in a group of layers called the membrane electrode assembly (MEA). The MEA consists of the following layered arrangement in order: Anodic gas diffusion layer (GDL), anodic catalyst layer, polymer electrolyte, cathodic catalyst layer, and cathodic GDL. Hydrogen fuel enters the cell through channels and flows over the GDL and catalyst layer that comprise the anode. The GDL, made of carbon paper or carbon cloth, serves as a porous current collector and distributes gas evenly across the electrode. Typically, catalyst layers are made of "carbon black", which has nanoparticles of the catalyst platinum (<10nm) on larger carbon nanoparticle supports (~100nm). A triple phase boundary is

formed at the surface of the solid catalyst, gaseous hydrogen, and liquid water with the electrolyte. Here, all three phases are required for the half reaction of oxidation of hydrogen.

On the surface of the catalyst, hydrogen breaks apart, and protons conduct across the polymer electrolyte. The polymer-based layer not only serves the function of proton conducting, but also as a gas separation barrier between the oxygen and hydrogen. For the past 30 years, DuPont™ Nafion® membranes and dispersions have been the polymer electrolyte of choice for the fuel cell industry [11]. Nafion serves as a good proton conductor when saturated in water, and a comparably durable material. Protons are conducted to the cathode, where they combine with atomic oxygen and free electrons to form water.

1.3.2.1 PEM Oxygen Reduction Electrodes

Oxygen or air flows over the cathodic GDL and catalyst layer, resulting in the following half reaction:

$$O_2 + 4H^+ + 4e^- \rightarrow 2H_2O \tag{1.8}$$

At the cathode in a PEM cell, an oxygen molecule is broken down and reduced. The half reaction described in Equation 1.8 has many steps and is more complex than the anode reaction. Therefore, catalyst loadings on the cathode are typically much higher than the anode to compensate. Much like the oxygen reduction process achieved in metal-air cells, this reaction is complex and sluggish, and requires engineered electrodes to be optimized.

A "good" electrode structure is one that can maximize active surface area per unit mass of the electrocatalyst, minimize barriers to reactant transport, and give relatively constant current output over time. Constant output at a steady voltage requires structural, mechanical, chemical and dimensional stability for the electrode. The proton exchange membrane must conduct protons well, but contain mass transfer of reactants and be electrically isolating. The required functions of an electrode in order to have optimal

operation are: high proton conductivity; immobilized anions; insolubility of membrane in water; solubility of water in membrane; impermeability to H_2 and O_2 crossover; swift water transport; reversible hydration; dimensional, chemical, and electrochemical stability during operation; thermal stability; and tolerances to impurities [12]. An ideal electrode is shown below in Figure 1-8.

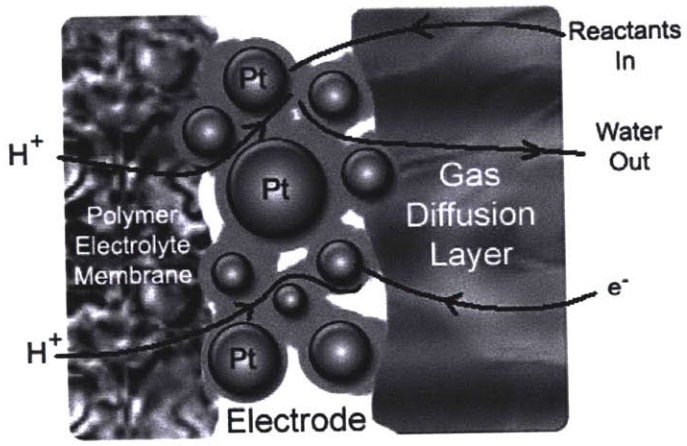

Figure 1-8: Diagram of an idealized electrode showing electronic, proton, and water pathways required for optimal performance of a PEM fuel cell.

Carbon from platinum black and the GDL serve as electron conductors. If carbon particles are not in contact with one another or the structurally-reinforcing GDL, the reaction is limited because electrons are prevented from flowing through a complete circuit. Alternatively, if the particles become imbedded in the Nafion, oxygen transport will be impeded and the reaction rate will decrease. Another cause of reaction rate decrease is the flooding of the electrode, when transport of water away cannot be accomplished fast enough.

The conventional method for preparing a PEM MEA is described as follows. Pre-catalyzed carbon particles known as "platinum black" function as the catalyst. A slurry is prepared of the tiny platinum black particles, added to a ~15% wt Nafion or PTFE solution. The slurry can be brushed onto a Nafion membrane to make a catalyst coasted membrane (CCM) or on the gas diffusion layer to make a catalyst coated substrate (CCS). The gas diffusion layer is typically comprised of carbon cloth or carbon paper. After the platinum black is brushed, the Nafion membrane, catalyst particles, and gas

diffusion layer are hot pressed at a temperature much lower than the thermal degradation point of Nafion and closer glass transition phase where Nafion flows (~150°C). Nafion is thermally and electrochemically stable at temperatures up to 280 °C, making it a good material for fuel cell applications [13]. However, heating Nafion much higher than 150 °C results in some loss of water retention properties. Therefore, typical procedures call for hot pressing at pressures on the order of 5000-15000 kPa at 120-160 °C for ~1-5 minutes. Nafion is often hot pressed when wet, a process known as steam pressing [12].

The process of brushing platinum black has the adverse effect of encapsulating some of the carbon particles in ionomer and electrically isolating them from the gas diffusion layer and current collector. These isolated particles block the flux of ions to the electrodes, thus increasing relative internal cell resistance, or ohmic overpotential. In addition, they are rendered useless and waste expensive catalyst.

1.3.2.2 Economics and Catalyst Efficiency

Fuel cell technology is more expensive than metal-air battery technology because more expensive catalysts are used. The Gemini space program, with a capable budget, exhibited some of the first applications of PEM fuel cells. In the early stages of fuel cell development, palladium was utilized as an electrocatalyst, but was replaced eventually by platinum. Platinum metal was bonded to a gold screen with polytetrafluoroethylene (PTFE) [9]. The use of platinum and gold provided steadier electrode performance and exhibited less corrosion at higher temperatures, but increased cost. Noble metal loadings as high as 35 mg/cm^2 could be found in the space program's fuel cells.

Today, loadings of 0.1 to 0.4 mg Pt/cm^2 are typically found in electrodes, but fuel cells are still not economically superior. Ongoing research on the use and modeling of alternative, low-cost catalysts is being performed, however, there are no substitutes for platinum that have better activity at this time [14]. The bid price of platinum in September, 2004 was $832.00 per troy ounce (as compared with gold, whose bid price is $401.50 and palladium, which is $206.00 per troy oz.) [15]. From this data, and assuming

the best case where the loading is 0.1mg/cm^2, the cost per unit area follows to be around \$0.00267/cm^2. This number sounds quite innocuous, however, a typical fuel cell for a small car has a large electrode area, with stacks of MEA's coated with platinum on both sides. Thus, the cost of the platinum in a fuel cell stack for an automobile is on the order of thousands of dollars.

The US Department of Energy (DoE) set a cost goal at 30 USD/kW for fuel cells to be competitive with internal combustion engines in the transportation sector. However, current technologies place fuel cell stack costs at around 100 USD/kW. It is clear from Figure 1-9 that higher-performing, more economical solutions must be found for future fuel cells to be competitive.

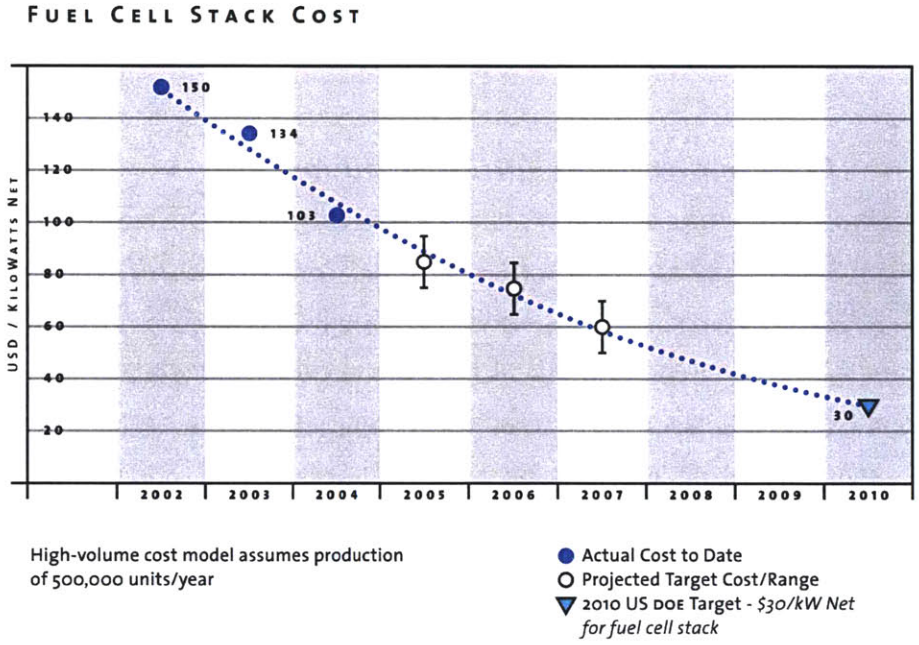

Figure 1-9: Plot of projection of transportation fuel cell stack cost reduction as a function of time in years with present technology and DOE goal noted. Published by Ballard Power Inc. [16]

As shown in Figure 1-10 below, the MEA makes up 84% of the cost in a fuel cell stack. It is this component where cost-reduction engineering is most effective. A strong research effort is underway to cut costs by lowering the amount of noble metal catalyst

required for the electrode by using less metal or optimizing the surface area to have greater activity per unit weight. Moreover, it has been studied that if the automotive market were to convert to fuel cell vehicles, the demand in platinum would rise greatly, driving the cost of platinum higher [17]. The necessity for cheaper electrodes that use less platinum yet exhibit higher performance is evident.

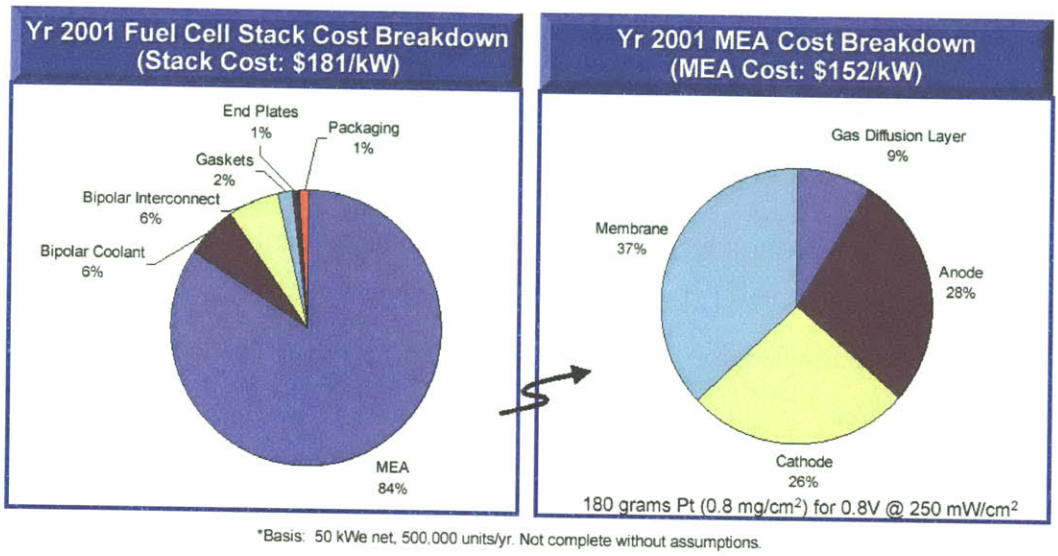

Figure 1-10: TIAX, LLC. report on the breakdown of the individual costs of an MEA are shown on the right, demonstrating the dominance of the MEA in manufacturing costs compared to the rest of a fuel cell stack [18].

The efficient use of catalyst in terms of active surface area per unit weight is motivated by economics and is critical for cheaper fuel cells. One method of characterizing the efficient use of catalysts is by determining the physical surface area (SA) per unit weight of catalyst. The surface to volume ratio for a sphere is given as:

$$SA = \frac{\frac{4}{3}\pi r^3}{\rho 4\pi r^2} = \frac{6}{\rho d} \tag{1.9}$$

where ρ is density of catalyst.

Calculation of the effective area of the catalyst can be accomplished by testing in electrochemical experiments to find active electrochemical area (ECA). This can be

determined by cyclic voltammetry (CV), a measure of current as voltage is cycled between high and low values. The analysis of the area beneath hydrogen adsorption/desorption peaks of the CV plot yields the active area. Further details of CV experiments can be found in later discussions. It should be noted at around 1nm diameter or less, a platinum particle loses its metallic properties and activity decreases. A typical mass specific area is 70 m^2 per gram Pt [12].

Another quantity to characterize catalyst efficiency is the weight ratio of catalyst to support, often abbreviated as "the Pt/C ratio." This method does not indicate the catalyst activity and characterizes on a weight basis and not area. Typical commercial catalysts have Pd/C ratios around 50% [12]. A third variation on catalyst efficiency is to calculate the ECA to weight carbon ratio. This improves upon the Pt/C ratio because takes into account the active area.

It should be noted that although active catalyst ECA is important, mass transfer effects might be to blame for poor electrode performance at high current densities. In addition to higher surface area per unit weight catalyst, some characteristics of an electrode that would improve upon current MEA technology are higher porosity, reduction of overpotentials, and ease of fabrication in large quantities.

1.4 Problem Statement

It has been demonstrated that there is a clear need for more efficient, large-scale energy conversion and higher performance portable energy. The major disadvantages to using heat engines are the limitations of the Carnot efficiency and the problems associated with high temperatures, such as environmental impacts and safety. On the small scale, the growing portable electronics market has increased the demand for longer-lasting, higher-power energy storage devices. Theoretically, fuel cells and micro fuel cells have a distinct advantage over existing technology, however, in practice there are many complications to implementation and market entry. Zinc-air batteries posses high energy densities, but suffer from slow reaction kinetics and water management issues. PEM fuel

cells have similar difficulties, and show a strong need for more efficient use of noble metal catalysts to make them more economical. For both batteries and fuel cells, there is a clear need for a cheaper oxygen reducing electrodes that perform on par or better than current technology. Utilizing the process of electrospinning to fabricate electrodes has the potential to solve many of these technical challenges.

2 ELECTROSPINNING

2.1 Principles of Electrospinning

Electrospinning is a process that creates polymer nanofibers in a non-woven fashion as shown in Figure 2-1a. Numerous tiny fibers with diameters on the order of hundreds of nanometers overlap one another to form a porous material with very high surface area per unit weight.

Because of its high surface area, the structure serves as an ideal support for catalysts to form an electrode, as well as functioning as a gas diffusion layer due to its porosity. Electrically conductive fibers serve as direct pathways from the catalyst particles to current collectors and lack point contacts that would increase electrical resistance.

The functioning principle behind electrospinning involves the use of a strong electric field, to draw a polymer solution into a jet as diagrammed in Figure 2-1b. The use of electric fields to produce fine fibers has been well documented for over 70 years. The first patent on using electrically charged liquids to produce fine fibers was published in 1934 by Formhals [19]. The first paper containing the phrase "electrospinning" was published in 1995 [20], however, prior to this the technique was called "electrostatic spinning". Electrostatic spinning is mentioned in several papers starting in 1975 with *Fundamentals of Electrostatic Spinning* by Dogu [21].

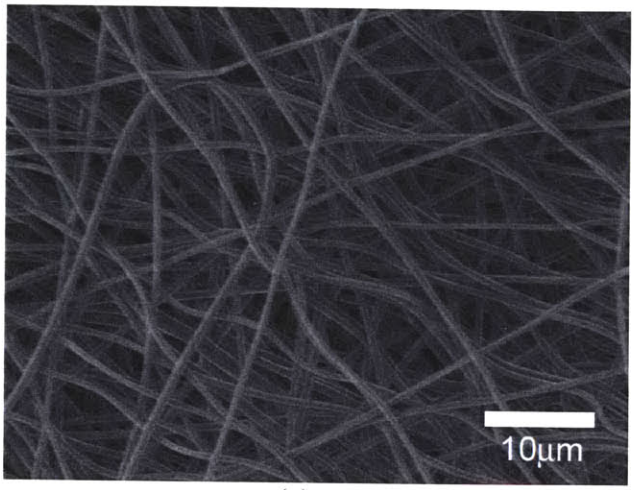

(a)

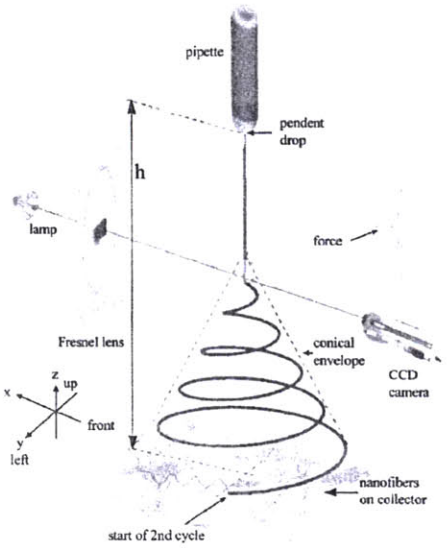

(b)

Figure 2-1(a,b): (a) SEM image of electrospun carbon nanofibers. (b) Electrospinning setup diagram showing onset of whipping pattern in a conical spray with collection on a substrate [22].

As the polymer solution moves through the electric field, the solvent evaporates, leaving a charged fiber. Earnshaw's theorem, demonstrated in Figure 2-2, states that point charges in a straight line are not in equilibrium [23]. The total lateral force is given by the following equation:

$$F = 2\,F_C\,\mathrm{Cos}\,(\theta) \tag{2.1}$$

where θ is the angle of the force vector from a point charge as diagrammed in Figure 2-2, and is valid for large angles. The forces between point charges on the fiber repel and are driven out of the linear configuration. This causes violent whipping of the fiber within the electric field, much like a lasso at very high speeds. The motion causes the fiber to become stretched and the diameter shrinks dramatically [24]. The fiber is collected at the negative terminal of the field, which is usually ground. Fibers fall in random directions in the uniform field, resulting in a non-woven mesh. The "spinning" in the word "electrospinning" is deceptive, as the plates and terminals do not rotate.

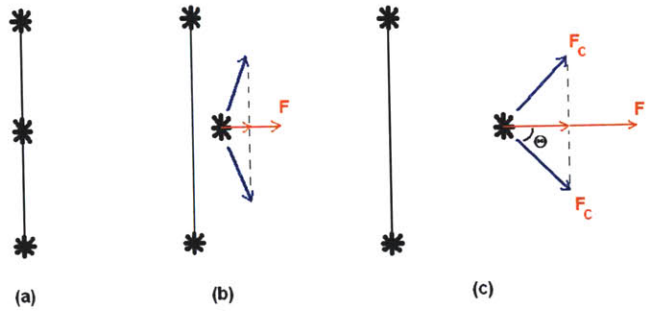

Figure 2-2 (a-c): Earnshaw's theorem proving point charges represented as stars on a straight line are not in equilibrium. Given an initial configuration of point charges in a line (a), and the slight disturbance of one of the charges out of the line (b). Repulsive forces act increasingly, driving the charge out of the line further in (c). As the point charge moves outwards, θ decreases and the force increases.

A phenomenon known as "Ralyleigh instability" occurs along fluid materials that create large beads or imperfections along the fiber. More on the modeling of this complex phenomena can be found in literature [25-27].

2.2 *Experimental Detail*

Much of the progress made in the field of electrospinning was reported by the Reneker group at the University of Akron in Ohio. The 1995 paper titled *Electrospinning Process and Applications of Electrospun Fibers* is the first example of a publication on the subject by the researchers at Akron's Department of Polymer Science [20]. In the experiment, a single charged capillary was used, with a metal mesh as the deposition substrate. A fiber diameter range of 50 nm to 5 microns was achieved, mostly with poly(ethylene oxide) (PEO). Solutions between 1wt.% and 7wt.% were experimented with. Five applications for the fibers were suggested, including composite material reinforcement, surface layer for textiles, support for thin polymeric materials, for application of insecticide on plants, as a route for production of non-woven cloth, and as dressing material for a wound. A second paper entitled *Structure and Morphology of Small-Diameter Electrospun Aramid Fibers* was published in 1995 by G. Srinivasan and D.H. Reneker [28]. This paper concerns the structure and morphology of fibers made from poly(p-phenylene terephthalamide) (PPTA). Fiber diameter ranged from 40 nm to a few hundreds of

nanometers. The fibers were characterized using electron diffraction patterns, bright and dark field microscopy, as well as atomic force microscopy.

Since the above publications, electrospinning continued to be investigated by altering the experimental parameters and the setup to achieve a variety of fiber structures and compositions. Numerous papers and over forty patents exist discussing electrospinning, the use of the electrospun nanofibers, and other related technology. The electric field of the electrospinning setup is often established between the capillary and deposition plate, or two conducing plates with the capillary hanging between them. There are many variables involved in the typical setup such as applied voltage, experimental apparatus geometry, solution flow rate and concentration, volume per spun sample, and temperature of the solution. Table 2-1 lists the main parameters and the effects they have on microstructure.

Table 2-1: Variable electrospinning parameters and their effects.

Parameter	**Effect of Raised Parameter**
Plate-to-plate voltage	Bead density per unit area increases with voltage exponentially [29]
Plate-to-plate distance	Decreases bead density, encourages fiber morphological changes [24]
Capillary tip protrusion into field	increased spun area size, fiber morphological changes
Solution flow rate	Surface tension altered, jet becomes discontinuous if high enough [24]
Volume of solution spun per electrode	More solution spun yields thicker electrodes
Concentration of PAN	thicker fibers, less spindling [29]
Concentration of Pd (II) acetate in total DMF	Increased solution conductivity yields higher charge transfer, which lowers bead density [22]
Temperature of Solution	Raised temperature allows for a faster process, but increases defects [24]

Table 2-1 describes parameters for a typical laboratory setup, however, alternative electrospinning apparatus configurations have been proposed and demonstrated. Patents exist on electrospinning with multiple capillary tubes and to achieve larger uniform areas, as seen in Figure 2-3(a). Electrospinning with multiple nozzles and pressurizing the solution were techniques mentioned in Lee's Patent No. 6,616,435 [30]. Spinning in a vacuum was explored by Reneker [31]. Patents on electrospinning apparatus exist by

Chu for multiple jets and Reneker on movable substrates [32, 33]. Coaxial fibers with cores of different materials have been patented by Reneker, as seen in Figure 2-3(b), and also demonstrated by Sun et al. [34]. Sun has observed clay particles in electrospun fibers [35]. McCann et al. followed up prior work and have been able to produce core-sheath, hollow, or porous structures [36]. This technique has significant applications because the center core of the fiber can be spun of a separate material and then removed.

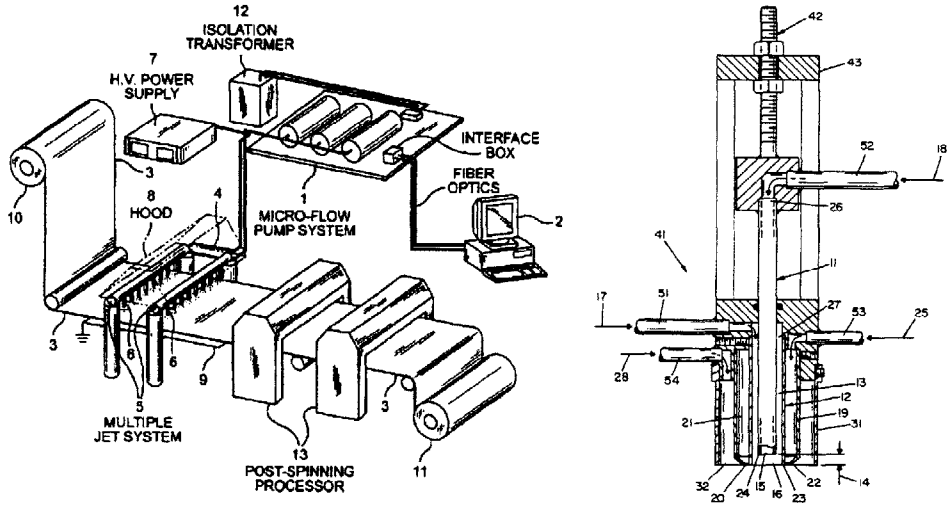

(a) (b)

Figure 2-3(a,b): (a) Electrospinning setup with multiple jets, excerpted from US Patent No. 6,713,011 [32]. (b) A diagram of an electrospinning nozzle able to spin fibers with several layers of cores from US Patent No. 6,520,425 [33].

The shape and structure of the fibers have also been altered by varying electrospinning parameters. Fong et al. demonstrated beaded polymer nanofibers [37]. A relationship is developed between viscoelasticity of the solution, charge density, and surface tension on the effect of bead formation. Ribbon-shaped, branched, and beaded polymer fibers were fabricated by Koombhongse [38].

Another method by which to form nanoparticles is electrospraying. The difference between electrospinning and electrospraying is that electrospraying uses an unstable jet. The jet is non-continuous so that instead of long fibers, the polymer forms droplets. Electrospraying is similar to the well known process of inkjet printing.

2.2.1 Materials

A variety of materials have been used in electrospinning, as demonstrated in Table 2-2. More materials are capable of being electrospun; these are only some reported in the literature.

Table 2-2: List of Materials that can be Electrospun. It is of great importance to the fuel cell industry that the last substance, Nafion, can be electrospun.

Material	**Scientist / Lab**
Polyacrylonitrile (PAN)	Kang [39]
PEO	Doshi and Reneker.[20]
poly(p-phenylene terephthalamide) (PPTA)	Srinivasan and Reneker [28]
nylon, polyimide, DNA, polyaramid, and polyaniline	Reneker [40]
DNA	Fang and Reneker [41]
Silk	Zarkoob and Reneker (US Patent No. 6,110,590) [42]
polyacrylonitrile and mesopashe pitch	Chun and Reneker [43]
Styrene-butadiene-styrene tiblock copolymers	Fong and Reneker [44]
polybenzimidazole for reinforcement fibers	Kim and Reneker [45]
poly(ethylenimine)diazeniumdiolate in medical devices	Smith and Reneker [46]
poly(ferrocenyldimethylsilane)	Chen et al. [47]
Poly(meta-phenylene isophthalamide)	Liu [48]
garlands of polycaprolactone	Reneker [49]
Nafion	Sanders et al. [50]
PLA	Bowling et al. [51]
poly(glycolic acid)	Bowling et al. [51]
poly(ethylene-co-vinyl acetate) (PEVA)	Bowling et al. [51]
Type I collagen	Bowling et al. [51]

Table 2-2 lists some pure chemicals that were electrospun in literature, and their applications can be found in the following section. However, it is possible to electrospin multiple solution components in mixture form. Schreuder-Gibson et al. have electrospun carbon nanotubes in a polymer solution to produce a network of organic polymer fibers encapsulating carbon nanotubes that aided significantly in electrical conductivity. Fabrication of electrospun nanofibers hybridized with metal nanoparticles has been achieved by spinning metal salts and annealing. Electrospinning to form matrices of nanofibers with metal nanoparticles was also being investigated by Demir. A patent by

Reneker details electrospinning metal salt and polymer solutions to secure the metal for catalyst use is detailed as well [52-55].

2.3 Applications

There are a multitude of suggested applications for electrospun materials. Electrospun fibers are excellent candidates for filtration and membrane applications due to their small pore size and large specific surface area. They can be used as textiles, composite reinforcement, and in the biomedical field as well [29].

As separation devices, electrospun nanofibers would make excellent filter media for submicron particles in separation industry. By utilizing the electrospinning apparatus with a core of decomposable material, large nanotubes may be constructed and surface features controlled for better filtration [22].

Electrospun fibers have been suggested as supports for nano-electronic machines. By spinning blends of non-electronically conducing polymer and a conducting material, semiconducing fibers can be made [22]. These have applications in micro- and optoelectronics, for example, nanowires, LEDs, and photocells. Ziegler et al. have prepared a flexible photovoltaic membrane by electrospinning polyacrylonitrile (PAN) nanofiber mixed with copper phthalocyanine dye, while nano-crystalline TiO_2 semiconductor particles can be embedded as well within the nanofibers [56]. Electrospinning solutions of polymers with metal salts has been explored for the purpose of creating active layers for use in sensors [54]. Manipulation of the charging on substrate or collector can yield three dimensional structures.

Electrospun materials are of interest to the military. Some types of electrospun elastomeric polymers are being examined for use in soldier's protective clothing. In the textile industry, nanofibers may be used as protective shields in specialty fabrics [22]. Small pore sizes aid in protection from chemical attacks. Another interesting invention was the use of nanofibers as chemical sensors for explosive detection. Blends of PEO

and fluorescent poly((*p*-phenylene ethynylene)-alt-(thienylene ethynylene)) electrospun with chloroform glow when exposed to explosives [22]. Nanofibers can improve electrochemical cell performance to allow for longer lasting, higher performing zinc-air batteries for portable commercial and military electronics

Alternative biomedical applications include: Scaffolding support for tissue regrowth, tissue engineering, wound dressing, drug delivery, artificial organs, and vascular grafts. Much research has gone on in this area and more can be found in the summary paper by Frenot [22].

2.4 Processing

Carbon fiber processing has been well studied in the past due to the growing number of applications and demand for the high-strength and low-weight material. Applications of traditional carbon fibers (on the order of microns in diameter) are in aerospace and automotive areas, where the fibers serve to reinforce materials and are particularly attractive because of their ability to resist high temperatures. Traditional carbon fibers have been used to reinforce materials such as concrete, metals, and polymers. General-purpose carbon fibers are also used for thermal insulation, sealing materials, electrically conducting materials, antistatic materials, heating elements, electrodes, filters, friction materials, sorbents, and catalysts [57]. Carbon is a catalyst itself in many chemical processes.

To fabricate carbon fibers, polymer fibers typically made from polyacrylonitrile (PAN) or pitch are annealed. Annealing of the less expensive PAN involves two steps: Stabilization and carbonization. The stabilization process is often completed in an air environment between 180-300 ^{o}C. Stabilization is required to make the PAN flameproof and stable at higher temperatures (>700^{o}C). Carbonization typically is performed in an inert environment at temperatures between 600-1500 ^{o}C. Occasionally, graphitized fibers are desired, and graphitization is performed in inert atmospheres at temperatures between

1500-3000°C. Annealing transforms the fibers to be electrically conductive and stronger, but less ductile. The change in chemical composition is detailed below in Figure 2-4.

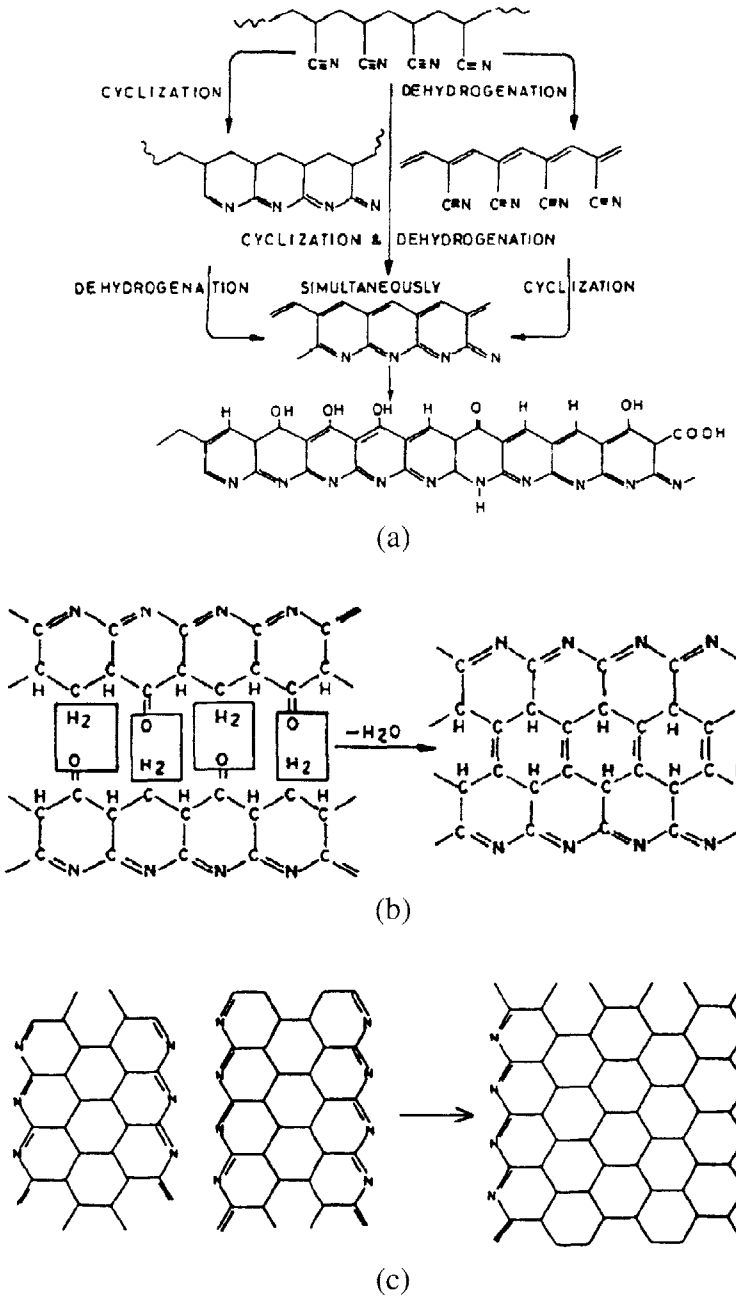

Figure 2-4 (a-c): Diagram of the molecular changes occurring during the chemical process of stabilization and carbonization of PAN. (a) The stabilization step, which occurs between 180-300°C in air environment. (b-c) The carbonization step. Shown in (b) is the mechanism of intermolecular cross-linking between 600-1500°C through oxygen-containing groups, however, dehydrogenation is a possible mechanism as well. In (c), cylclized sequences are cross linked and nitrogen atoms are released. Figure courtesy of Carbon Fiber Composites [57].

Other dated papers on pyrolysis of PAN add further to the discussion and understanding of the carbonization process [58, 59]. More recent research efforts have been focusing on annealing PAN nanofibers. The most recent and relevant paper is by Wang et al. and concluded that the conductivity of PAN nanofibers increases sharply with temperature and considerably with pyrolysis time at lower temperatures of 600, 700, and 800°C, but less obviously with higher temperatures (above 1000 °C) [60]. Typical values of electrical conductivity were reported as 10^4 S/m for a single, isolated fiber treated at 900°C under vacuum. The nanofibers examined were made from electrospinning PAN in a DMF solution. Thermal gravimetric analysis (TGA) and thermal differential analysis (DTA) demonstrated how the evaporation of DMF below 200° contributed to weight loss of 91.66wt.% during heat treatments, leaving 8.34wt.% PAN. Wang et al. claim this concurs with theory because their initial concentration of PAN in the solution was a similar value. Of the remaining 8.34wt.% of PAN, 46.5wt.% remains after being heat treated to 600 °C, and 40wt.% is left after 1273 K (1000 °C).

In the scenario where noble metal salts are mixed in solution with PAN and electrospun to form electrodes, the annealing process has multiple functions. The insulating PAN fibers are strengthened and converted to electrically conducting or semi-conducting carbon or graphite nanofibers. Moreover, heat treatments have the effect of precipitating and coarsening metal nanoparticles.

Gallagher and Gross published on the thermal decomposition of palladium (II) acetate in air, nitrogen, and vacuum environments [61]. At atmospheric pressure, palladium (II) acetate decomposed between 200 and 300 °C, dependent upon heat treatment rate. At rates of 2°C/min, weight losses were 53.52wt.% prior to oxidation (250-300°C). Note that palladium (II) acetate is 47.4wt.% metal. Gallagher and Gross also report that in the presence of oxygen, the palladium slowly becomes Pd-O up to the decomposition temperature near 800 °C, after which mainly pure palladium exists. There has even been recorded a slight loss of Pd species, presumably due to sublimation or gas entrainment below 300 °C.

2.5 *Research Objective*

The aim of this research is to improve current oxygen reduction electrode technology. The process of electrospinning was suggested as the method to fabricate electrodes with lower polarizations that are more cost effective. Fuel cells require superior electrodes that more efficiently utilize catalysts and are less expensive to produce. Catalyst homogeneity and geometrical efficiency can be realized through adjusting the electrospinning experimental parameters in fabrication. The procedure is a continuous manufacturing process that can be automated for savings. If successful, this research will lead to revolutionary designs and improvements of air electrodes and enable the development of a practical, rechargeable zinc-air battery and fuel cells with high power densities than are currently available.

2.6 *Approach of This Study – Fabrication and Characterization*

Electrospinning is a well known procedure, however, the experimental parameters for electrospinning a solution of polymer with noble metal salt for use in an optimized electrochemical apparatus are not known. Experimentation will find working values for variables such as solution composition, plate-to-plate distance, solution flow rate, applied voltage, and volume of solution spun. After electrospinning, the polymer nanofibers will be heat treated at various times and temperatures to increase the fiber's electrical conductivity and precipitate noble metal nanoparticles. Once fabrication of the electrode has been completed, characterization will commence. The microstructure of the electrode can be characterized through X-ray diffraction (XRD) and microscopy using a Scanning Electron Microscope (SEM) and Transmission Electron Microscope (TEM). Physical properties, such as conductivity of the electrode, can be tested using a microprobe station. Electrochemical properties can be examined using Rotating Disk Electrode (RDE) techniques, as well as installing electrodes in a working fuel cell. An iterative engineering process will continue exploring the effect of changing the experimental variables with the intent of maximizing electrochemical performance on an economic basis.

3 EXPERIMENTAL

In this chapter, the experimental procedure for fabricating and characterizing electrospun carbon nanofibers decorated with palladium nanoparticles is discussed. The electrospinning procedure contained numerous variable parameters. The refined procedure for preparation of the solution of n,n-dimethylformamide (organic solvent DMF), polyacrylonitrile (polymer PAN), and palladium (II) acetate (noble metal salt PdAce) is detailed below, along with the electrospinning setup and working parameter ranges. For ease of production and desired geometry, polyacrylonitrile (PAN) was chosen as the polymer for electrospinning.

Several methods of characterization were performed to attain a better understanding of the features of the fibers, the noble metal particle size as a function of time and temperature, and the performance of the catalyst. These included: Scanning Electron Microscopy (SEM), Transmission Electron Microscopy (TEM), X-Ray Diffraction (XRD), Cyclic Voltammetry (CV), Rotating Disk Electrode (RDE), microprobe station, weight measurements, and Brunauer-Emmet-Teller (BET) Surface Area Measurements. Details of the experimental setups and methods are described in the following sections.

3.1 Theoretical Loading Calculations

Before the solution was prepared, the theoretical loading of the resulting electrospun fibers was estimated. This calculation was detailed in Appendix A. The results of calculations such as these served as an approximation of solution concentration, but values were usually altered for experimental purposes.

Additional parameters required to define the properties of spun electrodes included the Pd/C ratio and the noble metal loading per unit area of electrode. As discussed in Section 1.3.2.2, the catalyst efficiency can be expressed using the catalyst / support mass ratio. This quantity can be found using the following calculation.

The solution contents must be known to determine the Pd/C ratio. An example of typical solution contents are shown below in Table 3-1.

Table 3-1: Typical solution contents necessary for calculating the Pd/C ratio.

Chemical	Mass (g)
DMF	7.00308
PAN	0.69237
Pd (II) acetate	0.19977

To calculate the Pd/C ratio, the total amount of palladium must be known. The tabulated chemical properties of the solution components are detailed below in Table 3-3.

Table 3-2: Material properties of the chemical compounds used in creating the electrospinning solution.

Compound	Formula	Molec. Wt. (g/mol)	Density at 25°C (g/ml)
Polyacrylonitrile	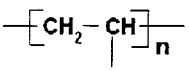	$M_{PAN} = 53.06$	ρ_{PAN} =1.184
n,n-dimethylformamide	$HCON(CH_3)_2$	M_{DMF}=73.09	ρ_{DMF} = 0.9481
palladium (II) acetate	$[Pd(C_2H_3O_2)_2]_3$	M_{PdAce} = 673.46	unknown
pure palladium	Pd	M_{Pd}=106.42	ρ_{Pd} = 12.0

The total amount of palladium, m_{Pd}, in the solution is found by multiplying the mass of palladium (II) acetate, m_{PdAce}, by the molar fraction of pure palladium in palladium (II) acetate:

$$m_{Pd} = m_{PdAce}\frac{3M_{Pd}}{M_{PdAce}} = 0.19977\text{g}\left(\frac{3\times 106.42}{673.46}\right) = 0.0947\text{g Pd} \tag{3.1}$$

The total amount of carbon can be found by adding the amounts of carbon from each chemical:

$$\begin{aligned} m_C &= m_{PAN}\frac{3M_C}{M_{PAN}} + m_{PdAce}\frac{12M_C}{M_{PdAce}} \\ &= (.69237g)\left(\frac{3\times 12.011}{53.06}\right) + (0.19977g)\left(\frac{12\times 12.011}{673.46}\right) = .5129\text{g C} \end{aligned} \tag{3.2}$$

Finally, assuming that the DMF fully evaporates, the ratio is constant throughout the solution, and that none of the Pd or C is decomposed during heat treatment, the weight ratio of Pd/C is:

$$m_{Pd}/m_C = \frac{0.0947g}{0.5129g} = 0.1846 \tag{3.3}$$

The loading per unit area of the final, heat treated electrode was calculated as well. The amount of solution spun, V_{spun}, and the electrospun diameter, d, were recorded from experimental findings.

$$m_{Pd.elec}/A_{elec} = m_{pd}\frac{V_{spun}}{V_{soln}} \cdot \frac{1}{\pi\frac{d^2}{4} \cdot F_{muffle}F_{tube}} \tag{3.4}$$

where $m_{Pd.elec}$ is the amount of pure palladium on the electrode, V_{spun} is the volume of solution spun, V_{soln} is the total volume of solution, d is the diameter of the spun electrode, F_{muffle} is the size loss factor in the muffle oven (typically 0.64), and F_{tube} is the size loss factor in the tube furnace(typically 0.64 as well). Plugging in,

$$= (0.0947g)\left(\frac{0.1mL}{7.384mL}\right)\left(\frac{1}{3.14\times\frac{5^2}{4}cm^2\times 0.64\times 0.64}\right) = 0.159mg/cm^2 \tag{3.5}$$

It should be noted the values for the Pd/C ratio and noble metal loading are approximate, and contain negligible experimental error.

3.2 Sample Naming Convention

A sample naming convention was necessary to distinguish samples and highlight the differences between electrodes. The method chosen uses the following parameters: Percent weight PAN, palladium to carbon ratio of the prepared solution, heat treatment high temperature, heat treatment time at high temperature, palladium loading of the final electrode with heat treatment losses taken into account, and sample number. These parameters were chose because they tell much about how the sample was fabricated and how it should perform electrochemically.

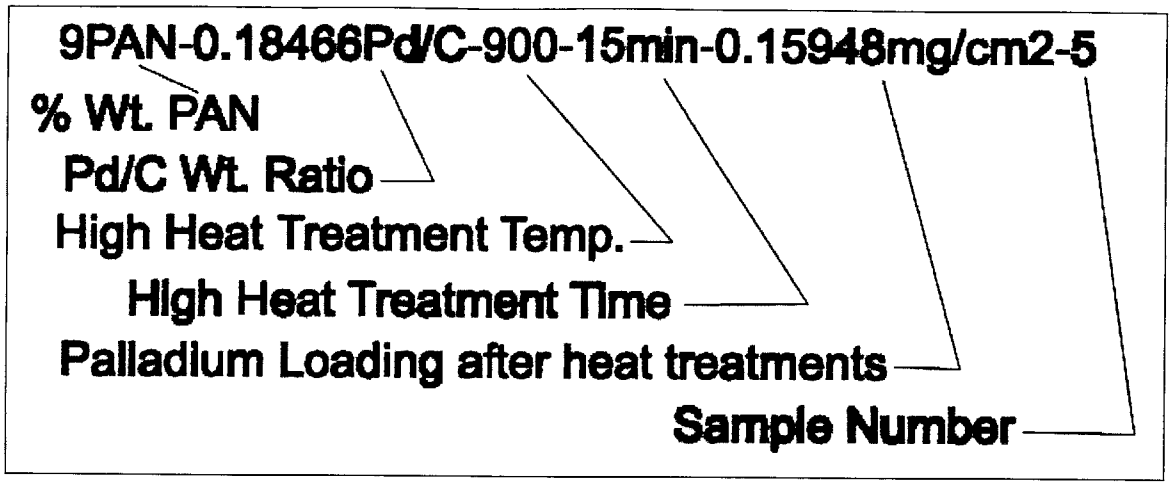

Figure 3-1: Sample naming convention detailed.

The first value, percent weight PAN was usually 7, 8, 9, or 10. If the sample was treated in the muffle oven and not the tube furnace, the high heat treatment temperature is given the value of 280 with a high heat treatment time of 120 minutes. Note that the values for Pd/C ratio and noble metal loading were the same as those calculated in Equation 3.3 and 3.5 in the previous section.

3.3 Fabrication: Electrospinning and Heat Treatments

The electrospinning process to create carbon nanofibers with noble metal nanoparticles required a polymer, liquid solvent, and noble metal salt. A solution was made with poly-acrylonitrile (PAN) chosen as the polymer in powder form, n,n-dimethylformamide (DMF) as the liquid solvent, and palladium (II) acetate as the noble metal salt. This combination of materials was studied in various concentrations. Two attempts were made with moderate success to create nanofibers with platinum catalysts. In these instances, the palladium salt was replaced by platinum (IV) chloride and platinum (II) pentadienoate. On all other occasions, PAN, DMF, and palladium (II) acetate were the solution components.

3.3.1 Preparing the Electrospinning Solution – The Dual Vial Method

The electrospun solution was prepared by unusual methods because noble the palladium (II) acetate facilitated reactions within the solution. For example, if a solution of PAN, DMF, and palladium (II) acetate were mixed, the original state of the fluid was a viscous liquid. Over the course of hours, however, the solution gradually turned into a thick, sticky, gelatin-like substance that was unsuitable for electrospinning. This reaction rate was greatly increased if the temperature was raised. Therefore, it was a requirement that the solution was used immediately following preparation. Use of a sonifier to expedite the dissolution process had the risk of causing palladium (II) acetate molecule being shaken apart or heated by molecular friction. An inhomogeneous solution or one too thick to electrospin was the result of overnight sonifying. It should be noted that the use of alternative salts such as platinum chloride and platinum (II) pentadienoate remained viscous for much longer periods of time and did not suffer from the adverse effect of solidifying.

The following method was developed to create a homogeneous solution for use in an electrospinning experiment. It is referred to as the "Dual Vial Method." The procedure of solution preparation is diagramed below in Figure 3-2.

1) Lab personnel donned appropriate safety gear for handling chemicals, as recommended by the MSDS sheets.
2) Cleaned two 25 mL glassware vials, their caps, two magnetic stir bars, and two teflon-coated scoops thoroughly using acetone, ethanol, and DI water. Dried thoroughly in a drying oven at around 70 ^{o}C until no water residue was apparent.
3) On a balance able to measure 0.00001 g, weighed out appropriate amount of palladium (II) acetate into one vial with teflon-coated scoop.
4) Weighted out appropriate amount of PAN into the second vial.
5) Divided the total amount of DMF. Added 80wt.% to the PAN vial and the remaining 20wt.% to the vial with palladium (II) acetate. Added stir bars to the vials and sealed them with electrical tape.
6) Stirred both vials on a magnetic stir plate for at least two hours. Time was dependent on solution concentration. For example, if a 10wt.% PAN solution was being created, around 4 hours would be required of stirring. When finished, the

PAN vial looked milky white, with small agglomerates of PAN still not fully in solution. This needed to be remedied with heat treatment.

7) The PAN vial was placed in a drying oven at 80 °C for 15 minutes, or until the polymer solution became fully clear.
8) Immediately after removal from the oven, the PAN vial was washed under a cold stream of tap water to bring the solution back to room temperature quickly. The vial needed to be sealed tightly. See note on water exposure below.
9) The contents of the PAN vial were poured into the vial with palladium (II) acetate on the stir plate. The solution stirred on the plate for 10-30 minutes, or until when held up to the light it looked homogeneous. Once the PAN and palladium mixed, the solution was reacting with itself and needed to be electrospun before it became too viscous.
10) The solution was loaded into a clean syringe. Teflon tubing with metal capillary tube at the outlet was connected, and the syringe and tubing were loaded into the syringe pump of the electrospinning setup.

- Note on weighing: Platinum chloride was found to react with the stainless steel scoops, and therefore, the use of teflon-coated scoops is recommended.
- Note on water exposure: PAN was very sensitive to water exposure. If the solution became exposed to a water droplet, the solution was destroyed. Daily humidity also affected the experiment.

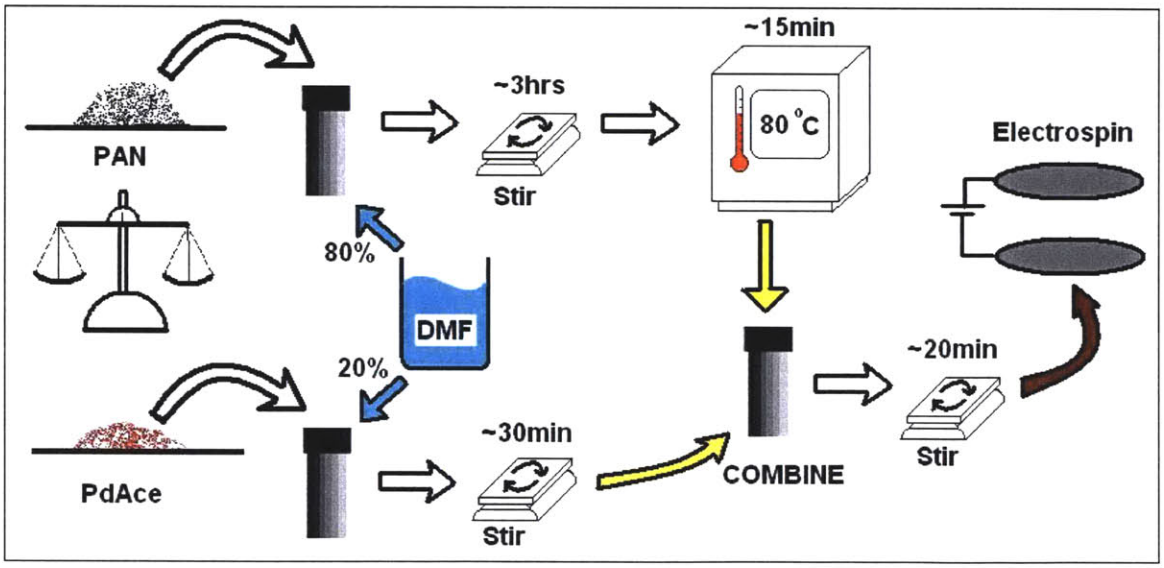

Figure 3-2: Diagram of the solution preparation procedure.

After the solution was prepared, electrospinning was performed immediately.

3.3.2 Electrospinning Parameters and Setup

A photograph of the electrospinning setup in the Electrochemical Energy Lab at MIT was provided with the major operating structures diagramed in Figure 3-3. The prepared solution was loaded into a glass syringe and forced through a capillary tube by a Harvard Apparatus PHD2000 syringe pump. The capillary tube ended with a metal syringe protruding into a high electric field between a charged plate and a grounded plate with aluminum foil substrate. On a few occasions, alternative substrates were used, such as a glass slide, silicon wafer, nickel foam, and E-TEK GDL (carbon paper). The plate distance was variable with a VWR height stand. Voltage was manually adjustable between 0 and 30kV with the Gamma High Voltage Research DC voltage source.

The working parameters of the fabrication process were provided below in Table 3-3. The effect of changing the parameters can be seen in Table 2-1 in Electrospinning.

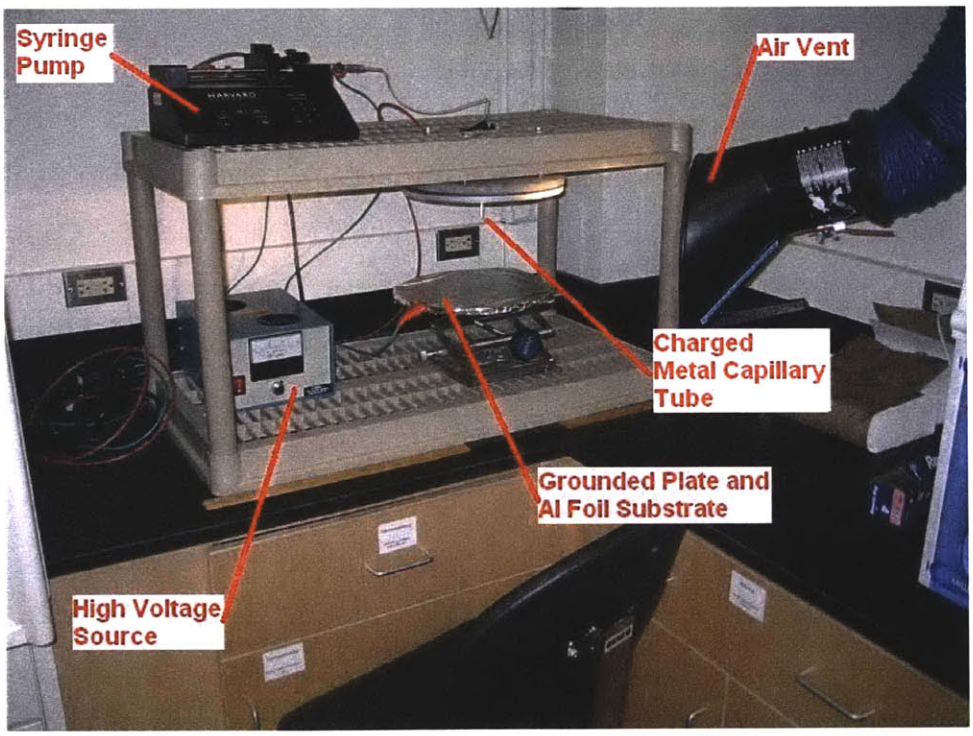

Figure 3-3: Labeled photo of the electrospinning Setup.

Table 3-3: Variable electrospinning parameters and values, where the range at which the setup in the Electrochemical Energy Lab was tested and shown to work is the working range.

Parameter	Working Range
Plate-to-plate voltage	12-18 kV
Plate-to-plate distance	17 cm
Capillary tip protrusion into field	5 - 5.5 cm
Solution flow rate	0.5 - 1.5 mL/hr
Volume of solution spun per electrode	0.01 - 2.00 mL
Concentration of PAN	5 - 10 wt.%
Concentration of Pd acetate in total DMF	0.00411- 0.0413 M
Temperature of Solution	Room (15-23°C)

3.3.3 Heat Treatments

There were two heat treatments performed on electrospun samples to fabricate electrodes. The first stabilization step was performed in a Fisher Scientific Muffle Oven. The muffle oven heated by convection with ambient air in the operating chamber. The heating cycle was as follows, as seen in Figure 3-4a: Ramped up to 50 °C at a rate of 5 °C/min, soaked for 2.0 hours at 50 °C, ramped up to 280 °C at a rate of 1 °C/min, soaked at 280 °C for 2.0 hours, cooled back down to room temperature at the natural cooling rate of the oven (less than 5 °C/min). The initial appearance of the new electrospun fibers was white in color, with a tint of red, depending on the concentration of palladium (II) acetate in the solution. After heat treatment in the muffle oven, the fibers turned a light brown color.

The second heat treatment was performed in a Lindberg/Blue M Mini Tube Furnace. The setup was simply a gas flow line from a tank to the ceramic tube of the tube furnace. A flow regulator and flow meter allowed for adjustable flow rates. Grade 5.0 argon gas was passed through the tube at a rate of 260 mL/min in a 20-30 minute purge cycle prior to heating. After the purge, the flow rate was reduced to 60 mL/min and a heat treatment

was performed. A typical heating profile is shown in Figure 3-4b. The sample was removed after the furnace thermocouple read around 100°C.

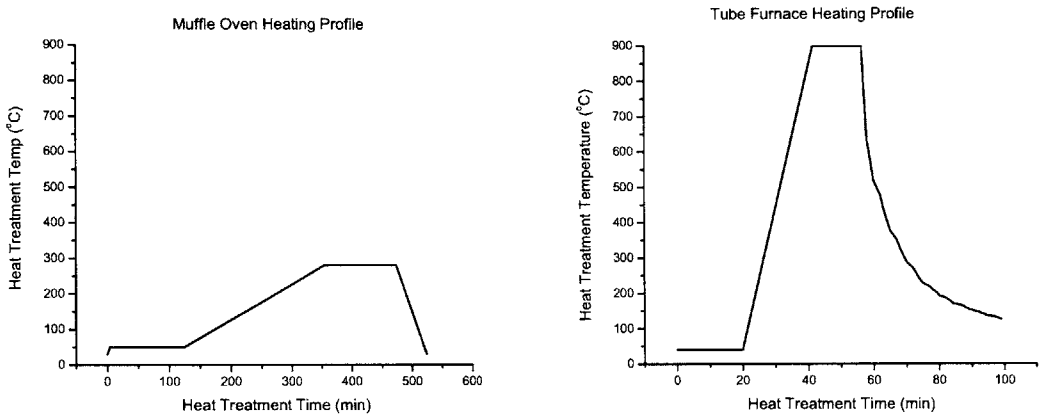

(a) (b)

Figure 3-4(a,b): Plots of typical muffle oven and tube furnace heat treatment profiles. Figure (a) was the profile to which the oven computer is set to run. The actual decay time of cooling was much longer than shown above. Ramp-up rate was 5°C/min. Figure (b) shows actual decay time, but ramp up usually deviated slightly from a straight line depending on the upper limit of the profile. The ramp-up rate was 40°C/min. Note the differences in time scale.

3.4 Characterization

3.4.1 Scanning Electron Microscopy (SEM) Procedure

SEM imaged the overall structure of the electrode; examined for spindling, spraying, or other fiber imperfections; determined fiber thickness; imaged particles of 5 nm or larger; and view cross sections of electrodes to determine thickness. Energy dispersive spectroscopy (EDS) was performed in the SEM with EDAX, Inc. equipment, to determine the chemical composition of the image features.

The electron microscopes utilized to image fiber morphology, electrode microstructure, and the larger palladium particles were located in the MIT Center for Materials Science and Engineering's (CMSE) Electron Microscopy Shared Experimental Facility (SEF).

The FEI/Phillips XL30 FEG SEM/ESEM gun voltage was between 3 and 15 keV, depending on the sample.

A piece of electrode around 0.25 cm^2 in area was laid gently upon a larger piece of conductive carbon tape, which had been previously mounted to a metal sample stage. The stage was mounted in the SEM, and microscopy was performed. For heat treated samples, the normal SEM could be used. For imaging samples that had not been heat treated and were insulating, the microscope was configured for environmental mode, or ESEM with GSE detector.

In cases when the EDS was used, the EDS cooling system was filled with liquid nitrogen at least two hours prior to use. During EDS use, the x-ray beam was focused on a single particle or an area, and a reading was taken. Larger apertures yielded better results.

3.4.2 X-Ray Diffraction (XRD)

XRD was a non-destructive tool to characterize the electrode by determining the material's crystal structure and the various phases. XRD patterns of scattered x-ray photons showed peaks as specific angles for crystalline materials. Peak patterns were specific to individual materials. Peaks could be analyzed to determine average crystal size using the Scherrer equation:

$$t = \frac{0.9\lambda}{B\cos\theta} \tag{3.6}$$

where t was the average crystal size, B was the full width half max (FWHM) of the peak, θ was the diffraction angle, and λ was the wavelength of the x-rays, in all experiments fixed at 1.5406 Å for $CuK_{\alpha 1}$ [62]. Broader background peaks proved the presence of amorphous material.

XRD was performed on a variety of samples with varying heat treatment times, tube furnace temperatures, and electrode catalyst loadings. The XRD instrument was a Rigaku 185mm diffractometer with copper rotating anode and 1.0° divergence slit, 1.0° scatter slit, and 0.3° receiver slit.

To minimize any artifacts in the diffraction pattern caused by tape or other sample holders, the electrode adhered to the glass slide with electrostatic force. The glass slide was cleaned with acetone, methanol, and DI water in the EEL and was transported to the XRD facility in a plastic sample holder. The slide was rubbed thoroughly with a kimwipe to enhance the static charge prior to sample mounting. The sample was then placed in the etched window and pressed down lightly. The slide with sample was carefully taken to the XRD machine and mounted in the holder. Any air currents could disturb the sample. However, it was found that once mounted inside the XRD machine, the sample hardly ever fell off unless larger heavy samples were experimented with. In the case a sample was greater than 1 cm^2 in area and likely to fall off due to limits of the weak static force, a small piece of tape was placed just outside the slide's etched window to hold the sample.

The data were taken in a step scan, with the step duration being 10 seconds, and step increment of 0.1°. A typical full scan ranged from 35° to 80° 2-theta, with some being longer when looking for graphite peaks. A typical scan of the (111) crystal peak was from 39.7° to 40.8° 2-theta, at a step of 0.01°. The step time varied depending on the size of the sample. Larger samples used times of 50 seconds per interval, while small pieces used 500 seconds per interval.

Peak analysis was performed with the help of Jade software. Analysis of the (111) peak scans allowed for curve fitting and background noise subtraction. With a curve fit, the software could calculate the FWHM of the peak, and state the error of the fit. This was then plugged into the Scherrer formula (Equation 3.6) to calculate average crystal size.

3.4.3 Transmission Electron Microscopy (TEM) Procedure

TEM allowed the viewing of nanoparticles and nanofibers with much higher resolution and image quality than the SEM. Electron diffraction patterns were collected to confirm chemical composition of crystalline material. High-resolution TEM was performed on

the JEOL 2010 to get clear images of crystal planes and nanoparticles with diameters less than 10 nm.

The JEOL 200 CX General Purpose TEM and the JOEL 2000FX TEM with LaB_6 filament were used to image fine palladium particles and were located in the MIT CMSE SEF as well.

3.4.3.1 Standard TEM

The JEOL 200 CX and 2000 FX captured images of the palladium nanoparticles with superior resolution to the SEM. The procedure for utilizing the microscope was standard. The sample was loaded on a Ted Pella holey copper film, which has one large gap in the center of the round disk. Approximately a 2 mm by 3 mm section carbon nanofiber electrode was carefully torn from the bulk sample. The torn edge was placed over the hole in the copper film. This allowed single fibers to be imaged without the interference of others that would otherwise be present if the bulk sample were viewed. After images were taken according to standard operation of the microscope, the film was developed and scanned into digital form at 300 dpi or higher, depending on the magnification of the film image.

3.4.3.2 In-Situ TEM

In April 2004, two attempts were made using the JEOL 200CX to investigate the formation of palladium nanoparticles during heating. Both were successful, and with help of a video recorder, particle growth was captured on film.

The loading of the sample was similar to that described above in Section 3.4.3.1. However, the sample being loaded was only heat treated to 280°C in air and the sample was loaded directly without copper holey film. The sample holder was a titanium hot stage, and required additional hardware such as a digital controller with electric power supply, and a gravity-fed cooling system that included a water tank, tubing, and collection bucket. The water was fed slowly through the hot stage and replenished when necessary.

3.4.3.3 Cross-sectional TEM

Several images of cross-sections of carbon nanofibers were imaged using the TEM. Due to the nature of the flat non-woven matte, fibers were never oriented in the vertical direction, orthogonal to the substrate surface. Cross-sectional images were not possible using the conventional methods stated, however, alternative methods were successful. Sample preparation was performed using LADD Research LR White resin of medium grade. A single drop of accelerator was added to about 1 mL of resin. The resin was poured into the mold and allowed to sit for a minute. The sample was then placed in the half-filled mold. A new solution of resin and accelerator was prepared, and expediently poured to fill the mold. This method centered the electrode within the resin block to facilitate cutting. The resin in the mold was allowed at least 24 hours to cure in a fume hood, after which, it was removed from the mold. A razor blade cut away the excess resin and the sample was mounted in the MT-X Ultramicrotome in the MIT CMSE SEF. The microtome was operational at room temperature using a diamond knife. The basin of the knife was filled with deionized water for ease of sample collection. The resin block with carbon nanofibers set in was sliced by the knife until the sample was clearly present. Final slices were taken at 50 and 30 nm thickness. 200 grid copper TEM sample holders were immersed in the water with tweezers to collect the cut sample. The samples were later imaged using the JEOL 200CX and JEOL 2000FX TEM instruments. Care was taken not to focus the beam excessively, which induced thermal stresses that caused the sample to curl inside the TEM.

3.4.4 Microprobe Station

Microprobes were inserted into the electrode to measure the electrical resistance of the bulk material. The effects of heat treatment time and temperature on fiber conductivity were examined.

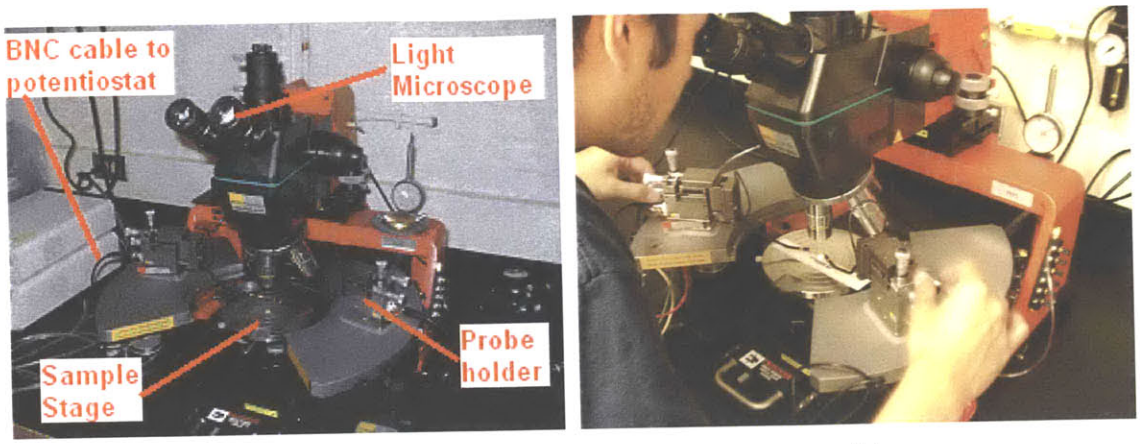

(a) (b)

Figure 3-5 (a, b): Labeled photo of the microprobe station setup and separate image of microprobe station in use.

As shown in Figure 3-5, the Suss MicroTec PM5 Microprobe Station was used to measure the bulk conductivity of the sample. A ruler was placed atop the vacuum stage to calibrate the instrument and align the probes. After focusing on the ruler surface, the probe tips were brought into focus and aligned on the ruler marks, 1 mm apart. This resulted in the probes being in the same plane and exactly 1 mm apart. A vacuum between the probe holders and the gray platforms was established to prevent probe movement. An image of the probes was shown below in Figure 3-6.

Figure 3-6: Light microscope magnified image of probe tip alignment calibration against the lines of a ruler with 1 mm denominations.

After probe tip alignment, the stage was lowered for sample loading. The sample was placed on a glass slide, which was then placed on the sample stage. The sample stage created suction between the slide and the stage, allowing little to no movement of the

slide. The probe tips were kept at the same position; while the stage was moved. With the sample loaded, the stage was raised slowly with the Z-knob on the left side of the probe station while looking in the microscope. When the fibers of the electrode came into focus, the electrode and probe tips were in the same focal plane and in contact. The fibers became slightly out of focus as the tips pushed them down. The Z-knob was turned until the probes were embedded firmly in the fiberous electrode. Then a measurement was taken.

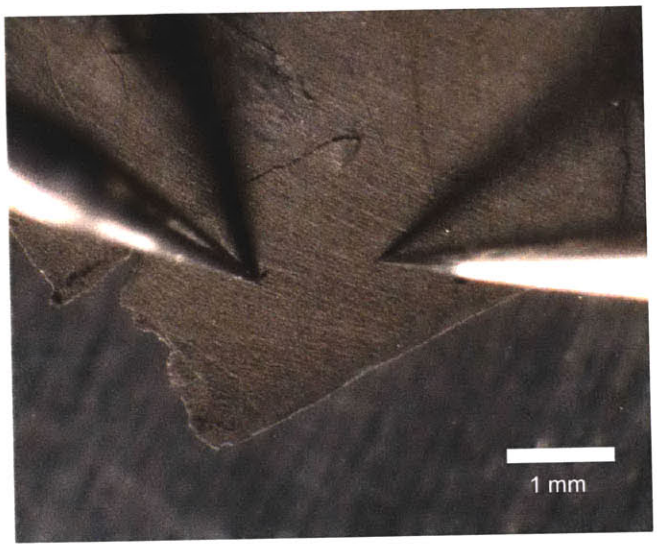

Figure 3-7: Light microscope magnified image of probe tips in contact with electrode.

The measurements were current vs. voltage (i-V) curves. The experiment was potentiodynamic, ramping the voltage from 0 V to 1 V to -1 V, and back to 0 V. The plot was linear, with the slope representing the resistance. Data were taken, usually when the voltage is 1 V, and the slope was calculated.

3.4.5 Cyclic Voltammetry (CV) and Rotating Disk Electrode (RDE)

Pine Instruments setup and rotators were used to measure the electrochemical performance of a catalyst in an electrode. CV was done in nitrogen-saturated solution with a stationary electrode. RDE tested electrodes that were spun at high speeds in an oxygen-saturated, acidic solution to reduce mass transfer effects that would be seen in a stationary electrode.

3.4.5.1 Electrochemical Testing Setup

The RDE setup was used for analysis of catalytic activity of the carbon nanofiber electrodes, and is diagrammed in Figure 3-8. All hardware was purchased from Pine Instrument Company of Grove City, PA, with the exception of the Dell Desktop computer. The cell consisted of three electrodes immersed in an acidic solution: the working (rotating), counter, and reference electrodes. The acid was held in a 125 mL European round-bottom flask with 5 ports: a center 24/40 neck for the rotating shaft, two Ace #7 ports for gas inlet and outlet, and two 14/20 ports for the reference and working electrodes. The rotating shaft extended from an electric motor housing called the rotator. The rotator had an enclosure which could be opened for maintenance and to detach the shaft. At the end of the shaft was the 5mm dia. working electrode made of glassy carbon mounted in a Teflon quickchange tip. The quickchange tip could be pushed into the shaft and sealed by o-rings. It was electrically connected by a spring that touched the back of the glassy carbon. The carbon nanofiber electrode was mounted to the glassy carbon by the method described below in the section entitled "Electrode Preparation." After extended usage, the glassy carbon sometimes became scratched. If not mirror smooth, it was polished with the polishing kit provided. It should be noted that as an alternative to the glassy carbon, a machined and polished palladium rod was inserted into the Teflon quickchange tip to test its electrochemical performance without carbon nanofibers. The reference electrode was a standard calomel electrode (SCE) provided by Pine. The counter electrode was a 22 gauge / 6" Cat. No. 13-766-5A 99.95wt.% pure platinum wire and sealed with a Teflon plug provided by Pine. Connections were made with gold-coated banana plug connectors and alligator clips. The reference electrode was connected to a bipotentiostat with a BNC cable. A Pine AFCBP1 computer-controlled analog bipotentiostat measured the signals from the three sources. The bipotentiostat has two sets of channels, the second being for working, counter, and reference electrodes as well. However, the second set collects data for the ring in the Rotating Ring Disk Electrode (RRDE) configuration, which was not used. The bipotentiostat was connected to the Dell desktop computer via National Instruments PCI NI-DAQ card. The NI-DAQ card converted the analog signal to digital. The card and potentiostat were controlled by

PineChem 2.8.0 software. It was important to note that the system was very sensitive and vulnerable to outside interference. The use of laptops and CRT monitors is not recommended near the setup, unless turned off while a sweep is running. Care should be taken when adjusting the height of the European flask's platform. Vibration could be caused which might shake the carbon nanofiber electrode loose. The setup was adapted to accommodate a Barnstead/Electrothermal 250 mL unimantle for testing performance at varying temperatures. In the elevated temperature setup, the gas outlet tube was replaced with glass thermometer.

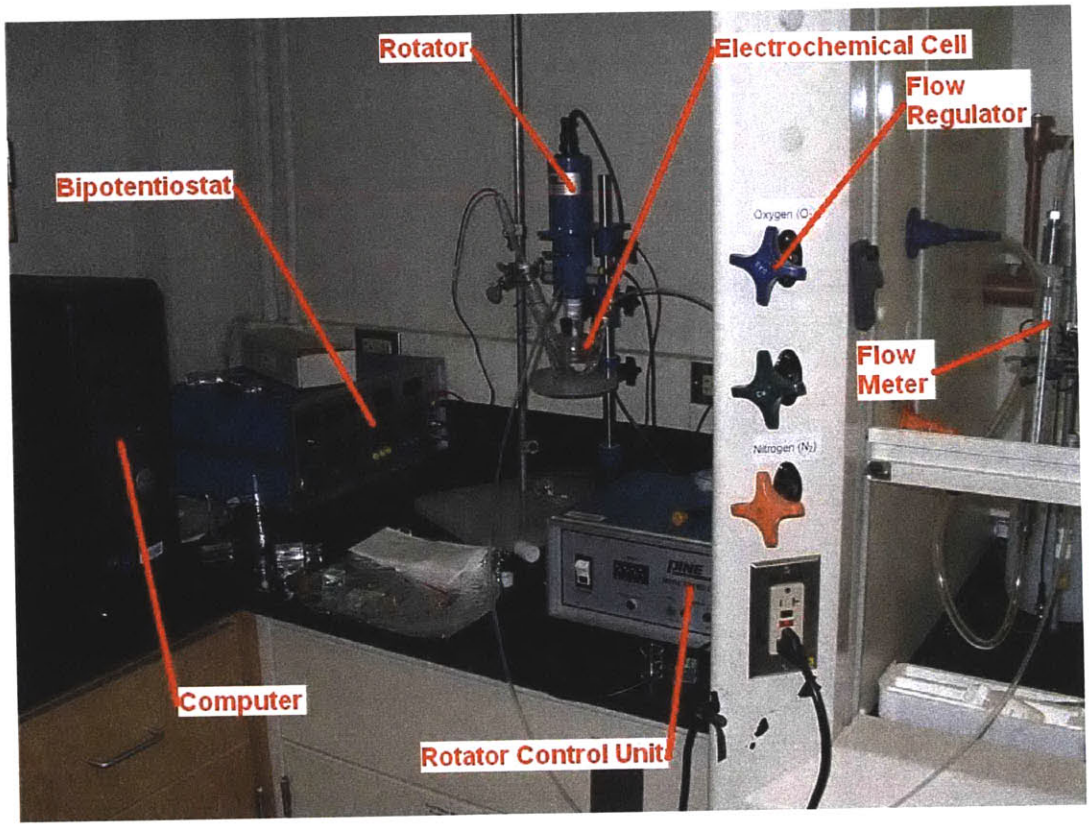

Figure 3-8: Labeled photo of the RDE setup

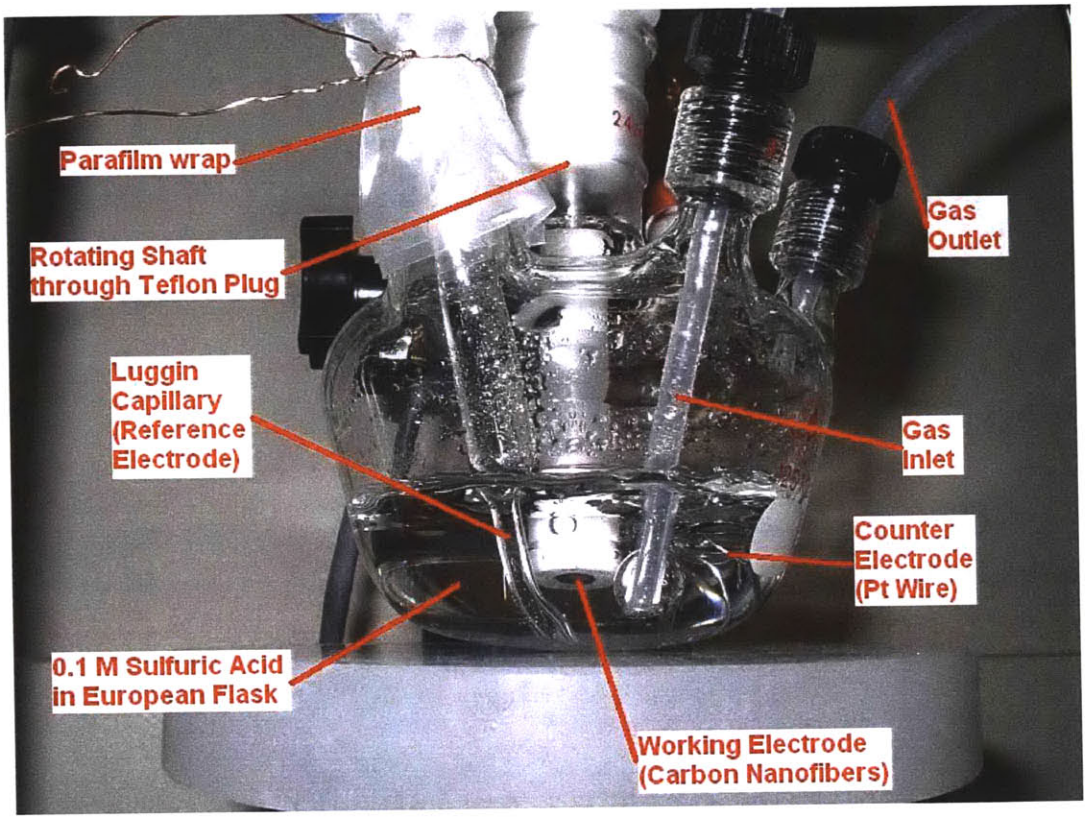

Figure 3-9: Labeled photo of the RDEs electrochemical cell setup.

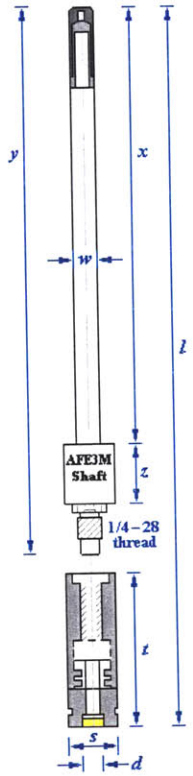

Figure 3-10: Working Electrode Shaft and quickchange tip.

3.4.5.2 Electrode Preparation

The following steps were taken to set up the RDE and perform an experiment. Nitrile gloves, lab coat, and goggles were worn at all times for safety and to reduce the chances of contamination of the cell with oils or salts from the skin. The working electrode was prepared using an electrostatic dissipative (ESD) workstation to minimize the static electricity that caused light samples to fly away or not stick to the glassy carbon disk. The ESD workstation consisted of an All-Spec Industries grounded rubber mat, lab coat, Staticide clean room formula in a spray bottle, and grounded wrist bands. The RDE setup was dismantled during electrode preparation.

First, all glassware and any equipment in contact with the solution were cleaned thoroughly using acetone, ethanol, and deionized water in that order. The lab deionized water was filtered in a Millipore Direct Q system, and had resistance of 18.2 MΩ·cm. A 0.1 M H_2SO_4 solution was prepared in a 250 mL volumetric flask. 50 µL of 5wt.% Nafion 1100 EW solution were diluted in 5 mL of isopropanol. The diluted Nafion solution, carbon nanofiber electrode, tweezers, and RDE shaft with Teflon quickchange disk tip attached were brought to the ESD workstation. The shaft was stood up on the mat, to place the metal in contact with the ground. The shaft, Teflon holder, and 5 mm diameter glassy carbon disk were wiped with a laboratory napkin dampened with Staticide solution. The solution left a visible thin film on the glassy carbon, which was wiped off with a laboratory paper napkin wet with pure isopropanol. With the static dissipated, the carbon nanofiber electrode could be mounted. Using the tweezers, the carbon nanofiber electrode was placed on the glassy carbon disk. In the event that it would not stick to the glassy carbon disk and jump to the Teflon, the Staticide treatment was repeated, followed by another isopropanol napkin wipe. 10 µL of the diluted Nafion solution was dropped onto the electrode on the glassy carbon with a Chemglass 5-50 mL micro pipette. The electrode was left to air dry for 1-5 minutes in an environment with minimal air currents to allow for even drying. For example, drying in a fume hood proved to be non-optimal. When dry, the sample looked lighter and less glossy once dry. This usually took 1-5 minutes.

Once the sample was dry, the shaft and sample were loaded into the RDE rotator motor assembly. With a small flathead screwdriver, the shaft was secured by tightening the screws of the clamp. The rotator enclosure was closed and tightened, allowing the graphite connections to be in contact with the shaft. The European flask was raised until a good seal was made with the 24/40 Teflon stopper with bearings. The platinum wire in 14/20 Teflon plug were lowered into the solution. The gas inlet and outlet tubes were inserted into the flask and sealed with Ace #7 sized plastic connectors with rubber o-rings. The gas inlet line was inserted deeply to bubble through the acid while the outlet was in shallow to prevent acid from clogging the line. The outlet tube led to an oil trap, which prevented back diffusion of air. Through the remaining 14/20 outlet, the acid solution was poured into the cell until it fully covered the working electrode but was not covering the connection between the quickchange tip and shaft. (Soaking this joint in the acid expedited degradation of the o-rings on the quickchange tip.) The Luggin capillary was filled with the same sulfuric acid solution, and inserted into the flask. Before insertion, the Luggin capillary was checked for air bubbles. If a bubble became trapped near the narrow tip, it could be eliminated by holding the tube in one's hand outside the setup, and flicking his wrist gently. Once loaded, the Luggin capillary was held in place by a three-pronged holder attached to a stand. The joint between the Luggin capillary and the flask was wrapped tightly with Parafilm "M" to prevent gas leakage. The Parafilm was tied with copper wire to prevent leaks. Grade 5.0 Nitrogen gas was bubbled through the acid in excess (greater than 100 mL/min) for at least 20 minutes before experimentation. During purging, the calomel electrode was filled with sufficient 4.0 M KCl solution. After the purge time was over, the calomel reference electrode was inserted into the Luggin capillary and all electrodes were connected to the bipotentiostat. After all connections were checked, the bipotentiostat was turned on. It is critical not to turn it on until all connections are made and all electrodes are in the cell. The computer program PineChem 2.8.0 was run on the desktop and controls the bipotentiostat externally.

3.4.5.3 Electrode Testing

Once the cell was turned on and working, cyclic voltammetry (CV) was performed. Typical starting parameters were: 100 mV/s scan rate, 1 amp maximum current, scanned from -250 mV to 1000 mV and back three times (6 sweeps total), with data taken at 1 mV intervals, and the shaft held at 0 RPM. The CV was then slowed and scanned at 50 mV/sec, 20 mV/sec, and finally 10 mV/sec. On the final sweeps, the curve shape and peaks were empirically analyzed to determine if the electrode was performing properly. If so, then nitrogen gas was switched off, and oxygen purged the cell for 5-15 minutes. Following a purge, RDE was performed with the disk rotation at speed between 0 and 3000 RPM, usually at 250 RPM increments and scan rates of 100 or 20 mV/sec. After experimentation was complete, the cell was shut down and the data taken to be analyzed using the PineChem and Origin 7.0 software. Upon cleanup, care was taken to store the reference electrode tip in a sealed container, with KCl wetting the tip.

3.4.6 Other Methods of Characterization

3.4.6.1 Weight and Size Difference Recording

Electrospun fibers were stabilized and carbonized through an annealing process. Using a Mettler Toledo AG285 balance and a ruler, the mass and area of samples were recorded before and after heat treatments. Information collected on mass loss helped in determining the chemical changes occurring during the heat treatments, but due to the complexity of the various reactions, the extent to which each took place was indeterminate.

As-electrospun carbon nanofibers were first heat treated in a stabilization process at a rate of 5°C/min to 280°C for 2 hours in air. During this heat treatment, the average weight loss for sample 8PAN-0.024885Pd/C-280-120min-0.030412mg/cm2 was 21.8wt.%. Gallagher and Gross reported that the acetate was completely decomposed between 200 and 300°C depending on heating rate. For example, at 8 °C/min, acetate was decomposed

by 250°C and at 4°C/min, acetate was decomposed by 240°C [61]. Simultaneously, residual DMF was evaporating and PAN was being stabilized by incorporating oxygen and rejecting nitrogen. Therefore, it was impossible to conclude with certainty the extent of all reactions when the only available data were total sample weight loss.

After carbonization at 900°C for 15 minutes in the tube furnace, the average weight loss for fifteen samples heat treated was 55.0wt.% lost. Four of these samples were plotted below in Figure 3-11, along with other sample data from the tube furnace. Trends were seen for increasing weight loss as heat treatment time increased. The average weight loss of 55.0wt.% was comparable with the calculated values of 53.5wt.% and 60.0wt.% loss reported by Wang for 600°C and 1000°C treatments, respectively with pure PAN fibers [60].

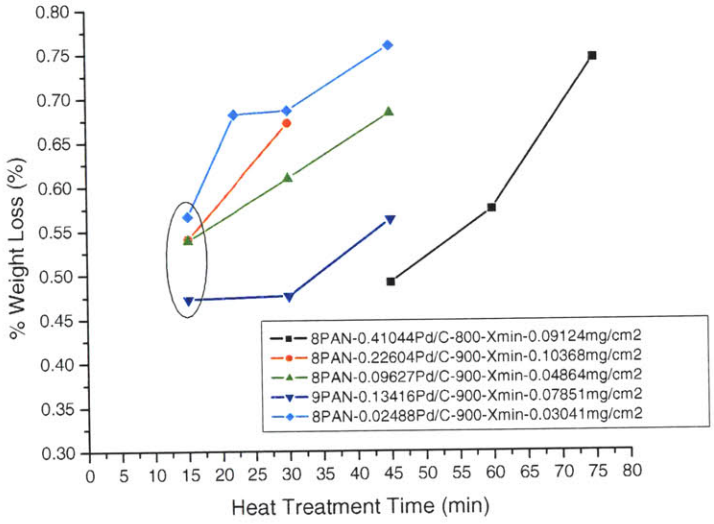

Figure 3-11: Weight percentage loss for various samples as a function of heat treatment time and temperature when baked at 800 or 900°C for varying time in grade 5.0 argon with a flow rate of 60 mL/min.

During the heat treatments at 280°C in air for 2 hours and at 900°C in grade 5.0 argon for any time, a loss in size was typically recorded. Due to mass losses, fibers tended to shrink in diameter on average of 20% reduction when heat treated at 280°C for two hours in air. When heat treated at 900°C in argon for 15 minutes, the diameter of the sample once again changed at around 20% reduction, resulting in an area reduction of 36%.

Calculations showed that sample 8PAN-0.02488Pd/C-900-15min-0.03041mg/cm2-8 lost around 73% of its original area after the stabilization and carbonization heat treatments. The process of weight and size loss is diagrammed below in Figure 3-12.

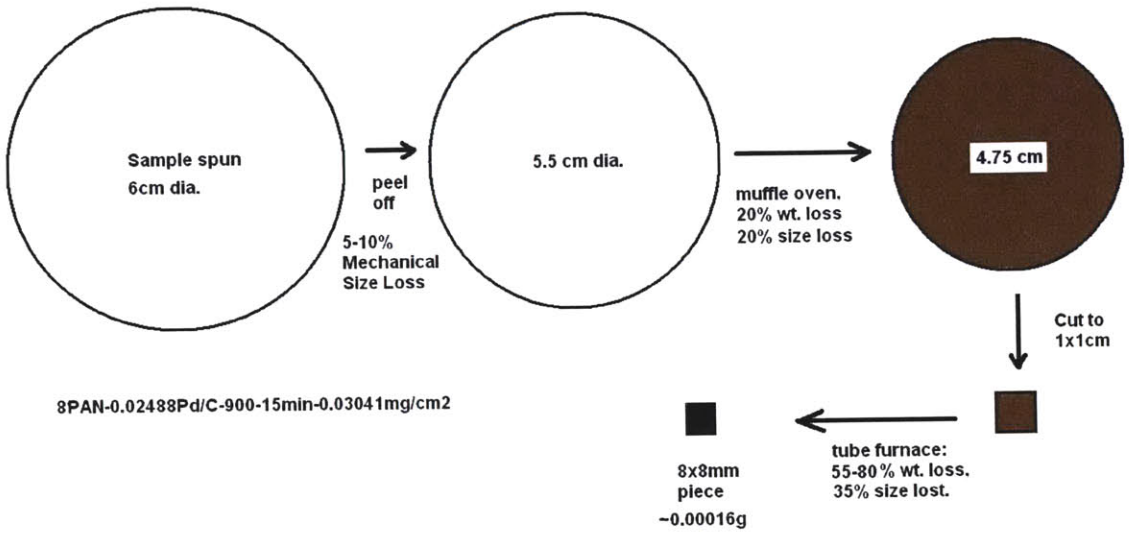

Figure 3-12: Diagram of the heat treatment process for sample 8PAN-0.02488Pd/C-900-15min-0.03041mg/cm2-8 indicating how the sample changed in size and mass during heat treatments. When the new sample was removed from the substrate, some residue often remained resulting in mechanical size loss.

3.4.6.2 Fuel Cell Testing Station

Electrode performance was measured in a PEM fuel cell. The University Model Testing Station was purchased from Fuel Cell Technologies, Inc. Electrospun carbon nanofibers were heat treated and then cut into 1 cm^2 electrodes with a razor blade. A carbon cloth gas diffusion layer (GDL) from E-TEK was purchased and cut into 1 cm^2 sections. An MEA was prepared in the following layered arrangement: Gasket, GDL, nanofiber electrode, Nafion, electrode, GDL, gasket. The anode and cathode were identical. 30 µL of 5wt.% Nafion was added to the GDL to help the electrode stick. No hot pressing was used. The MEA operated in the fuel cell testing station under varying conditions of pressure (0, 10, or 20 psi gauge) and inlet humidity (0 or 100% RH). Voltage and current were measured.

3.4.6.3 XANES

In X-ray absorption spectroscopy the absorption coefficient was defined as

$$\mu = \exp\left[I_o / I_t \right] \tag{3.7}$$

where I_o and I_t were the incident and transmitted intensities, respectively. The coefficient was a function of incident photon energy across the adsorption edge for the ejection of a core level (K or L shell) electron. Typically when plotted as a function of x-ray energy, at the adsorption edge there was a large rise in the coefficient, E_o, beyond which there were oscillations referred to as "fine structure." Those first oscillations up to 50 eV near E_o were referred to as X-ray adsorption near-edge structure (XANES), while the entire region after Eo was called X-ray adsorption fine structure (XAFS) [63]. These oscillations provided structural information and material characteristics about the sample.

Three samples were outsourced to Dr. Mansour Azzam of the Naval Surface Warfare Center. The experimentation was performed and results reported.

4 RESULTS AND DISCUSSION

4.1 Microsctructure

4.1.1 SEM Results

Observable differences could be seen in the fiber morphology before and after heat treatment, as seen in Figure 4-1. First, the image of the as-spun sample in Figure 4-1a appeared blurry and unresolved because it was insulating, causing the sample to charge. It was speculated that the resistivity of the sample decreased during heat treatment, as Section 4.2– Physical Properties confirms later.

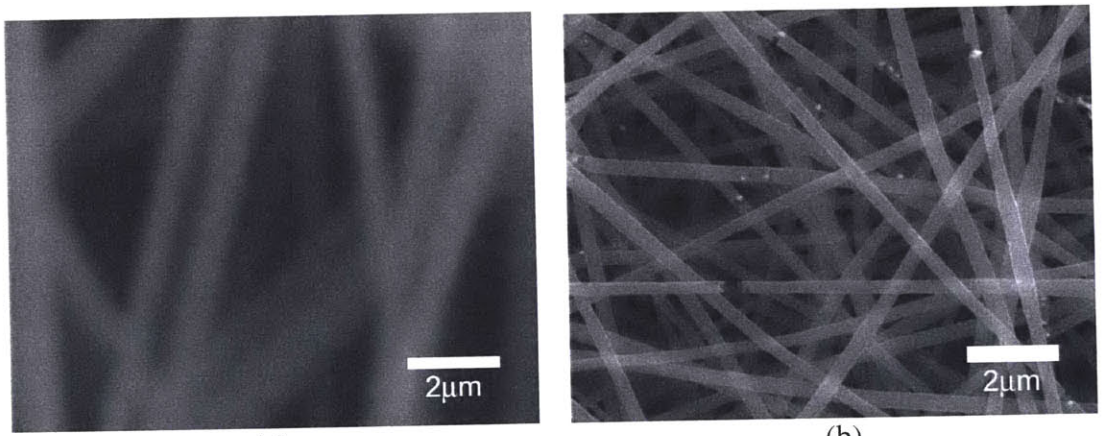

(a) (b)

Figure 4-1(a,b): SEM images of sample 8PAN-0.02488Pd/C-280-120min-0.03041mg/-8 and 8PAN-0.02488Pd/C-900-15min-0.03041mg/cm2-8 comparing fibers that have just been spun to those that have been heat treated in the muffle oven and tube furnace.

Second, the fiber diameter was around 1 μm, as opposed to 300 nm diameter fibers of the heat treated sample, as calculated from further higher magnification imaging. This shrinkage corresponded to weight loss discussed in the Experimental. A third noticeable difference was that bright spots were present in the images of the heat treated samples. The use of energy dispersive spectroscopy (EDS) ensured the bright spots seen by the SEM were in fact palladium particles, as seen in Appendix B.

The SEM images clearly showed that the noble metal loading was uniform and homogeneous throughout the entire electrode area. This was demonstrated below in Figure 4-2.

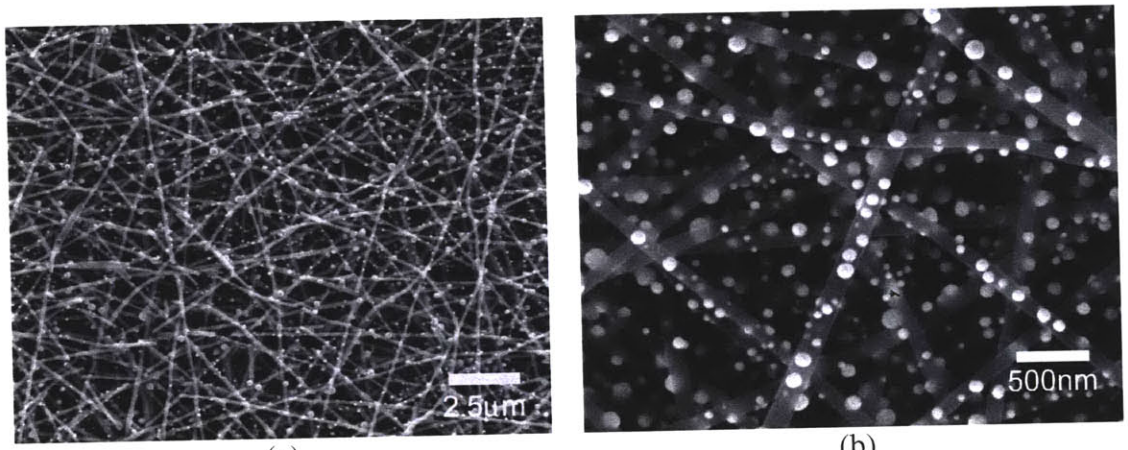

(a) (b)

Figure 4-2(a,b): SEM image of sample 8PAN-0.22604Pd/C-900-15min-0.10368mg/cm2-5 exhibiting homogeneous distribution of palladium particles

Samples could be mounted in the SEM at various angles to obtain views that would enable better understanding of the 3-dimensional structure of the electrode. In Figure 4-3, the electrode 9PAN-0.08815Pd/C-800-75min-0.19353mg/cm2 was mounted at a 90° angle to view cross-sectional images. These images, along with many others like them, showed the thickness of electrodes, demonstrated that particle loading was uniform throughout, and indicated fibers were round in nature.

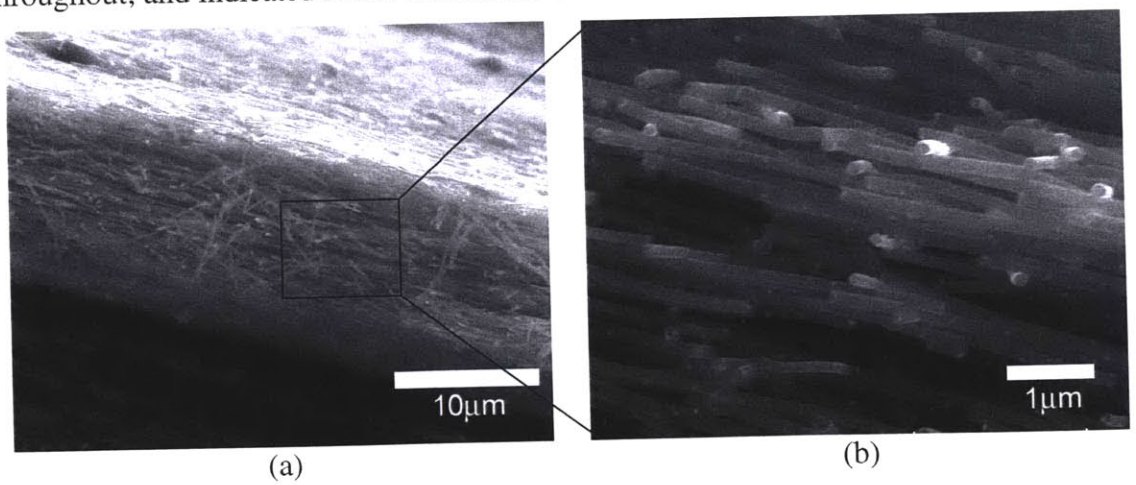

(a) (b)

Figure 4-3(a,b): A cross-sectional SEM image of 9PAN-0.08815Pd/C-800-75min-0.19353mg/cm2 electrode demonstrates how the intact electrode appears when mounted

at 90°. (b) A close-up of the electrode cross-section shows palladium loading is uniform throughout the entire thickness

Combining the thickness measurements from the cross-sectional SEM images with the recorded data of amount of solution spun per electrode, **a relationship between electrode thickness and amount of solution spun was found**, as shown in Figure 4-4.

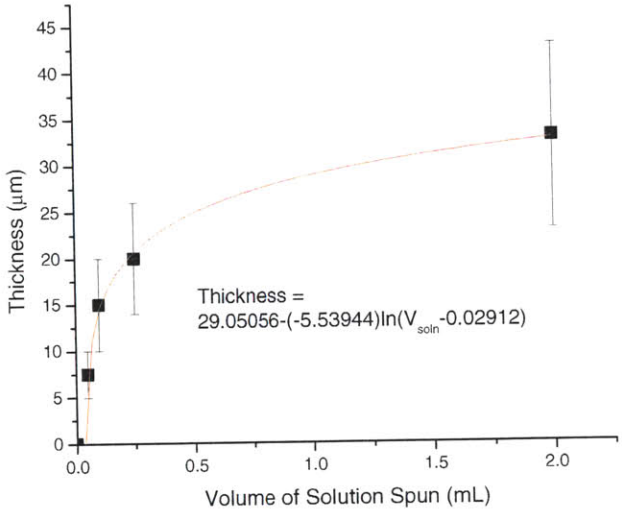

Figure 4-4: Plot of electrode thickness as a function of volume of solution electrospun, exhibiting a logarithmic relationship. The x-axis represents amount of spun solution, which is directly proportional to solution flow rate and time of spinning. Error bars indicate the range of thicknesses seen in the SEM images for unique samples. Additional errors may result when the sample is removed from the substrate after electrospinning and excess material is left behind.

The SEM was a useful tool in detecting defects such as spindling and spraying, as seen in Appendix C. This facilitated the iterative engineering process and exposed problems before any unnecessary further characterization. It was empirically confirmed, as seen in Figure 4-5, that the effect of **increasing PAN concentration led to a decrease in spindling.** These findings concur with what was found in the literature [22].

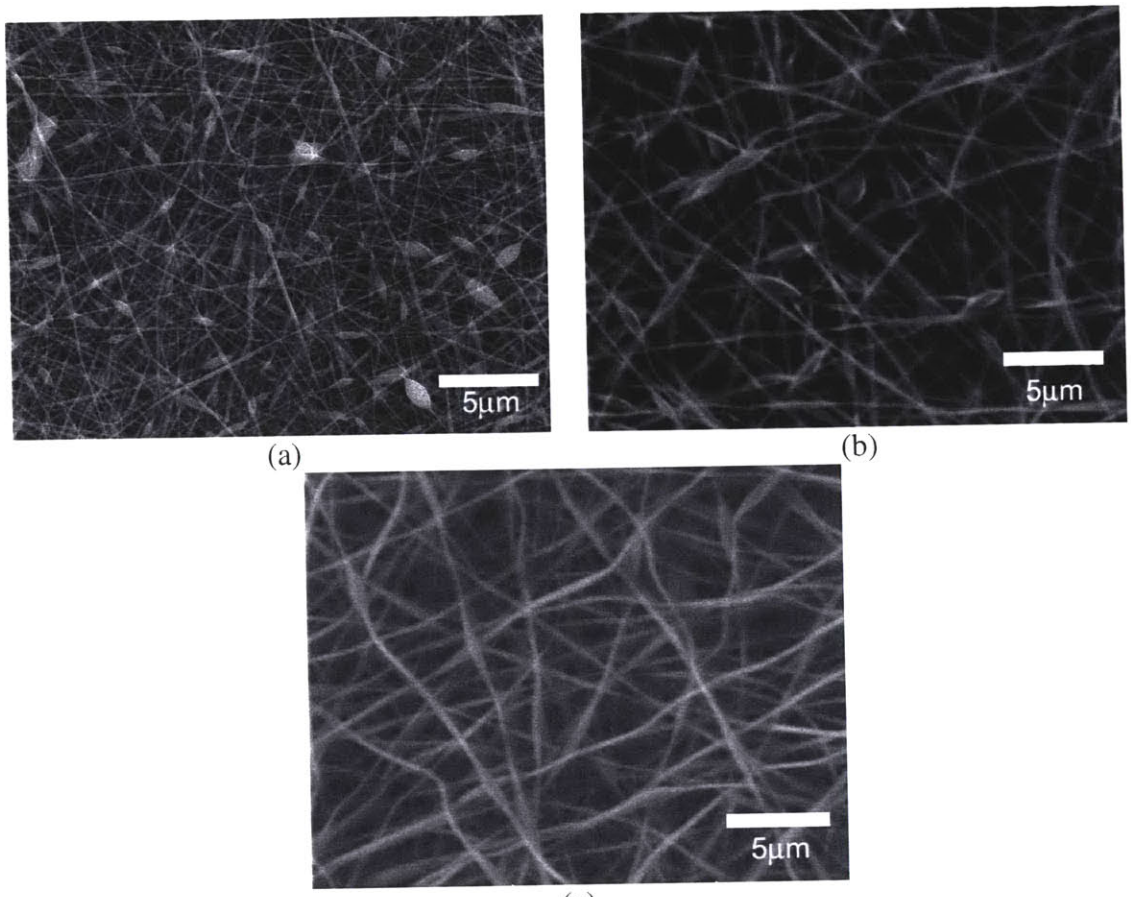

(a) (b)

(c)

Figure 4-5(a-c): SEM images of unloaded samples 8PAN-0Pd/C-900-15min-0mg/cm2, 9PAN-0Pd/C-280-120min-0mg/cm2, and 10PAN-0Pd/C-280-120min-0mg/cm2 in (a), (b), and (c) respectively, that exhibit less spindling with increasing PAN concentration.

After a sample was electrospun and shown to be void of defects in the SEM, further characterization could be performed. Typically, the next step was to characterize the material properties of the microstructure through XRD.

4.1.2 XRD Results

The technique of X-ray diffraction examined the bulk properties of a relatively large area (up to $1cm^2$) of the sample. As shown in Figure 4-6 and Figure 4-7 below, with increased heat treatment time, the palladium peaks formed and became narrower, indicating that palladium crystal sizes were growing. In Figure 4-6, the largest crystal peaks for graphite and palladium oxide were indexed. **There were no resolvable palladium oxide peaks**

found in the nanofiber XRD scans. There was a large amorphous background with a broad peak between 20 and 30° 2-theta, representing the carbon backbone of the electrode. However, **no crystalline graphite could be detected**, even in sample 8PAN-0.02488Pd/C-1100-5min-0.03041mg/cm2-8 as shown in Appendix D.

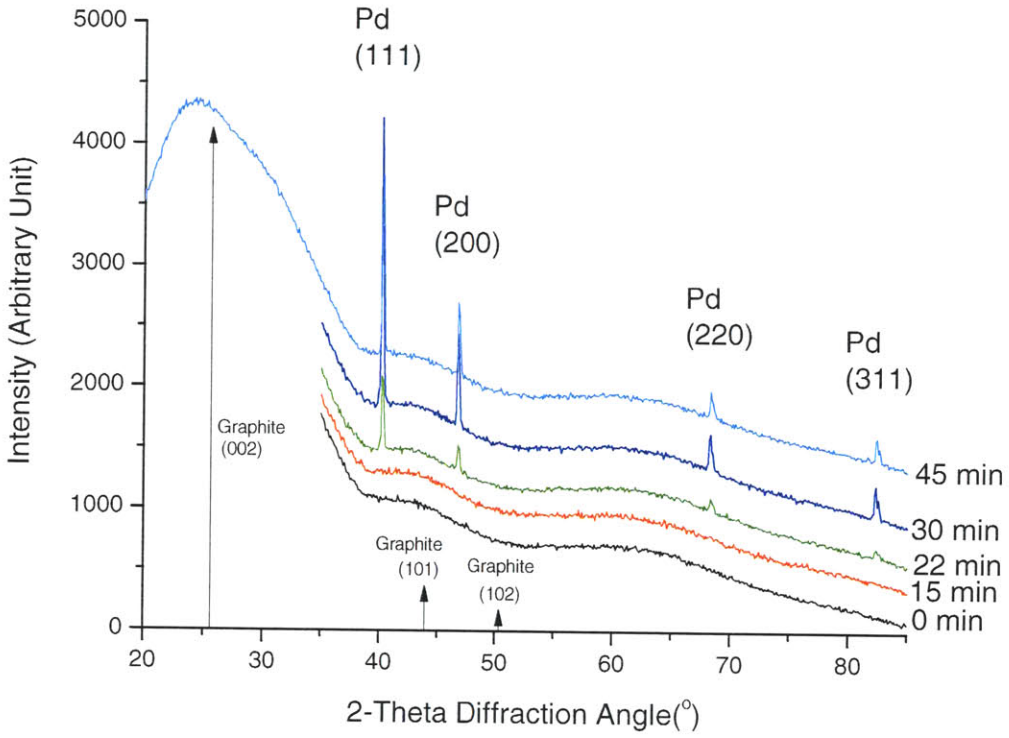

Figure 4-6 Plot of X-ray diffraction intensity vs. 2-theta diffraction angle for five scans of a similar sample 8PAN-0.02488Pd/C-900-Xmin-0.03041mg/cm2-8 heat treated at varying times. As heat treatment time increased, the palladium peaks become more defined. In addition, amorphous backgrounds indicated a lack of graphite. Further examples of XRD scans are in Appendix D.

Analysis of the (111) palladium peaks of several samples revealed an increasing trend in particle size as a function of heat treatment time and temperature. Shown below in Figure 4-8 are the results from (111) peak analysis using the calculated full width half max (FWHM) in the Scherrer equation (3.6). **In general, average crystal size increased with heat treatment time and temperature.** Moreover, it was apparent that for higher temperatures, crystal growth rate increased. In the event that palladium loading and fiber

thickness varied, crystal formation, growth rate, and size varied dependently as shown in Figure 4-8.

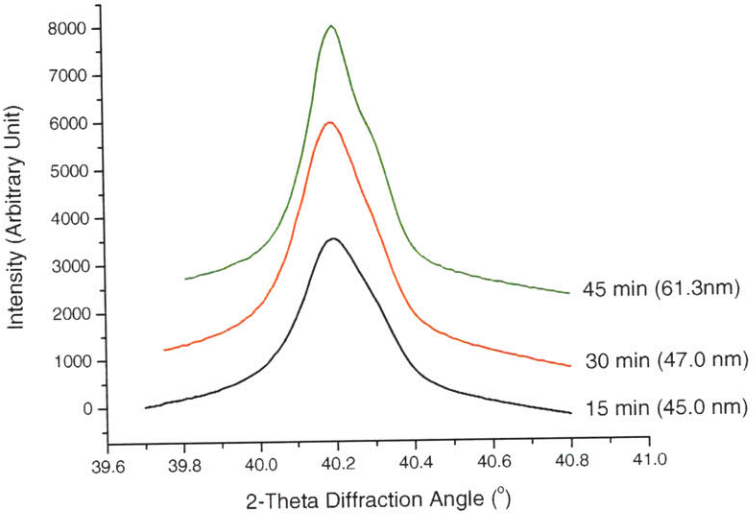

Figure 4-7: Plot of X-ray diffraction peak intensity of the (111) peak from sample 9PAN-0.13416Pd/C-900-Xmin-0.07851mg/cm2 baked at 900°C for 15, 30, and 45 minutes as a function of 2-theta diffraction angle. As heat treatment time increased, narrower peaks indicated larger average crystal sizes. The presence of $CuK_{\alpha 1}$ peaks could be distinguished and subtracted out during peak analysis.

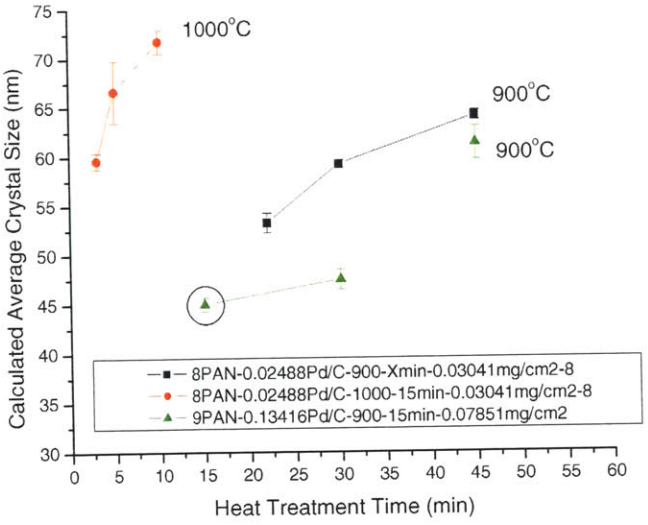

Figure 4-8: Plot of calculated average crystal size of samples heated at 900°C and 1000°C as a function of time. Error reported fluctuated based on goodness of fit of Jade peak-fitting software, which was related to signal noise.

The XRD assigned quantitative values to the average crystal sizes for the bulk electrode. XRD establish a clear, trend between crystal size and heat treatment time and temperature. However, to obtain an in-depth understanding of the micro- and nanostructure of the electrode, further methods of experimentation was necessary. The TEM was able to provide further explanations and insight.

4.1.3 TEM Results

The resolution of the TEM was far superior to the SEM. Using the SEM, particle growth was seen in palladium spheres greater than 10nm in diameter, as shown in Figure 4-2. The TEM images resolved smaller particles on the order of nanometers to give a fuller understanding of the effect of heat treatment time and temperature on a broader range of particle sizes and growth. Seen in Figure 4-9 of sample 9PAN-0.18466Pd/C-900-Xmin-0.12459mg/cm2-9, **the TEM was able to demonstrate that particle size was a function of heat treatment time and temperature.** This confirmed the trend seen by the SEM and XRD.

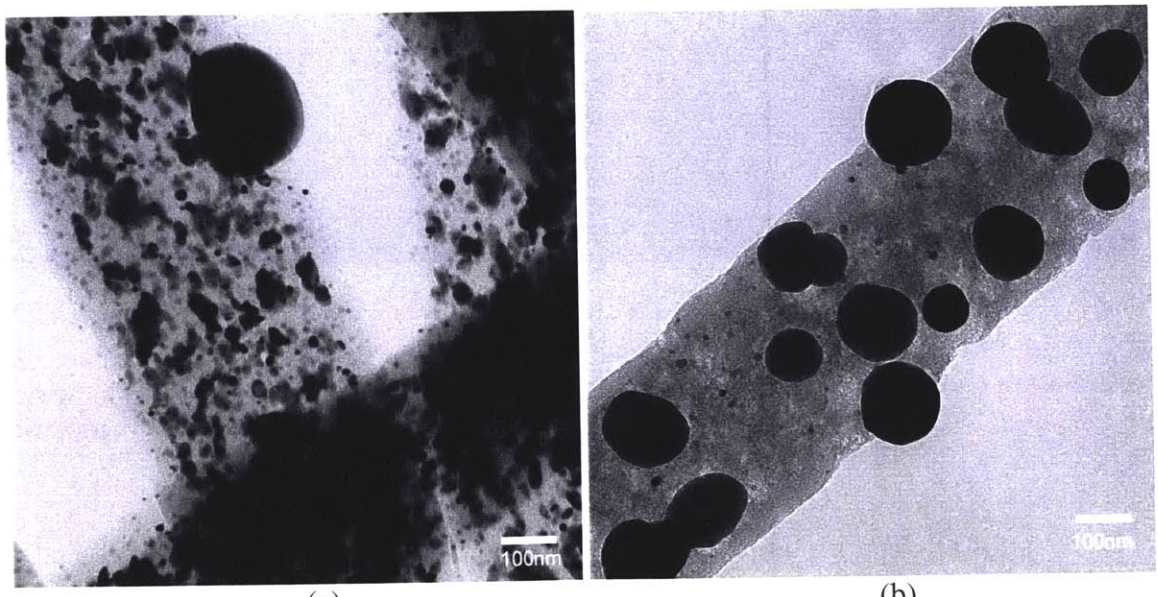

(a) (b)

Figure 4-9 (a,b): TEM images of sample 9PAN-0.18466Pd/C-900-Xmin-0.12459mg/cm2-9 heat treated at 15 minutes in (a) and 45 minutes in (b). The effect of longer heat treatment on particle size is evident.

The relationship between PAN concentration in the solution and average fiber diameter was revealed in the TEM. Comparing sample 9PAN-0.18466Pd/C-900-15min-0.12459mg/cm2-9 in Figure 4-9(a) to sample 8PAN-0.22604Pd/C-900-15min-0.10368mg/cm2-5 in Figure 4-10, the fiber in Figure 4-9(a) has a PAN concentration of 9wt.% and fiber diameter of 472nm, while the fiber in Figure 4-10 has a PAN concentration of 8wt.% and a fiber diameter of 237nm. **Lower solution concentrations of PAN led to thinner fibers.** However, other factors such as salt loading and voltage contribute to the fiber thickness, as reported in Chapter 2, Electrospinnin. Despite similar Pd/C ratios and equivalent heat treatments, there are far fewer smaller particles in Figure 4-10. Due to this evidence, it was hypothesized that particle growth and formation is affected by fiber thickness. **Thinner fibers led to faster particle growth.**

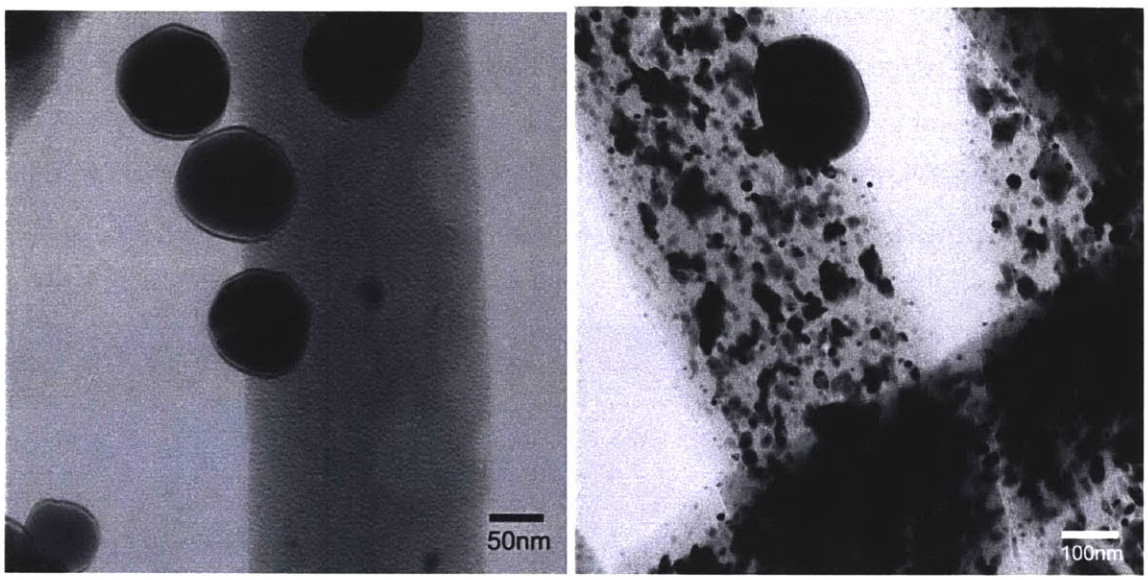

(a) (b)

Figure 4-10(a,b): TEM images demonstrating fiber thickness and particle size distribution as a function of PAN concentration and fiber thickness for sample 8PAN-0.22604Pd/C-900-15min-0.10368mg/cm2-5 in (a) as compared to 9PAN-0.18466Pd/C-900-15min-0.12459mg/cm2-9 in (b), both heat treated at 900°C for 15 min.

The better resolution of the TEM allowed particle size counts to be performed to determine average particle sizes. TEM images of sample 9PAN-0.13416Pd/C-900-15min-0.07851mg/cm2 are shown in Figure 4-11.

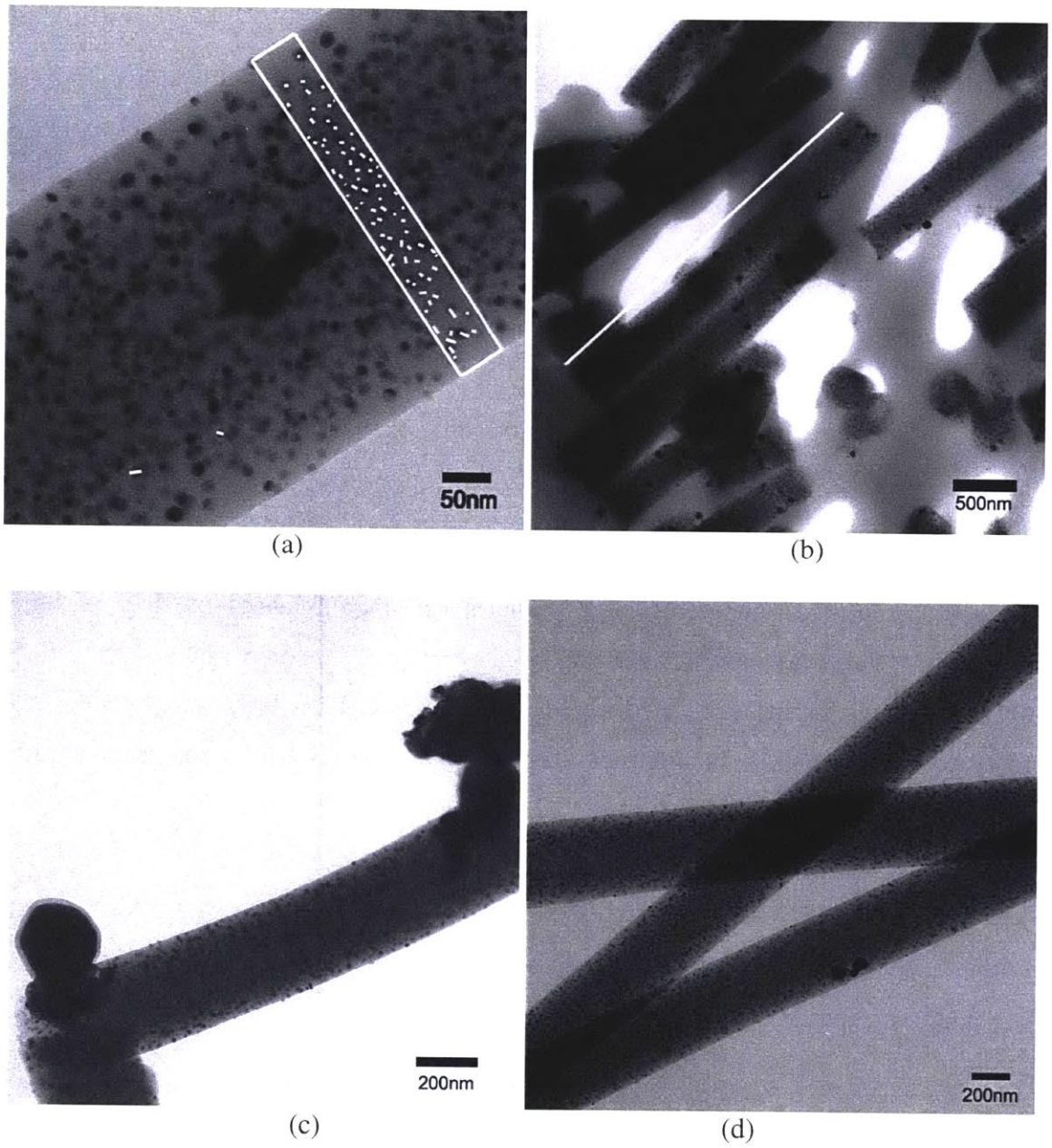

Figure 4-11(a-d): (a) TEM images showing how a 50 nm length of sample's 9PAN-0.13416Pd/C-900-15min-0.07851mg/cm2 fiber has 79 particles along a fiber that is 378 nm in diameter. One 100nm particle exists. (b) Along the indicated fiber that is 3 μm long and has 13 particles that are larger, roughly 100nm in diameter. (c) 200 nm diameter particles spaced roughly 1.5 μm apart. (d) Longer lengths of fibers exhibiting rare occurrences of large particles.

It is evident by cursory inspection of Figure 4-11 that a bi-modal distribution of particles existed, with very few "large" particles (with diameters averaging around 100 nm in diameter) and hundreds of "small" particles (with diameters averaging around 10 nm).

To calculate the average particle size based on TEM images, it was imperative to know the total number of particles in the image. As shown in Figure 4-11a, a 50nm length of fiber was chosen and all small particles within the highlighted area were counted. There were 79 particles found in the 50nm length, and this was normalized to provide a number of small particles per micron length of fiber:

Counts of small particles per length of fiber = 79 small particles / 50 nm length (4.1)

$$\frac{79\,particles}{50nm} = \frac{x\ particles}{1\mu m} \tag{4.2}$$

$$x = 1580 \text{ small particles } /\mu\text{m} \tag{4.3}$$

An estimate of the number of large particles per micron length of fiber was then calculated. This was more challenging because there were some fibers with a higher density of large particles. The three images in Figure 4-11 (b-d) were chosen to be analyzed. For example, in Figure 4-11b, 31 large particles were counted along fiber length of 9.919 μm. In Figure 4-11d, 2 large particles were counted along fiber length of 12.46 μm.

From image (b) and (d) Figure 4-11, the total number of large particles per unit length was approximated as:

$$\frac{31+2}{9.919+12.46} = 1.474\,particles/\mu m \tag{4.4}$$

Based on the calculations result in Equation 4.3 for small particles and Equation 4.4 for large ones, the following histogram can be plotted in Figure 4-12.

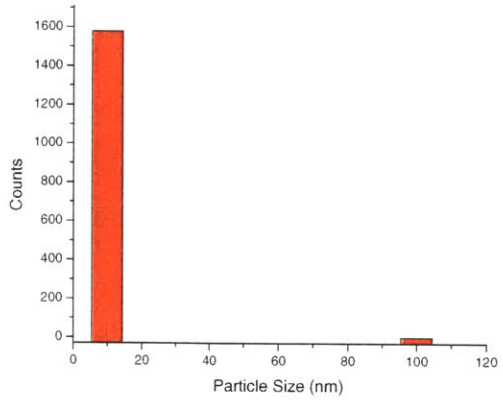

Figure 4-12: Histogram showing simplified bi-modal distribution of particle sizes based on the calculations and analysis performed on sample 9PAN-0.13416Pd/C-900-15min-0.07851mg/cm2. Only two bins existed at 10nm and 100nm for simplification.

The numerical average of the particle size was calculated using the following formula:

$$d_{ave,n} = \frac{\sum_{i=1}^{n} d_i}{n} \tag{4.5}$$

where $d_{ave,n}$ is the average particle size, d_i is the particle diameter counted, and n is the total number of particles. Using Equation 4.5:

$$d_{ave,n} = \frac{\sum_{i=1}^{n} d_i}{n} = \frac{(1580)(10nm)+(1.74)(100nm)}{(1580+1.74)} = 10.08nm \tag{4.6}$$

Another formula representing the volume averaged diameter which the XRD measures, $d_{ave,vol}$, is:

$$d_{ave,vol} = \sum_{i=1}^{n} v_i d_i = \frac{\sum_{i=1}^{n} d_i^4}{\sum_{i=1}^{n} d_i^3} \tag{4.7}$$

where d_i is the particle diameter, v_i is the volume fraction of the palladium crystal.

To find the volume averaged diameter determined by XRD, Equation 4.7 was used:

$$d_{ave,vol} = \frac{\sum_{i=1}^{n} d_i^4}{\sum_{i=1}^{n} d_i^3} = \frac{(10^4)(1580)+(1.474)(100^4)}{(10^3)(1580)+(1.474)(100^3)} = 53.44nm \tag{4.8}$$

For sample 9PAN-0.13416Pd/C-900-15min-0.07851mg/cm2, the calculated numerical average crystal size was 10.08 nm while the volume weighted average was 53.44 nm. The volume weighted average of 53.44 nm was much closer to the 45 nm reported by XRD, denoted in Figure 4-8 by a circled green triangle. Error can be accounted for in a lack of sampling for all areas of the electrode and a limited number of particles counted.

Other distinctions can be made between XRD data and the TEM images. There was a difference between "particle size" from the TEM counts and "crystal size" from the XRD. In the TEM, particles were counted while the XRD data were of average crystal size. Often, a large particle was made up of several smaller crystal grains, as was shown later under High Resolution TEM. This made comparisons misleading.

Additional particle counts were performed on sample 8PAN-0.02488Pd/C-900-Xmin-0.03041mg/cm2-8. Histograms and analysis are reported in Appendix E.

An understanding of the distribution and method of growth of palladium particles began to form. However images alone could not ensure the postulation of a theory with confidence.

4.1.3.1 In-Situ TEM Results

In-situ TEM experiments studied particle formation and growth while it was occurring. There were several findings from the in-situ experiments. First, it was seen in temperature profile Figure 4-13 and Figure 4-14 that **particles became resolved between the temperatures 585 and 684 °C**, corresponding to the times 16:55 and 18:02, respectively. Particles continued to grow as the temperature was increased.

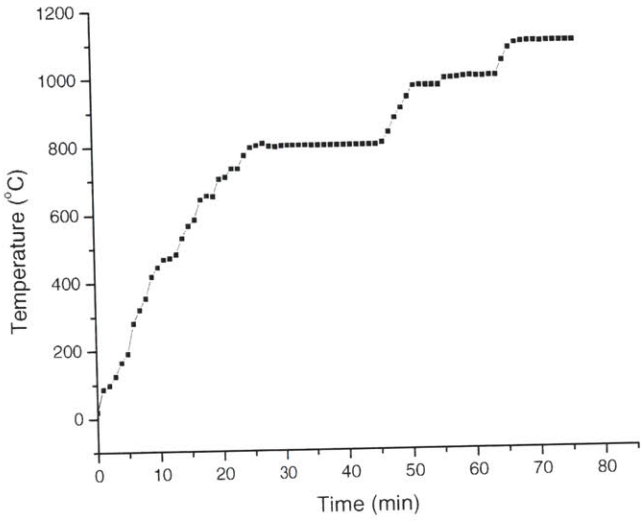

Figure 4-13: Hot stage temperature as a function of time during the in-situ TEM experiment.

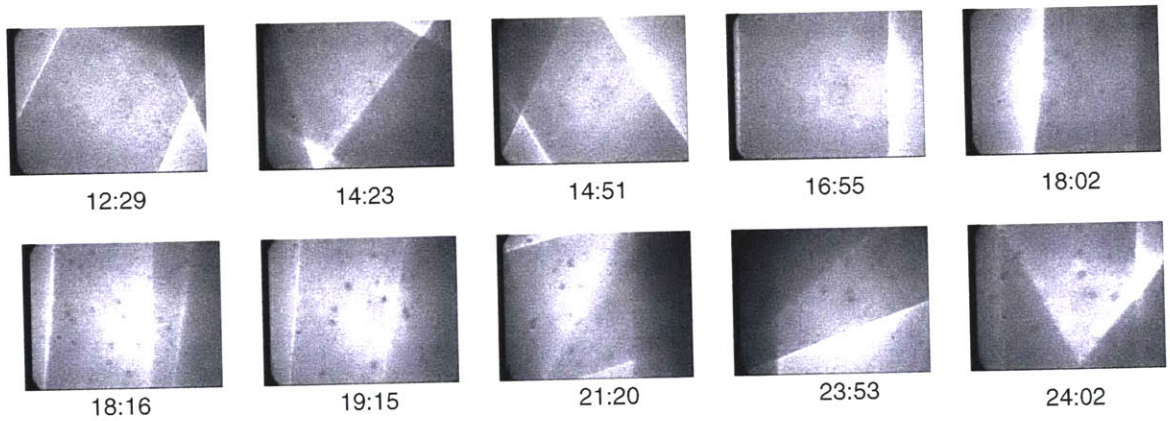

Figure 4-14: Particle precipitation and growth as a function of time for the hot stage TEM experiment for sample 8PAN-0.04926Pd/C-X°-Ymin-0.09124mg/cm2. The magnification was 41kX, with the television adding 15X. Width of an image is approximately 300nm.

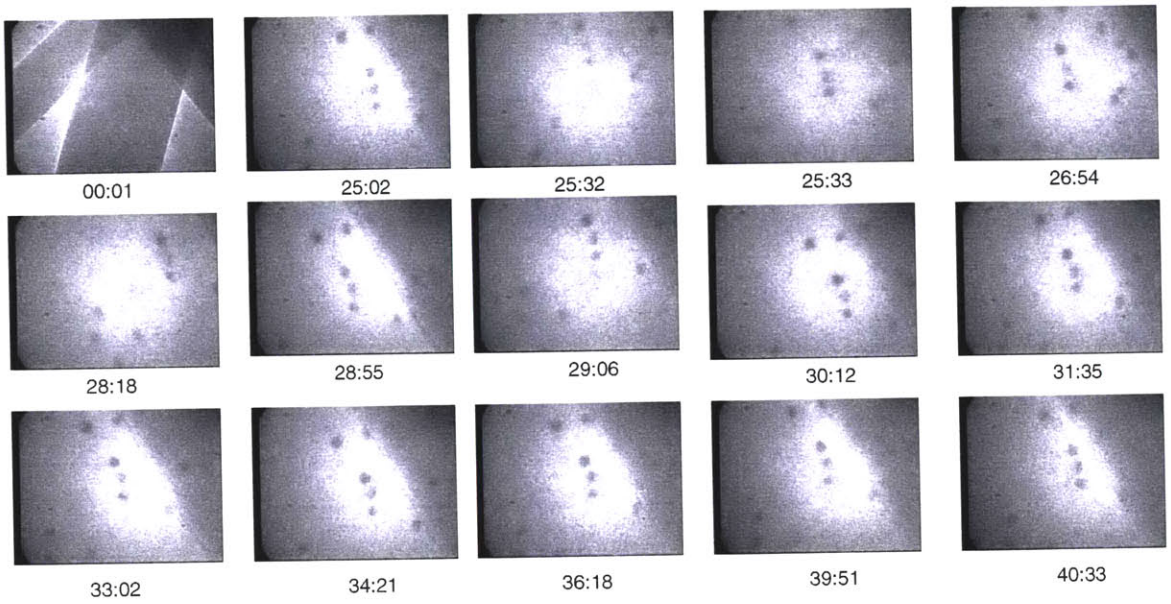

Figure 4-15: TEM images showing the lack of movement of particles as function of time with temperature held constant at 800 °C from 26 minutes until 45 minutes in the in-situ experiments. Magnification was 41kX, with the television adding 15X. The width of the images was approximately 300nm. The image at time 00:01 was taken at a lower magnification.

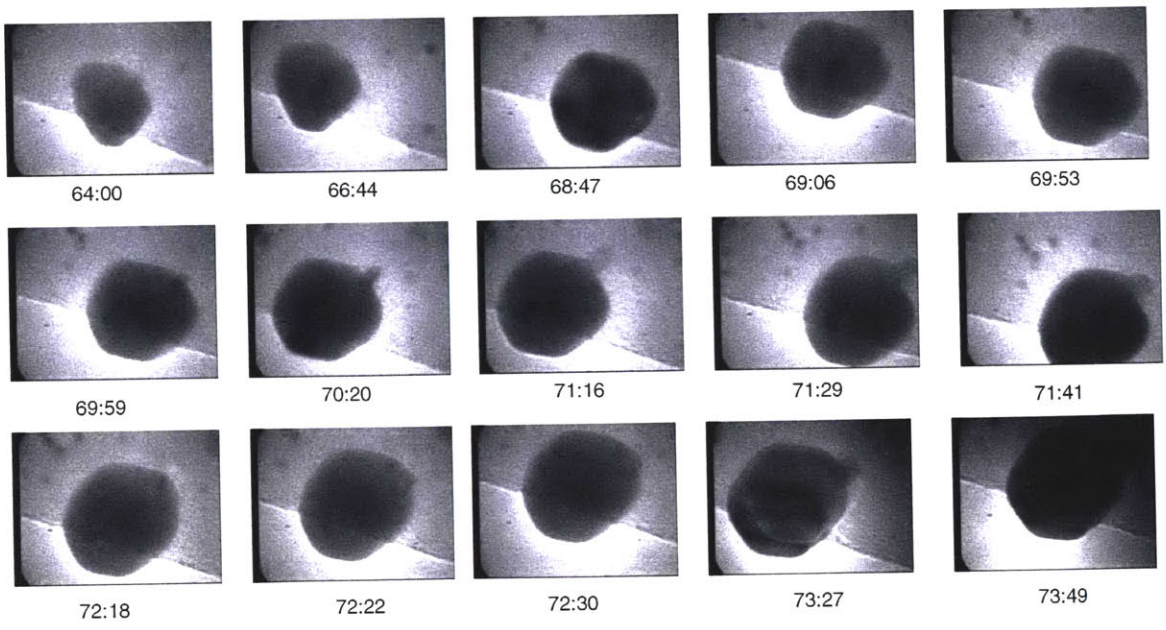

Figure 4-16: In-situ images of particle growth as a function of time shown with plot of corresponding temperature as a function of time. Magnification was 68kX, with 15X added by the television screen. The particle is approximately 100nm across at time 64:00.

At 800°C, the temperature was held constant from time 26:00 until 47:00. During this time, as seen in Figure 4-15, the TEM beam was trained on three small particles that showed no signs of movement or increased diameter. This indicated that in the in-situ environment, particle size was a function of heat treatment temperature, but not a function of time, contradicting data seen in the TEM and SEM when imaging samples baked in the tube furnace. It was concluded that because the vacuum environment of the TEM was the only difference between the two experiments, that the argon environment affected the formation of particles.

Other evidence provided by the in-situ experiments assisted in the understanding of the mechanisms of particle formation and growth. It is important to note there was no significant movement seen by any of the particles visible. Well-established theories of particle coarsening include Ostwald ripening, where one particle shrinks in size while an adjacent gains the mass. Another theory is known as coalescence growth, particles coarsen due to mobile migration and physical contact. **It was clear that for the resolvable particles, there was a lack of particle migration to any visible extent.** It is possible that particles small enough to avoid resolution, however, did migrate. Again, the vacuum environment has affects on the chemistry and particle growth.

4.1.3.2 Cross-sectional TEM Results

Cross-sectional TEM provided important information as to how the particles were distributed throughout the fiber. Prior to this work, it was believed the particles were on the surface of the fiber and that the fibers were round and solid. It was evident from Figure 4-17 below that both of these assumptions were false. Fibers were generally round or elliptical, but were not always solid. Pockets of empty space can clearly be seen in Figure 4-17(a). It is also apparent that the vast majority of small particles did not penetrate the surface of the fiber, and would not be electrochemically active. Often, a center core was less dense with palladium particles, as in Figure 4-17(d). On some occasions, the core had a higher density of particles. **This work concluded that particle nucleation and growth occur within the fiber, and are not surface phenomena.** The information presented was critical in explaining the results from the RDE, detailed a later section.

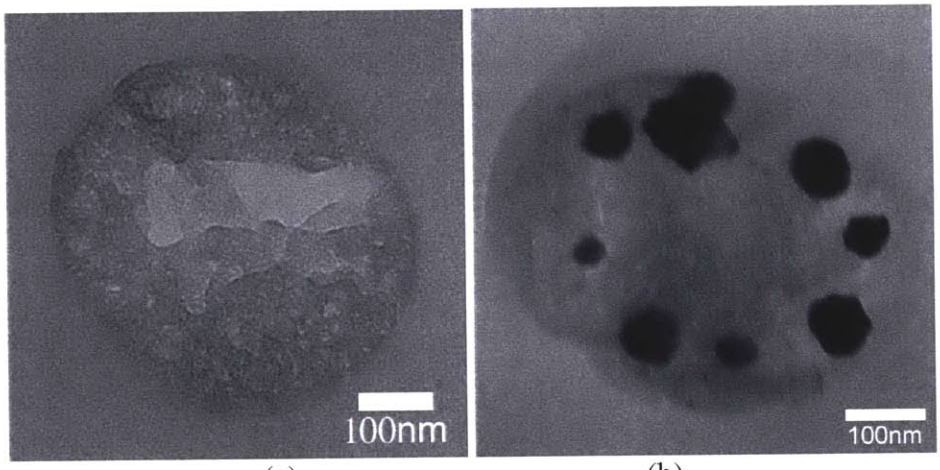

(a) (b)

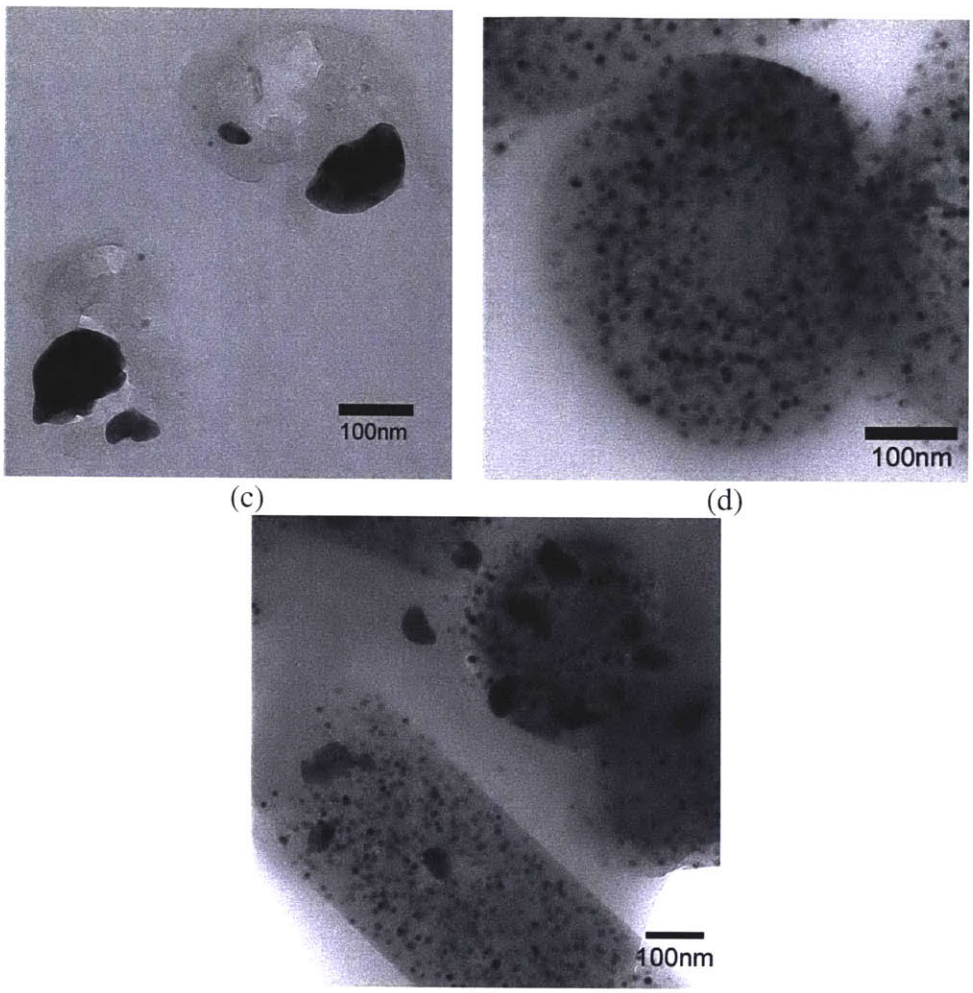

(c) (d)

(e)

Figure 4-17: Cross-sectional TEM images. Figures (a-c) correspond with the same sample in Figure 5-11(b). (a) Sample 9PAN-0.18466Pd/C-900-45min-0.12459mg/cm2, where vacant cavities in the interior of the carbon nanofiber are apparent. This sectional cut hd no large particles by chance. (b) The same sample, with particles dispersed at a similar radius from the center of the fiber and not penetrating the surface. (c) Smaller particles along with larger ones can be seen in this image of the same sample. Fibers are not always perfectly round. (d and e) Sample 9PAN-0.13416Pd/C-900-15min-0.07851mg/cm2 shows a large number of particles between 5-10 nm, however, cross-sectional images prove that almost all of them are embedded within the fiber.

4.1.3.3 High-Resolution TEM Results

The operation of the high-resolution TEM was performed by Paulo Ferreria to look for crystal planes in the palladium particles and carbon fibers. Figure 4-18 through Figure 4-21 are examples of these images. The metallic palladium particles were entirely

crystallite in nature, as seen in Figure 4-18. The presence of lattice fringes caused by crystal planes supported the findings of the XRD study. Larger particles often exhibited fringe patterns of various orientations, indicating **large palladium particles were comprised of several crystal grains.**

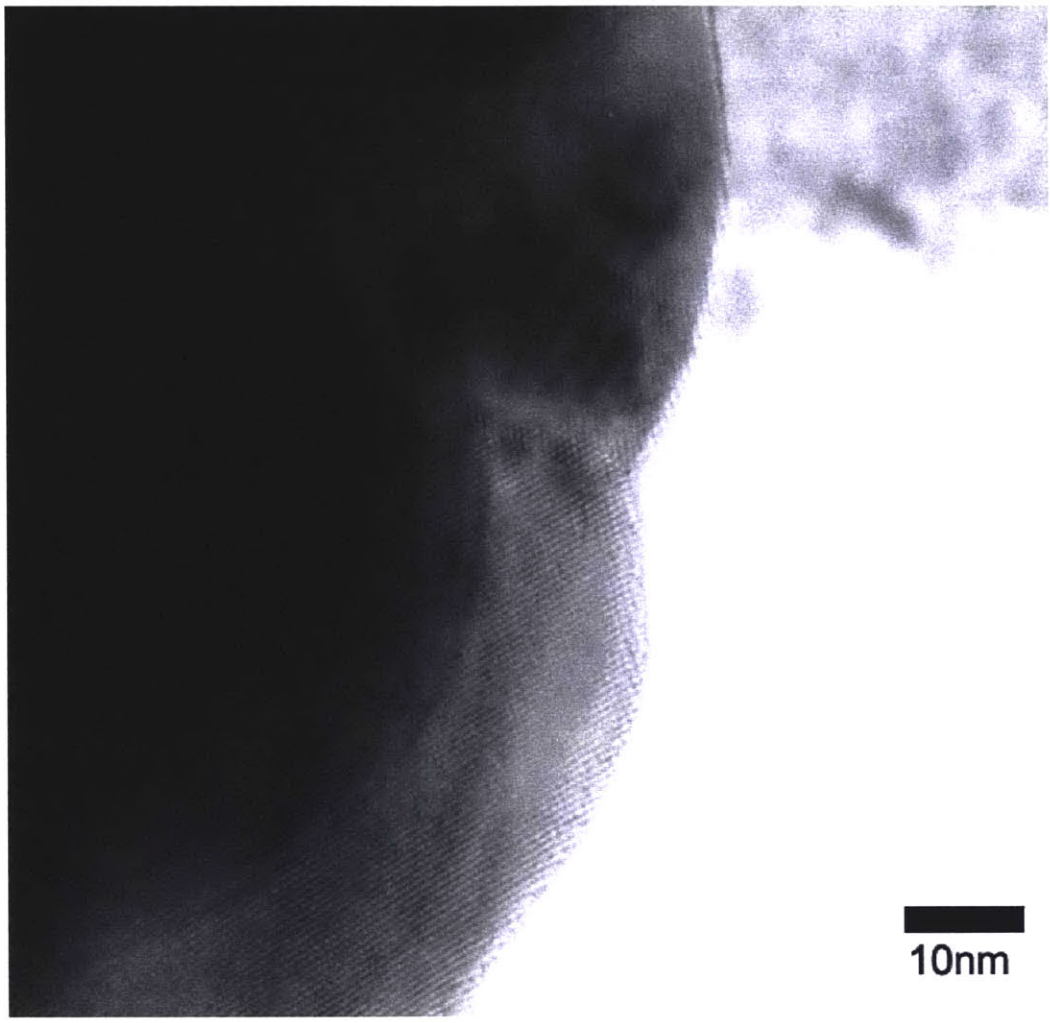

Figure 4-18: A high resolution TEM image of a palladium particle from sample 8PAN-0.02488Pd/C-900-15min-0.03041mg/cm2-8 showing the presence of multiple orientations of crystal lattice planes in a single particle. Imaged by Paulo Ferreria.

As seen in Figure 4-18 through Figure 4-21, carbon fibers displayed no evidence of significant amounts of lattice fringes**,** however, a faint organization could sometimes be located. **It was inferred that there were no significant amounts of graphitic carbon in the carbon nanofibers.**

Figure 4-21was an image of sample 8PAN-0.02488Pd/C-900-15min-0.025913mg/cm2-5 heat treated at 1100°C. Even at this elevated temperature the sample did not demonstrate significant amounts of graphite. XRD data confirmed these findings, as seen in Appendix
Figure 7-7.

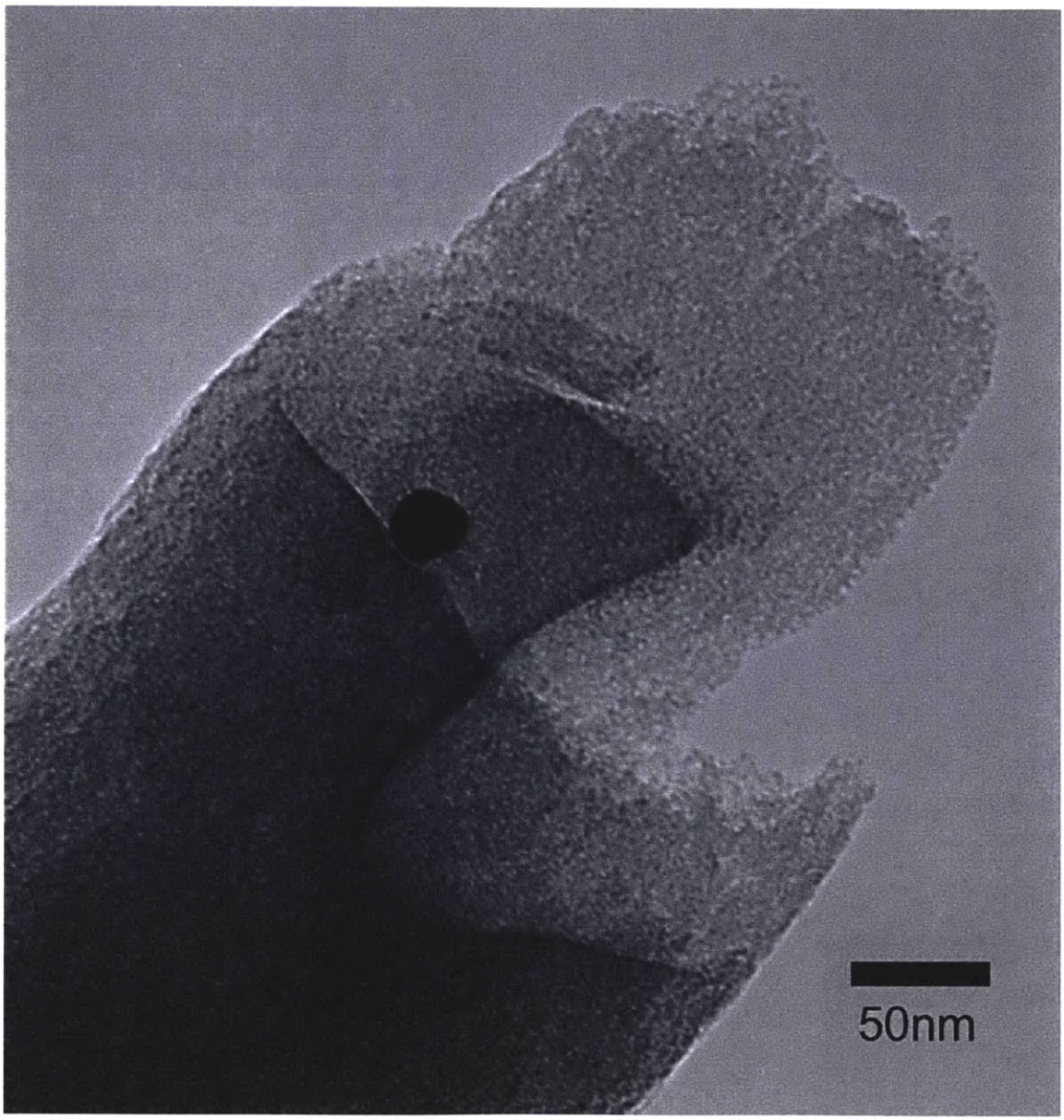

Figure 4-19 A high-resolution TEM image of the tip of a fiber from sample 8PAN-0.02488Pd/C-1100-5min-0.025913mg/cm2-5 showing a "salt and pepper" pattern that

indicates the presence of amorphous carbon. This sample corresponds to the XRD data in Figure C-3. Imaged by Paulo Ferreria.

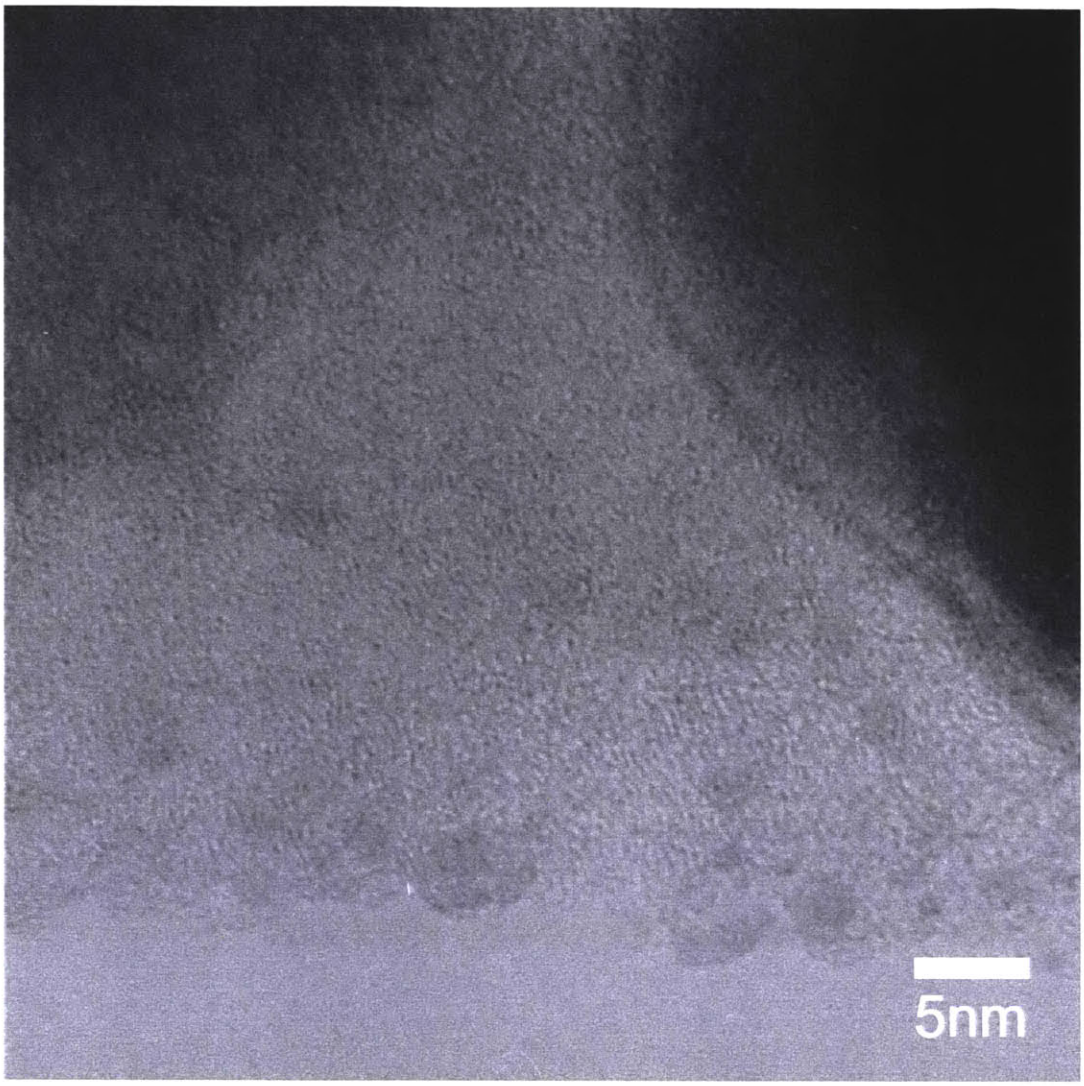

Figure 4-20 A high-resolution TEM image of8PAN-0.02488Pd/C-900-15min-0.03041mg/cm2-8 sample fiber edge showing some ordering of amorphous carbon with some small 5nm palladium particles. Imaged by Paulo Ferreria.

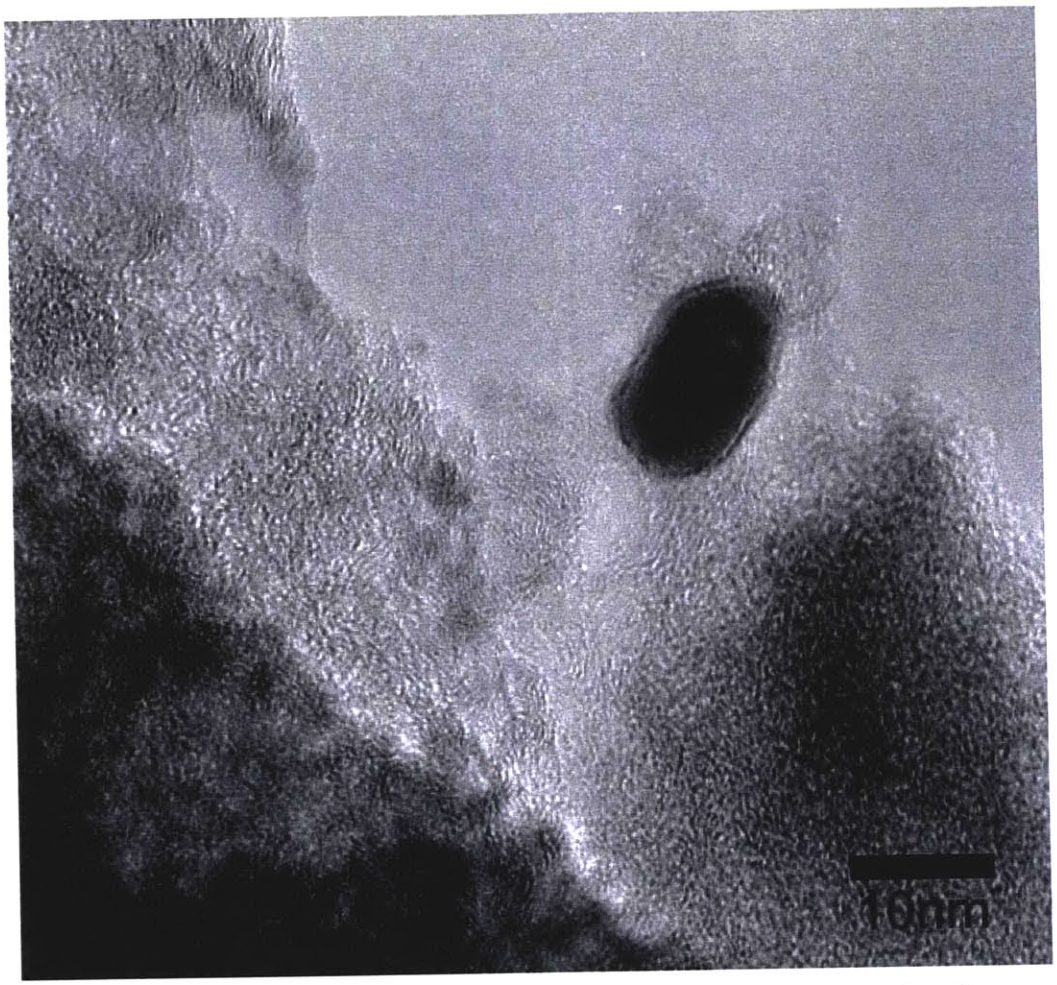

Figure 4-21: A high resolution TEM image of a palladium particle and carbon support from sample 8PAN-0.02488Pd/C-900-15min-0.03041mg/cm2-8, with the faint presence of organization of the carbon crystal structure in the surrounding support. Graphite planes are not distinct, but the fiber is not entirely amorphous. Imaged by Paulo Ferreria.

4.1.4 XANES Results

X-ray absorption near edge structure (XANES) characterization was performed to determine the chemical nature of the material. The additional results are seen below in Figure 4-22. Samples 8PAN-0.02488Pd/C-280-120min-0.019464mg/cm2-2 and 8PAN-0.02488Pd/C-280-120min-0.019464mg/cm2-1.5 (named 2G and 1.5G respectively in Figure 4-22), had only been heated in the muffle oven and show an increased presence of Pd-O. After sample 8PAN-0.02488Pd/C-800-60min-0.019464mg/cm2-2 (referred to as 2GG), was heat treated in the tube furnace, the Pd-O peak shrank, and a pure palladium peak grew as shown in Figure 4-22(b).

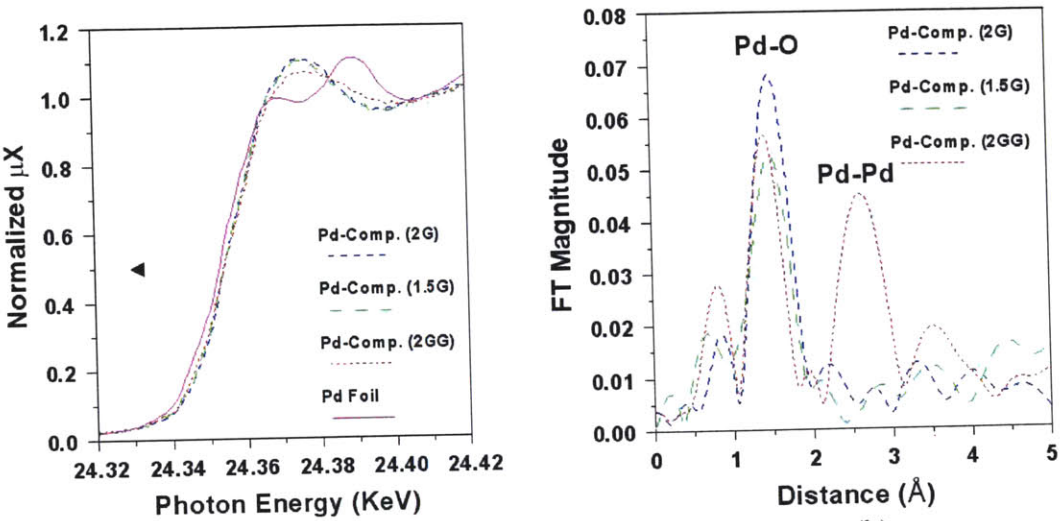

(a) (b)

Figure 4-22: XANES Results. The corresponding labels for the samples are:

2G: 8PAN-0.02488Pd/C-280-120min-0.019464mg/cm2-2
1.5G: 8PAN-0.02488Pd/C-280-120min-0.019464mg/cm2-1.5
2GG: 8PAN-0.02488Pd/C-800-60min-0.019464mg/cm2-2

(a) A comparison of XANES of electrode along with that of metallic palladium foil. The data indicated palladium in the nanocomposite is present in an oxidized form relative to metallic palladium. (b) A comparison of phase uncorrected Fourier transforms of k^3-weighted extended X-ray absorption fine structure (EXAFS) of some palladium nanocomposite along with that for metallic palladium foil. The Pd-Pd contribution from the foil is very strong compared to that from the nanocomposite labeled 2GG. The Pd-Pd interaction in the nanocomposite must be further substantiated. Figures courtesy of Dr. Azzam Mansour of the Naval Surface Warfare Center.

4.2 Physical Properties

The bulk physical properties of the several electrodes were investigated using a microprobe station to test the electrical resistivity. The results were portrayed in Figure 4-23. It was demonstrated that resistivity is a function of heat treatment time and temperature. **As heat treatment time increased, resistivity decreased,** as shown by the general downward trend of all samples in Figure 4-23. The electrode thickness was taken into accounted.

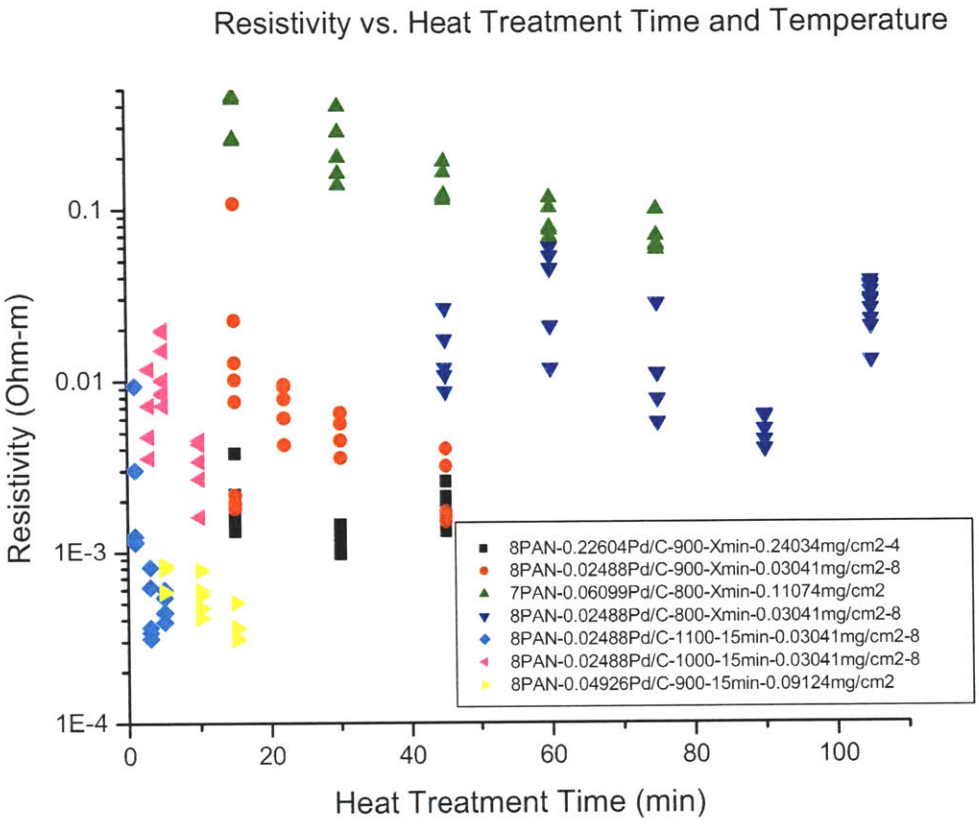

Figure 4-23: Plot of bulk resistivity as measured by the microprobe station vs. heat treatment time and temperature showing a general decreasing trend in resistivity as heating time increases or heating temperature increases. Five readings were taken for each sample at different points throughout the electrode. Error may be contributed by varying thicknesses of the electrode at different points where probe insertion took place, as well as slightly varying contact resistances between the probes and the sample due to environmental vibration. Samples heat treated for very short periods of time, such as the 8PAN-0.02488Pd/C-1000-Xmin-0.03041mg/cm2-8, show higher range of error as well.

Figure 4-23 displays that samples heat treated at 800°C, such as 8PAN-0.02488Pd/C-900-15min-0.03041mg/cm2-8, have resistivities around 0.01-0.1 Ohm-meters. Samples treated at 900°C demonstrated resistivity values on the order of 10^{-3} Ohm-m. Sample 8PAN-0.04926Pd/C-900-15min-0.09124mg/cm2, treated at 1000oC had a resistivity on the order of 10^{-4} Ohm-m. This compared well with results from literature [60].

Another physical property often reported when describing electrodes is durability and structural integrity. **All electrodes fabricated were free-standing** and could be handled

with tweezers without falling apart. In general, electrodes were more robust when electrospun thicker. After heat treatment in air environment at 280°C, samples were flexible. After tube furnace heat treatment, samples were more brittle and delicate, but still flexible and free-standing.

4.3 Electrochemical Properties

4.3.1 Cyclic Voltammetry (CV) Results

To ensure the electrochemical setup was functioning properly, electrodes that had known performance and/or published electrochemical data were tested. The CV of a polished palladium disk was seen below in Figure 4-24.

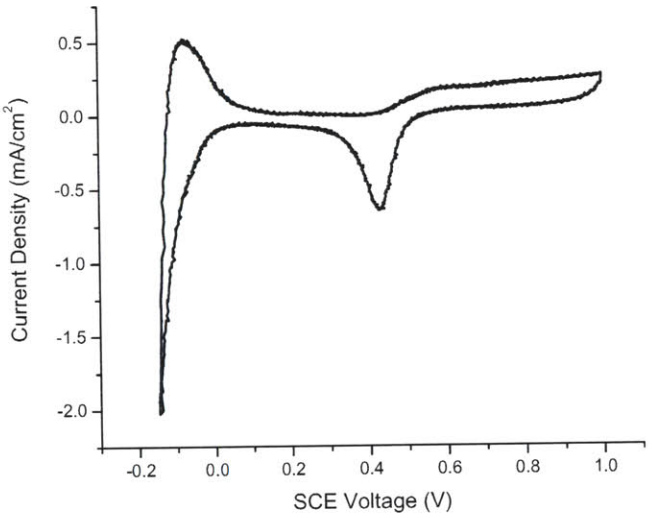

Figure 4-24: CV of polished palladium disk in N_2 saturated 0.1 M H_2SO_4 at 0 RPM with a sweep rate of 50mV/sec. This curve's shape and peak heights matched that reported in literature[64].

The peaks corresponded with electrochemical activity. For a positive sweep starting from lower voltage values and moving right, the first peak at -0.1 V SCE was the hydrogen desorption peak. If the surface of the catalyst was a thin film or very smooth

and pure, multiple peaks could be distinguished for desorption of monolayers of various strengths. The reaction corresponding with the hydrogen desorption peak was:

$$H_{ads} \rightarrow H^+ + e^- \tag{4.9}$$

Sweeping to higher voltages, oxide formation (of PdO) was encountered. This peak could be represented with the following chemical reaction:

$$H_2O \rightarrow O_{ads} + 2H^+ + 2e^- \tag{4.10}$$

The oxide formation region could be divided into two peaks that are often distinguishable. At around 0.5 V SCE, the following reaction occurred:

$$Pd + H_2O \rightarrow PdOH + H^+ + e^- \tag{4.11}$$

A second small bump was seen around 0.8 V SCE. The second peak in the oxide formation region corresponded to the following reaction:

$$PdOH \rightarrow PdO + H^+ + e^- \tag{4.12}$$

The voltage sweep then reached its set maximum of 1.0V and reversed direction. At around 0.45 V SCE in Figure 4-24, the oxide reduction region was reached. Here, PdO was reduced, and the following general reaction occurred:

$$O_{ads} + 2H^+ + 2e^- \rightarrow H_2O \tag{4.13}$$

At oxide 0.45 V SCE where the reduction peak occurred, both reactions in Equations (4.11) and (4.12) occurred in reverse.

Finally, the cathodic hydrogen region peaks occurred at the same potential as the hydrogen desorption peaks from the reaction in Equation (4.9). The hydrogen adsorption reaction was:

$$H^+ + e^- \rightarrow H_{ads} \tag{4.14}$$

The gap between the values for the positive sweep and the negative sweep were the result of the electrical double-layer capacitance on the surface of the catalyst. From the testing of the palladium disk electrode, it was found that 0.1 M H_2SO_4 worked well in the setup and was reported often in literature for CV and RDE applications.

Following setup calibration, carbon nanofiber electrodes were mounted with diluted Nafion solution onto the glassy carbon disk of the rotating disk electrode as described in Section 3.4.5.2. A carbon nanofiber electrode prepared with no palladium salt was fabricated to serve as a control sample in experimentation. The electrochemical performance of sample 10PAN-0Pd/C-900-15min-0mg/cm2 is shown below in Figure 4-25.

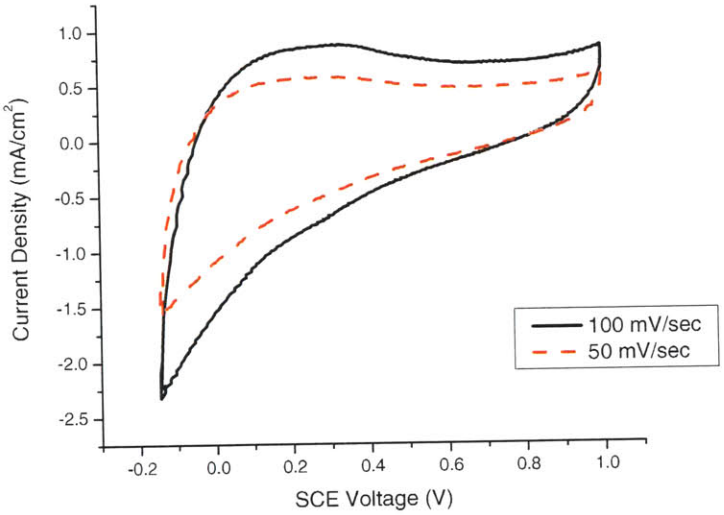

Figure 4-25: CV of unloaded carbon nanofiber control sample 10PAN-0Pd/C-900-15min-0mg/cm2 at 100 and 50 mV/sec in N_2 saturated 0.1M H_2SO_4.

To determine the electrochemical effect of adding palladium to the carbon nanofiber electrodes, sample 8PAN-0.22604Pd/C-900-Xmin-0.10368mg/cm2-6 was tested and the results were shown below in Figure 4-26 and Figure 4-27. The setup and mounted nanofiber electrode were experimented with to find an optimal sweep rate. It was established that the lowest sweep rate of 10mV/sec produced more refined activity peaks, as seen in Figure 4-27.

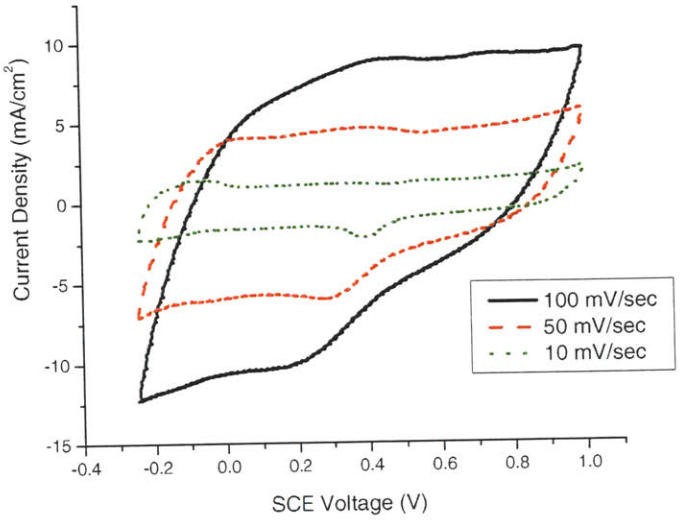

Figure 4-26: CV of sample 8PAN-0.22604Pd/C-900-15min-0.10368mg/cm2-5 demonstrationg that increased sweep rate results in lower currents but more peak definition. Sample was tested in 0.1M H_2SO_4 and used 10 mL of 200:1 Isopropanol:Nafion solution with rotation rate of 0 RPM.

Similar to the CV of pure palladium from Figure 4-24, sample 8PAN-0.22604Pd/C-900-Xmin-0.10368mg/cm2-6 treated at 15, 30, and 45 minutes exhibited hydrogen adsorption and desorption peaks along with oxide formation and reduction peaks. For the 15 minute sample, hydrogen adsorption and desorption peaks were well defined.

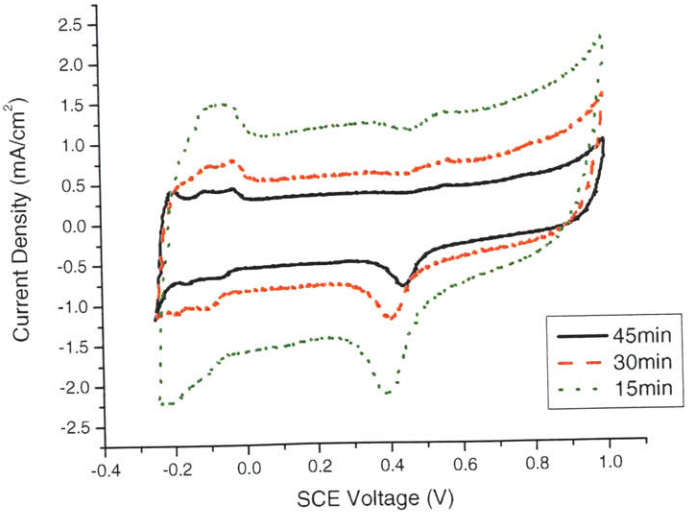

Figure 4-27: CV of sample 8PAN-0.22604Pd/C-900-Xmin-0.10368mg/cm2-5 adhered using 200:1 Isopropanol:Nafion solution, tested in N_2 saturated 0.1M H_2SO_4 at 0 RPM

with a scan rate of 10mV/sec. The 15 minute sample corresponds to the TEM image in Figure 4-10.

In Figure 4-27, the electrochemical activity decreased as heat treatment time increased. A plausible explanation for the exhibited behavior was that the fibers were thin with a high loading and large particles formed quickly, resulting in a decrease of catalyst surface area. Figure 4-10 showed that after only 15 minutes, many large particles had formed that were around 100nm in diameter, which was almost half a fiber diameter. As heat treatment time increased, particles grew larger according to the trend established in 4.1.3 with TEM and in Figure 4-8 with XRD. Particle growth could be explained by the CV in Figure 4-27. As heat treatment time increased, the hydrogen adsorption and desorption peaks characteristic of thin films disappeared, so the CV looked more like thick, bulk palladium that would result from larger particles. As particles grew, catalyst surface area decreased and electrochemical activity decreased concurrently.

From the analysis of area beneath the hydrogen adsorption peaks of the CV data, information could be gathered about the catalyst surface area. The following Figure 4-28 was an example of a typical first hydrogen adsorption peak analyzed.

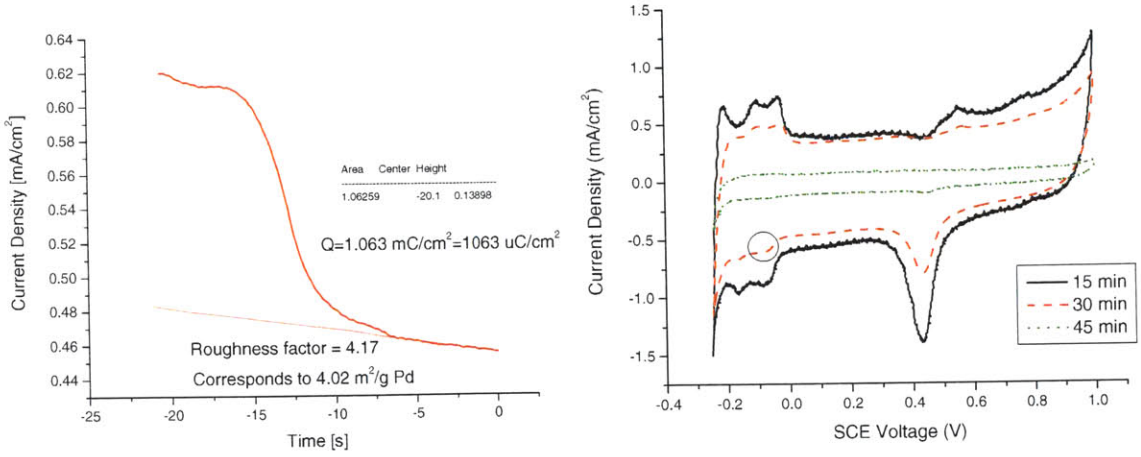

(a) (b)

Figure 4-28 (a,b): (a) Analysis of the hydrogen adsorption first peak of sample 8PAN-0.22604Pd/C-900-30min-0.10368mg/cm2-6, corresponding to the circled peak in (b), mirrored on x-axis.

The catalyst surface area data from sample 8PAN-0.22604Pd/C-900-Xmin-0.10368mg/cm2-6 can be summarized below in Table 4-1. A clear trend was displayed. Detailed calculations are shown in Appendix F.

Table 4-1: Electrochmically active surface area as a function of heat treatment time for sample 8PAN-0.22604Pd/C-900-Xmin-0.10368mg/cm2-6.

Heat Treatment Time (min)	Electrochemically Active Area (m^2/g)
15	7.17
30	4.02
45	1.23

As heat treatment time increases, electrochemically active surface area decreases for sample 8PAN-0.22604Pd/C-900-15min-0.10368mg/cm2-6. The CVs for this sample were shown in Figure 4-27. **The electrochemical surface area per gram catalysts for the carbon nanofiber electrode was 7.17 m^2/g catalyst, while state-of-the-art systems are around 70m^2/g [12].** The lower values from the fabricated carbon nanofiber electrodes were expected because particle sizes on the order of single nanometers exist in carbon black, while the electrospun nanofiber electrode had larger diameter particle sizes.

Tests of sample 8PAN-0.22604Pd/C-900-15min-0.10368mg/cm2-5 were performed at various solution temperatures and the results were displayed in Figure 4-29. The reference electrode was not rated above 80°C, therefore temperatures were kept modest. A trend is seen that for increasing solution temperature, a sample's activity increases.

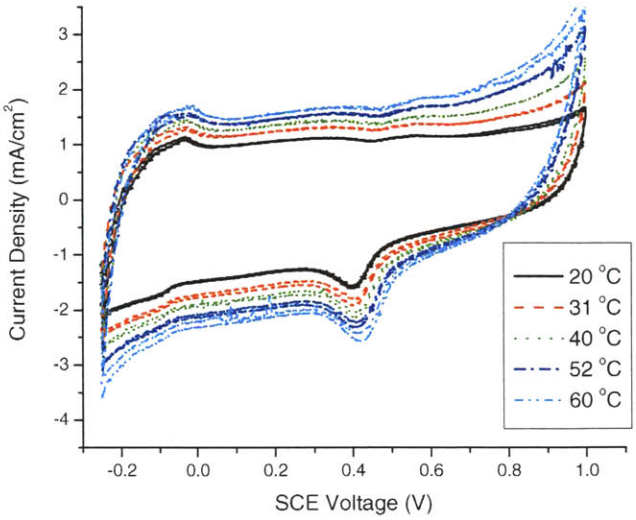

Figure 4-29: CV of sample 8PAN-0.22604Pd/C-900-15min-0.10368mg/cm2-5 in N_2 saturated 0.1 M H_2SO_4 at 0RPM and scan rates of 25mV/sec demonstrating electrochemical activity as a function temperature.

Sample 9PAN-0.18466Pd/C-900-Xmin-0.15948mg/cm2-9 was tested for electrochemical performance for comparison. The resulting CV curves were displayed below in Figure 4-30. For this sample, as heat treatment time increased, activity increased. This was opposite of the trend seen in Figure 4-27.

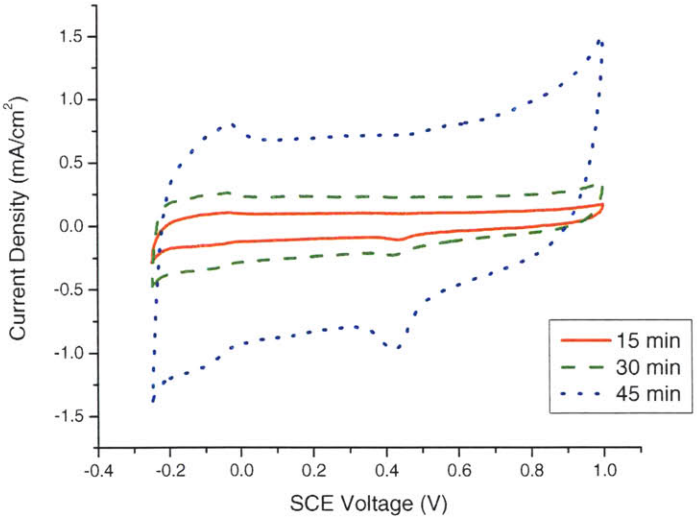

Figure 4-30: CV of sample 9PAN-0.18466Pd/C-900-Xmin-0.15948mg/cm2-9 heat treated at 15, 30, and 45 minutes at 900 °C and tested in N_2 saturated 0.1M H_2SO_4 with 10µL of 100:1 Isopropanol:Nafion solution at 10mV/sec.

TEM images of sample 9PAN-0.18466Pd/C-900-Xmin-0.15948mg/cm2-9 in Figure 4-9 and cross-sectional images in Figure 4-17(a-c) showed that fibers were over 400 nm thick, and as heat treatment time increased, more particles breached the surface of the fiber. The smaller particles in Figure 4-9(a) nucleated within the fiber and were not electrochemically active, which explained the trend seen of increasing activity with increasing heat treatment time. It is noteworthy that sample 9PAN-0.18466Pd/C-900-Xmin-0.15948mg/cm2-9 in Figure 4-30 actually has a smaller oxide reduction peak than sample 8PAN-0.22604Pd/C-900-Xmin-0.10368mg/cm2-6 in Figure 4-27, despite having a higher loading of palladium in mg/cm^2.

To confirm the hypothesis that sample 9PAN-0.18466Pd/C-900-Xmin-0.15948mg/cm2-9 displayed increasing activity with increasing heat treatment due to larger particles penetrating the carbon nanofiber surface, a similar sample (9PAN-0.18466Pd/C-900-Xmin-0.15948mg/cm2-7) was heat treated further and tested electrochemically. A comparison of both samples was shown below in Figure 4-31.

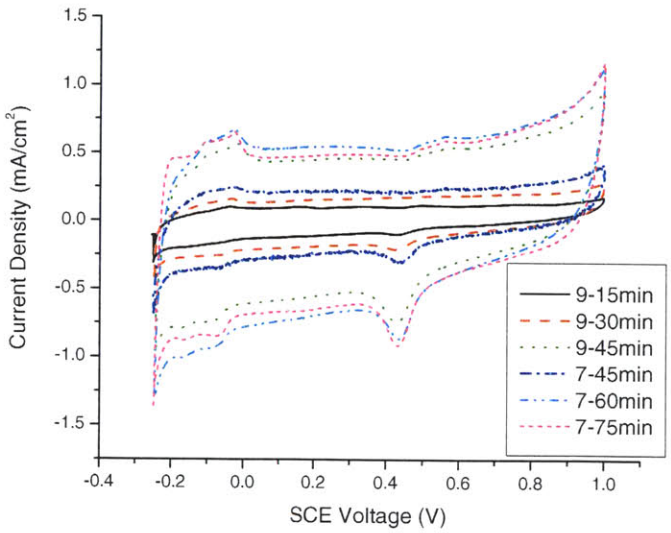

Figure 4-31: CV of sample 9PAN-0.18466Pd/C-900-15min-0.12459mg/cm2-7 and -9 in N_2 saturated 0.1M H_2SO_4 at 10mV/sec displaying that as heat treatment time increased, activity increased. Samples were labeled with the electrode number and heat treatment time at 900°C. This evidence was corroborated with findings from the TEM.

As heat treatment time increased, the activity plateaued as shown by the 60 and 75 minutes samples in Figure 4-31. TEM images of sample 9PAN-0.18466Pd/C-900-Xmin-0.12459mg/cm2-9 heat treated at 15 and 45 minutes at 900°C are shown in Figure 4-9. Activity increased as heat treatment time increased because more particles penetrated the surface of the carbon fiber, until at longer temperatures (60, 75min), the particle growth decreased surface area per unit volume and the trend faded.

One discrepancy seen is that the two samples show a large difference in activity when heat treated at 900°C for 45 minutes. Further TEM analysis of sample 9PAN-0.18466Pd/C-900-Xmin-0.12459mg/cm2-7 yielded the following images in Figure 4-32.

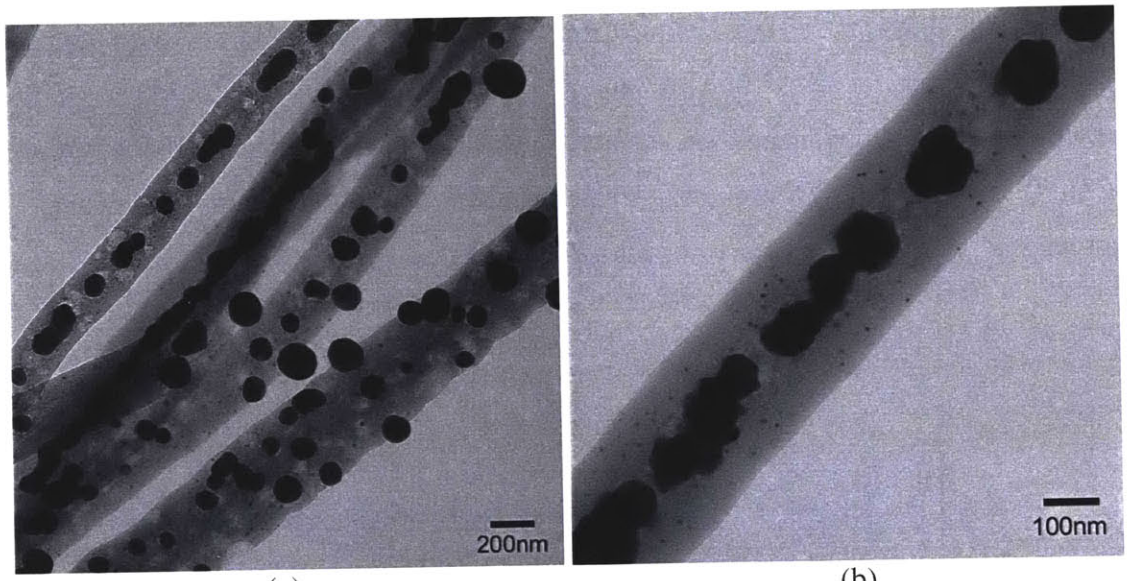

(a) (b)

Figure 4-32 (a,b): TEM images of sample 9PAN-0.18466Pd/C-900-45min-0.12459mg/cm2-7 show that some fibers contained an ordered distribution of particles within the center of the fiber.

Figure 4-32 demonstrated that many of the particles appear to be located in the center of the fiber. This core effect was seen in sample 9PAN-0.18466Pd/C-900-45min-0.12459mg/cm2-7 and to a far lesser extent in sample 9PAN-0.18466Pd/C-900-45min-0.12459mg/cm2-9. This structure was present in many of the fibers of the sample, but not all. The formation of core particles explained why sample 9PAN-0.18466Pd/C-900-45min-0.12459mg/cm2-7 has lower activity than sample 9PAN-0.18466Pd/C-900-45min-0.12459mg/cm2-9.

A more extreme example of a case where a fiber had numerous particles yet little activity was sample 9PAN-0.13416Pd/C-900-15min-0.07851mg/cm2. Electrochemical data for this sample were seen below in Figure 4-33.

As shown in Figure 4-13(a-d), TEM images of sample 9PAN-0.13416Pd/C-900-15min-0.07851mg/cm2 showed a plethora of small particles that should have expressed a large surface area. However, cross-sectional TEM images of the same sample in Figure 4-17(d) and (e) show that the vast majority of particles were within the fiber. Because the particles were encapsulated by carbon, the particles were inactive and the CV of sample 9PAN-0.13416Pd/C-900-15min-0.07851mg/cm2 in Figure 4-33 had a similar shape and low current density exhibited in the CV of plain carbon nanofibers seen in Figure 4-25.

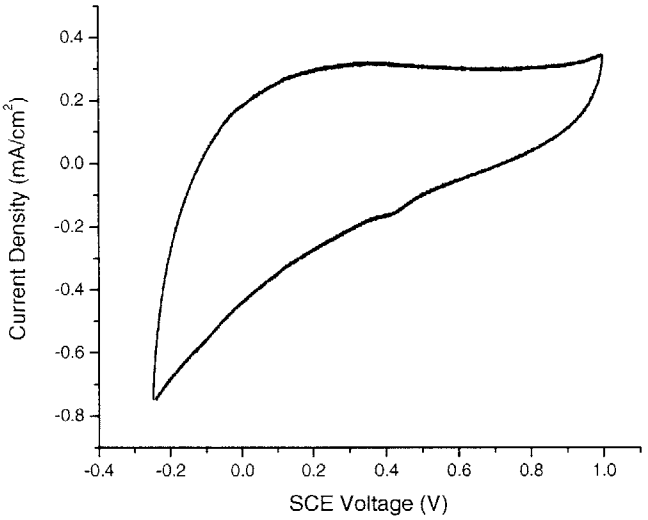

Figure 4-33 CV of sample 9PAN-0.13416Pd/C-900-15min-0.07851mg/cm2 tested in N2 saturated 0.1M H_2SO_4 with 10μL of 200:1 Isopropanol:Nafion solution with a sweep rate of 50mV/sec. The CV curve was comparable to plain carbon in Figure 4-25, but had a very feint peak at 0.4V where oxide reduction occurred. CVs of this sample with sweep rates of 10mV/s had similar shapes and lacked palladium peaks.

All of the CV work concluded that electrochemical performance was a function of the surface area of the catalyst. **The exposed electrochemical area was a function multiple**

parameters, including heat treatment time, heat treatment temperature, fiber thickness, electrode thickness, and catalyst loading. Tradeoffs and benefits existed between these parameters in the engineering of the nanofiber electrode. As concluded earlier, particle size and growth rate were a function of heat treatment time, heat treatment temperature, and fiber diameter. Thicker fibers yielded smaller particles, but the particle nucleation occurred more often within the fibers. Larger particles had less surface area per unit volume, but had higher probability of penetrating the fiber surface and being active. Naturally, thicker electrodes and higher loaded samples were more electrochemically active if other variable were held constant.

4.3.2 Rotating Disk Electrode (RDE) Results

All samples tested with cyclic voltammetry in an N_2 saturated acidic solution were also tested while rotating in an O_2 saturated solution in an RDE setup. RDE examines the oxygen reduction reaction in Equation 1.8, which is the same half reaction in a PEM fuel cell. A typical example of a scan in O_2 saturated H_2SO_4 is shown below in Figure 4-34.

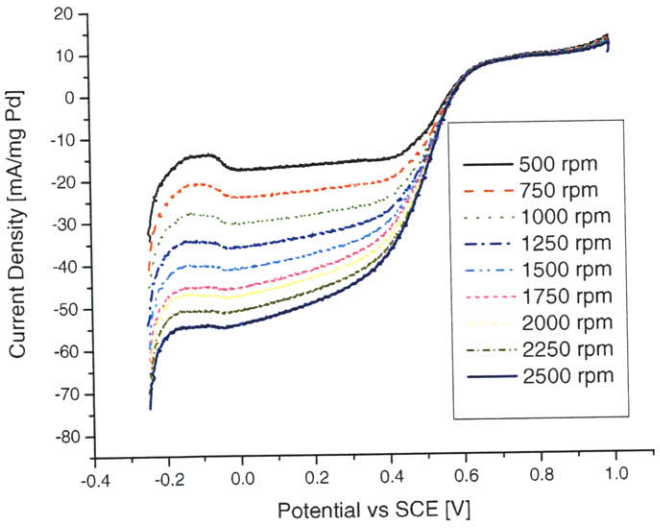

Figure 4-34: RDE of sample 8PAN-0.22604Pd/C-900-15min-0.10368mg/cm2-6 adhered with 10 μL of 200:1 Isopropanol:Nafion solution tested in O_2 saturated 0.1 M H_2SO_4 at a scan rate of 25mV/sec.

Figure 4-34 clearly displays the increase of activity as rotation rate increased. The data from Figure 4-34 and other plots like it could be analyzed to determine the limiting kinetic current, number of electrons involved in the reaction, exchange current density, and Tafel slope. Plots like Figure 4-35 are called Koutecky-Levich (K-L) plots.

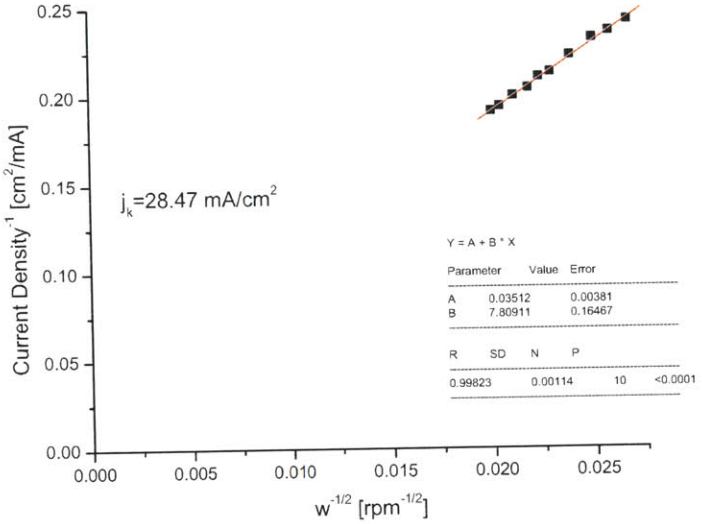

Figure 4-35: Typical K-L plot of sample 8PAN-0.22604Pd/C-900-15min-0.10368mg/cm2-6 at around 0.42 V SCE with 10 data points taken from rotation rates between 1400-2500 RPM. The limiting kinetic current was 28.47mA/cm2. Analysis by Simcha Singer.

The results from the analysis of several K-L plots are listed below in Table 4-2. The y-intercept of K-L plots yielded the inverse of j_k, the exchange current density. This value indicates how the electrode would perform in the absence of mass transfer effects.

Table 4-2: RDE Results of sample 8PAN-0.22604Pd/C-900-Xmin-0.10368mg/cm2-6 heat treated at 15, 30, and 45 minutes at 900°C. Data made possible by the analysis work of Simcha Singer.

HT time (@ 900C)	j_k (mA/cm2)	j_k (mA/mg Pd)	Tafel Slope at low overpotential	Number of electrons (determined at 0.42 V)	Cat. Surf. Area (m^2/mg) These are N_2 - not at specific voltages	Exchange Current Density A/cm^2_{real}
15	28.47(at 0.42 V vs SCE)	15.33 (at 0.55 V vs SCE)	-62 mV/decade	~4.09	7.17	1.005 $x10^{-12}$
30	15.79 (at 0.42 V vs SCE)	10.97 (at0.55 V)	-81 mV/decade	3.5	4.02	Order~ (10^{-10})
45	13.36 at 0.42V	---	-56 mV/decade	2.57	1.23	3.78 $x10^{-13}$

Several trends were noted in RDE experimentation. For sample 8PAN-0.22604Pd/C-900-Xmin-0.10368mg/cm2-6, kinetic limiting current (j_k) decreased as time increased. In addition, the number of electrons involved in the reaction decreased as time increased, indicating that the reaction gradually produces more hydrogen peroxide, which has a negative effect on performance.

The CV and RDE experiments gave a fair indication of the electrochemical performance of the nanofiber electrodes. However, there are other factors involved in designing a well-performing fuel cell electrode besides catalyst surface area found by the CV and RDE. Fuel cell operation adds complications such as fuel mass diffusion; hydrophobicity and water management; structural and thermal stress; chemical poisoning and catalyst degradation; and activation, ohmic, and mass transfer overpotentials. Further testing of the electrospun carbon nanofiber electrodes was performed in a PEM fuel cell to gain further understanding.

4.3.3 PEM Fuel Cell Results

Sample 9PAN-0.18466Pd/C-900-15min-0.15948mg/cm2-10 was mounted and tested in a PEM fuel cell apparatus. This sample was similar to sample 9PAN-0.18466Pd/C-900-60min-0.15948mg/cm2-5 with characterization data Figure 4-31(60 min). The results of the fuel cell testing were shown below in Figure 4-36.

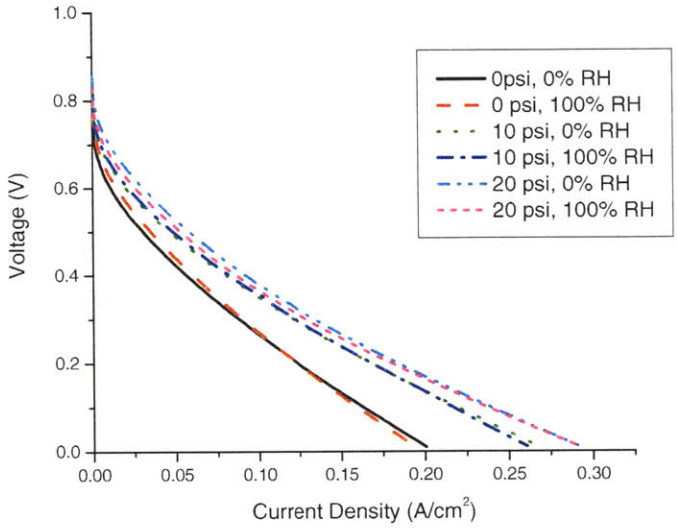

Figure 4-36: Sample 9PAN-0.18466Pd/C-900-15min-0.15948mg/cm2-5 in H2/O2 Fuel Cell Tested at 80 ^{o}C and varying inlet pressure (gauge) with the humidifier on (100% RH) or off (0% RH). Fuel cell testing station operated by Jungik Kim.

To compare the fuel cell results of sample 9PAN-0.18466Pd/C-900-15min-0.15948mg/cm2-10 to commercially available electrodes, E-TEK's 0.5mg Pt/cm^2 low-temperature electrode and GDL was investigated under similar fuel cell testing conditions. Results were displayed in Figure 4-37.

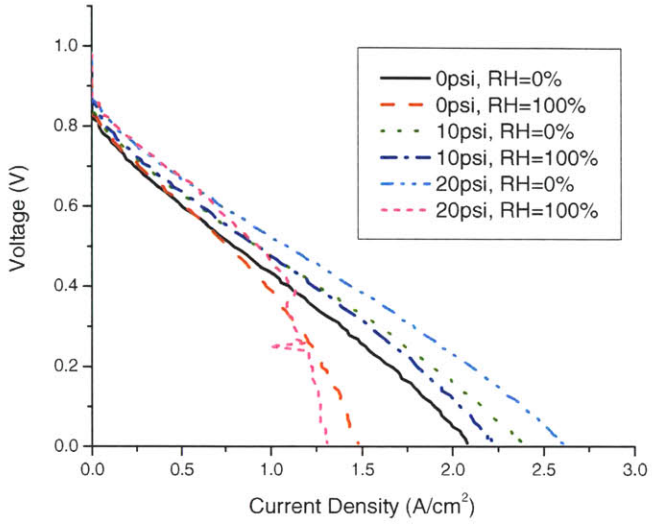

Figure 4-37: A fuel cell i-V performance curve of E-TEK Electrode with platinum loading of 0.5 mg/cm2 tested at 80°C with varying inlet conditions. Cell most likely flooded at 20psi and 100% RH.

While testing conditions in the fuel cell were the same, the E-TEK electrode was hot-pressed in preparation while the carbon nanofiber electrode was not. This could have accounted for better internal contacts and therefore better performance.

Figure 4-38demonstrates the differences in performance on a catalyst weight basis. This comparison is not entirely representative because platinum has a higher catalytic activity than palladium.

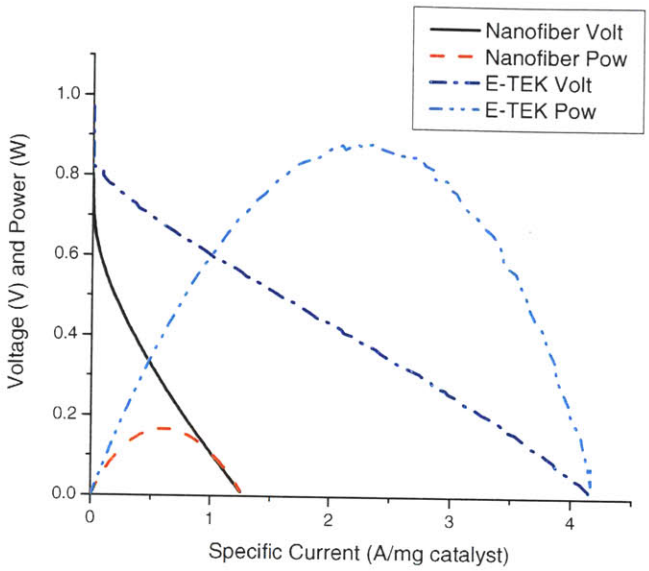

Figure 4-38: Fuel cell i-V and power curves comparing sample 9PAN-0.18466Pd/C-900-15min-0.15948mg/cm2-10 with commercial fuel cell electrode from E-TEK (0.5 mg Pt/cm2) at 0psi and 0%RH.

It was important to note that the E-TEK electrode used platinum metal while the carbon nanofiber electrode used palladium, a less active catalyst. From the data presented in Figure 4-39, it was demonstrated that the nanofiber electrode with palladium was around 20% as active. Taking into account that the E-TEK electrode had platinum metal that was less active than platinum, it can be concluded that the new technology developed to electrospin carbon nanofiber electrodes had comparable performance on a cost basis. Figure 4-39 and Figure 4-40 compared the commercial electrode with the electrospun nanofibers with cost per unit power as a function of efficiency. Fuel cell efficiency was defined as:

$$\eta = \frac{E_{Measured}}{E_{Theotretical}} \tag{4.19}$$

where $E_{Measured}$ was the measured voltage and $E_{Theoretical}$ was the theoretical voltage calculated from Equation 1.3 given the conditions of temperature and pressure. The costs of each electrode were calculated using May 2005 market prices of $871.00/troy oz. of platinum and $193.00 /troy oz. of palladium. The electrodes were 1cm^2 each, and two were used per MEA.

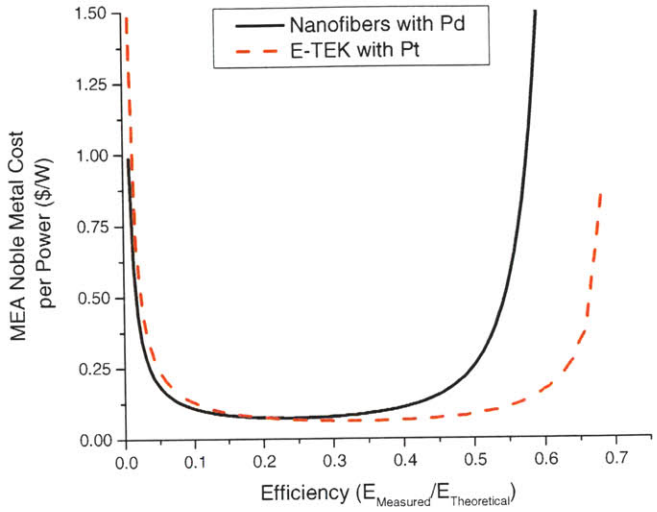

Figure 4-39: Plot of MEA metal cost per Watt as a function of fuel cell efficiency for sample 9PAN-0.18466Pd/C-900-15min-0.15948mg/cm2-10 and E-TEK Pt electrode tested in a PEM fuel cell at 0psi (gauge) and 0% RH. The theoretical open circuit voltage for these conditions was 1.17V.

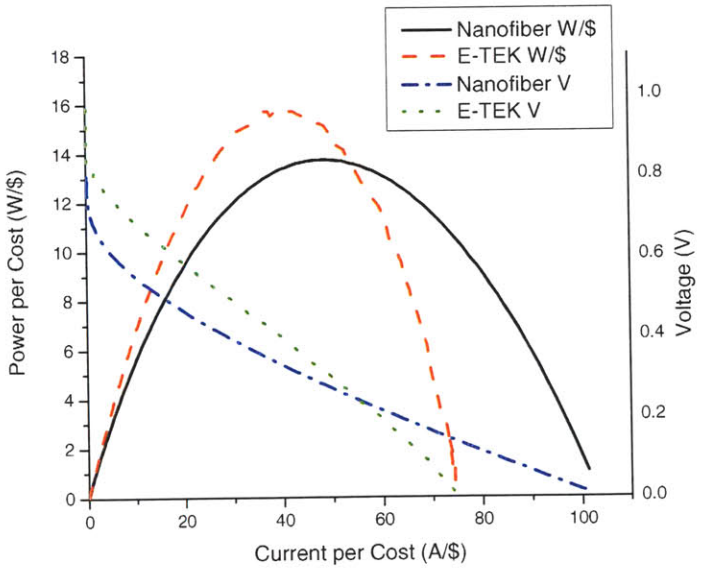

Figure 4-40: Plot of power per cost as a function of current per cost. It is clear that at higher values of current per cost, the nanofiber electrode is superior, but the E-TEK electrode has a higher overall value of Watts per dollar.

It was shown that sample 9PAN-0.18466Pd/C-900-60min-0.15948mg/cm2-10 exhibited performance that was comparable to the commercially available E-TEK electrode. At low efficiencies, when the current draw is high, the nanofiber electrode is actually cheaper per Watt. However, the lines in Figure 4-39 intersect at 0.205 and at greater efficiency, the commercial electrode is cheaper per unit power. With further experimentation and engineering of the fabrication parameters of the electrospun sample, it is very likely an electrode with identical or better performance can be implemented.

It should be noted that all economic performance comparisons were calculated based on costs of metal, neglecting manufacturing costs. Traditionally, fuel cell electrode assembly is discontinuous, requiring multiple steps and manual labor. Electrospinning is much simpler and can be implemented to output large quantities on a continuous production line, possibly making the overall cost cheaper.

5 CONCLUSION

This research focused on the development of a novel oxygen reduction electrode for use in fuel cells and metal-air batteries. The technique of electrospinning was utilized to fabricate a porous, non-woven, carbon nanofiber mesh to support palladium nanoparticles. Electrospinning was a versatile, flexible, and continuous manufacturing process that could be automated for economical electrode production. Variable processing parameters of the electrospinning experiment included: Applied voltage, plate-to-plate distance, capillary tip protrusion distance, substrate material, solution flow rate, amount of solution spun, solution polymer concentration, noble metal salt concentration, and solution temperature, to name a few.

Post-processing of the as-spun nanofibers included a stabilization heat treatment in air environment up to 280°C for 2 hours, followed by a carbonization heat treatment in grade 5.0 argon environment to temperatures between 800 and 1100 °C for varying times. The stabilization step prepared the samples to be heat treated to higher temperatures without burning or decomposing. The carbonization step served to convert the insulating polymer nanofibers into conducting amorphous carbon fibers and precipitate noble metal nanoparticles. Variation of the independent processing parameters of electrospinning and heat treatment permitted experimentation with dependent variables such as fiber thickness, electrode thickness, particle size, and electrochemical activity.

Several methods and experimental apparatus were used to characterize the microstructure, physical properties, and electrochemical properties of the nanofibers. Micro and nanostructure characterization methods included SEM, XRD, TEM, and XANES. The physical property of bulk conductivity was measured using a microprobe station. Electrochemical activity was determined through testing samples with CV, RDE, and in a PEM fuel cell.

The SEM inspected the microstructure of the electrode and aided in determining the effect of altering electrospinning parameters. In agreement with literature, increasing PAN solution concentration increased viscosity, which raised the average fiber diameter. Defects such as spindling and spraying were imaged. Particle distribution was shown to be homogeneous across the electrode, as well as throughout the thickness. Cross-sectional SEM images facilitated the quantification of the relationship between solution volume spun and electrode thickness. The EDS of the SEM proved bright particles were in fact palladium.

The data of scans collected from the XRD led to the conclusion that no palladium oxide or crystallite carbon (graphite) could be found in significant amounts. Palladium, however, demonstrated significant crystallite peaks. Using the Scherrer Equation (3.6), average crystal size was calculated from the full width half max of the (111) palladium peak. Calculated average crystal size increased as heat treatment time and temperature increased. Crystal growth rate increased for higher temperatures.

The TEM allowed palladium particles on the order of nanometers to be resolved and a further understanding of particle formation was realized. TEM concurred with SEM and XRD to prove that particle size increased with heat treatment time and temperature. It was also discovered that particle size and growth rate were a function of fiber thickness. Particle counts in the TEM demonstrated a bimodal distribution of particle sizes, and assisted in explaining why average particle sizes were closer to 10nm, while XRD average crystal size was typically around 50nm. The TEM adapted to allow hot stage in-situ TEM to be performed, which provided information on particle growth mechanisms. Particles became resolvable between 585 and 684 ^{o}C, and showed no evidence of migration, indicating Ostwald ripening was the growth mechanism. It should be noted that discrepancies existed between observations in the tube furnace and in the vacuum environment of the TEM. Cross-sectional TEM revealed how palladium particles nucleate within the fiber. High-resolution TEM was not able to detect any distinct graphite ordering of the carbon support, but indicated large palladium particles were comprised of multiple, smaller crystals.

The microprobe station established that electrode bulk resistivity was a function of heat treatment time and temperature. Higher temperatures and longer heat treatment times resulted in lower bulk resistivity. Typical resistivity values for samples carbonized at 900°C were on the order of 10^{-3} Ohm-m, and samples treated at 1000°C were on the order of 10^{-4} Ohm-m.

Electrochemical evaluation of the nanofiber electrode began with cyclic voltammetry. CV was able to determine the active electrochemical surface area of palladium to be 7.17 m^2/g catalyst. Commercial electrodes have typical ECA values of around $70m^2/g$ catalyst, however, there are other factors necessary to make a "good electrode." The commercial value for ECA was expected because smaller particles are typically found in platinum black. CV plots of various samples made evident that although numerous particles on the order of nanometers could be seen in TEM and should have yielded high ECA, the particles were not functional if they nucleated within the fiber and did not penetrate the carbon surface. This was confirmed by cross-sectional TEM. CV trends showed that as heat treatment time increased, activity decreased for electrodes with fiber diameters around 200nm. Growth of larger particles reduced active and geometrical surface area per unit weight of catalyst. However, for electrodes with average fiber diameters around 400nm, the opposite trend was noted, and increased heat treatment times led to increased activity. As particles grew within thick nanofibers, the larger particles became more exposed. Active surface area was proven to be a function of heat treatment time and temperature along with average fiber diameter. Thicker electrodes and higher loadings also led to increased activity, with all other variables held constant.

Electrochemical activity was also examined using RDE experiments. Using the rotating electrode is an oxygen saturated acidic solution permitted the oxygen reduction half reaction of a fuel cell to be investigated. Plotting the data obtained from RDE in Koutecky-Levich plots, limiting kinetic current was calculated. It was shown that for an sample 8PAN-0.22604Pd/C-900-Xmin-0.10368mg/cm2-6, with thinner fiber diameters (around 200nm), kinetic limiting current decreased with increased heat treatment time (and decreased electrochemically active area). It was also noted that as particles grew

and surface area per unit weight catalyst decreased, the average number of electrons shrunk from 4 to 2, indicating larger catalyst particles increasing the probability of peroxide formation, an inefficient electrochemical pathway.

Testing the electrodes in a PEM fuel cell taught how to build an MEA with the developed nanofiber electrode, in addition to testing its electrochemical performance. The MEA was built by cutting the nanofiber electrode and attaching it to the GDL with 30μL of 5wt.% Nafion solution and not hot pressing. The electrochemical results from the fuel cell testing of a typical electrode showed that maximum power of the nanofiber electrode was 0.166 W at 0.619 A/mg Pd, while the commercial E-TEK electrode operated with 0.877W at 2.26 A/mg Pt. The nanofiber electrode performed roughly 20% as well as the commercial technology, however, palladium was used in the nanofiber electrode, which has much lower activity than platinum. When compared on a catalyst cost basis, the carbon nanofiber electrode exhibited performance comparable to the E-TEK electrode. When taking manufacturing costs into account, the nanofiber electrode will be more attractive. It should also be noted that the electrode used was not completely optimized.

The final conclusion is that with further optimization or use of platinum salts, the technology developed of electrospinning carbon nanofiber elcectrodes can be utilized to fabricate a more economical electrode with unequivocal, superior performance to current technology.

6 PERSPECTIVES

The carbon nanofiber electrode decorated with noble metal nanoparticles has been shown to perform on-par with current commercial electrodes on a cost basis. To push this technology ahead so it has a clear advantage, the following techniques could be implemented. First, with the current experimental setup, further experimentation with electrodes of varying heat treatment times and temperatures, fiber thicknesses, and Pd/C ratios could be tested in the PEM fuel cell. A more complicated experiment would replace the single capillary with a concentric capillary tube, as seen in Figure 2-3b. By electrospinning a solution with a core of pure PAN and an outer shell containing palladium (II) acetate, the probability that particles nucleate near the surface of the nanofiber will be higher than the current method.

Electrospinning thinner electrodes has been attempted as a method of reducing loading but increasing Pd/C ratio. Alternative substrates, such as metal mesh and E-TEK's GDL without catalyst loading, have been used. A disadvantage to this process is that if not removed from the substrate prior to stabilization, the fibers mass loss contributes to large stresses which can fracture the fibers. Using aluminum foil as a substrate and then removing the fibers with a razor blade works well, but this procedure is limited to electrodes than can be handled and use solution volumes of 0.05 μL or more.

Electrospinning of several salts has been accomplished, and will be another method to improve electrode performance. Palladium (II) acetate was the dominant salt tested, however, parameters on electrospinning with platinum (IV) chloride and platinum (II) pentadienoate were also recorded to test feasibility. Conductivity of the solution greatly affects the electrospinning conditions. The solution of platinum (IV) chloride and PAN in DMF was highly conductive and difficult to spin. Platinum (II) pentadienoate, on the contrary, was very similar to palladium (II) acetate, but exhibited more spindling under the same electrospinning conditions. Studies of bimetallic catalysts have shown them to be more active and less prone to corrosion and poisoning than pure catalysts. The

incorporation of cobalt into platinum has shown to improve oxygen reduction reaction kinetics [65]. Electrospinning solutions of platinum and cobalt salts may lead to better activity.

The flexibility of the electrospinning process and variability of numerous parameters provides for numerous applications. The future of electrospinning technology with applications in electrochemistry looks promising.

7 APPENDICES

APPENDIX A. ESTIMATED NOBLE METAL LOADING

To get an approximate value for the amount of noble metal salt required in the solution, the following calculation was made. Several input criteria were necessary as shown in Table 7-1.

Table 7-1: Necessary input criteria assumptions for calculation of theoretical noble metal loading.

Variable	Assumed Value
Weight concentration of PAN	10wt.%
Total volume of DMF	25 mL
Assumed Fiber Morphology	Long, round cylinder
Estimated Fiber Diameter	Fixed at 300nm
Estimated particle diameter	Fixed at 5 nm
Estimated average distance between particles	Fixed at 50 nm

First, the weight of the DMF must be found:

$$(25\text{mL of DMF})\left(\frac{0.948\text{g}}{1\text{mL}}\right) = 23.7025\text{g} \tag{7.1}$$

The assumption has been made in Table 7-1 that the PAN is 10wt.% of the solution. Therefore, from the weight of DMF in Table 3-2, the following calculation was made for the weight of PAN:

$$\left(\frac{23.7025\text{g DMF}}{0.9}\right) = \left(\frac{m_{PAN}}{0.1}\right)$$
$$m_{PAN} = 2.6336\text{g} \tag{7.2}$$

With the density of PAN given in Table 3-2, the total volume of PAN can be calculated:

$$(2.6336\text{g PAN})\left(\frac{1ml}{1.184\text{g PAN}}\right) = 2.2243\text{ml PAN} \tag{7.3}$$

As Table 3-2 denotes, it was assumed that the nanofiber electrode was comprised of fibers that are cylindrical and 300nm in diameter. The assumption was made that electrode was made from one continuous fiber of length, *L*. This is portrayed below in Figure 7-1.

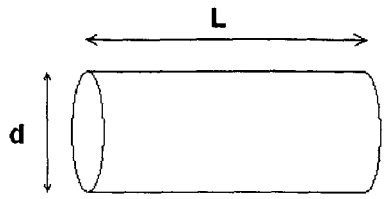

Figure 7-1: Schematic of a carbon nanofiber with diameter d and length L that makes up the electrode.

The total length, L, of the single-fiber electrode was found to be:

$$L = \frac{4V}{\pi d^2} = \frac{(2.2243\text{mL PAN})\left(\frac{1000\text{mm}^3}{1\text{ml}}\right)\times 4}{\pi(3\times10^{-4}\text{mm})^2} = 3.1467\times10^{10}\text{mm} \qquad (7.4)$$

Finding the total volume of palladium was the next step in solving for the amount of palladium salt needed in the solution. The assumption was made that particles are spherical and 5 nm in diameter, are made of pure palladium, and all palladium metal precipitates on the surface of the fiber. The volume of Pd occupied by a particle was:

$$V_{Pd.sphere} = \frac{4}{3}\pi r^3 = \left(\frac{4}{3}\right)(\pi)(5\times10^{-6}\text{mm})^3 = 5.2359\times10^{-16}\text{mm}^3/\text{sphere} \qquad (7.5)$$

Given that the fiber length was known and the diameter was assumed, the total surface area for palladium particle formation was calculated. A projection of the total fiber surface area is shown below in Figure 7-2.

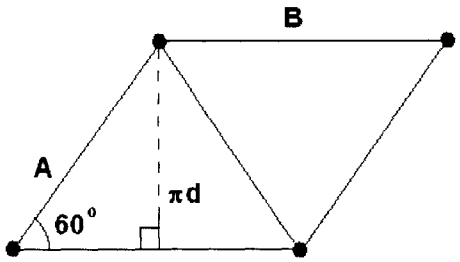

Figure 7-2: Diagram of the projected surface area of a fiber.

The value of B was simply the length of the total fiber, L, above in Equation 7.4.

$$B = L = 3.1467\times10^{10}\text{mm} \qquad (7.6)$$

The length of A was found using simple trigonometric relationships:

$$A = \frac{\pi d}{\sin 60^\circ} = 1.08827 \times 10^{-3}\,\text{mm} \tag{7.7}$$

The assumption was made that palladium particles were spaced 50 nm apart in any direction. This could be represented by equilateral triangles with particles at the vertices. Returning to Figure 7-2 of the projected surface area, the number of particles along segment A and B were estimated to determine the total number of particles on the surface of the fiber.

$$\text{Particles along A} = \frac{\text{A}}{50\text{nm}} + 1 = \frac{1.08827 \times 10^{-3}\,\text{mm}}{50 \times 10^{-6}\,\text{mm}} = 22.765 \tag{7.8}$$

$$\text{Particles along B} = \frac{\text{B}}{50\text{nm}} + 1 = 6.2934 \times 10^{4} \tag{7.9}$$

$$\text{Total \# of particles on fiber} = (\text{Points along A})(\text{Points along B}) = 1.43269 \times 10^{16}\,\text{particles} \tag{7.10}$$

The total volume of pure palladium is therefore:

$$\text{Total Volume of Palladium} = (\text{\# of particles})(\text{Volume of one Pd Sphere})$$
$$\text{Total Volume of Palladium} = 7.5014\text{mm}^3 \tag{7.11}$$

The calculation concludes by transforming the total volume of pure palladium into mass of palladium, and multiplying by the molecular weight ratio of Pd / Pd acetate to obtain the mass of palladium (II) acetate:

$$m_{Pd,pure} = \rho_{Pd,pure} V_{Pd,pure} = \left(12.0\text{g Pd/cm}^3\right)\left(7.5014\text{mm}^3\right)\left(\frac{1\text{cm}}{10^3\,\text{mm}^3}\right) \tag{7.12}$$

$$m_{Pd,pure} = 0.09001\text{g} \tag{7.13}$$

$$\%\ \text{of Pure Pd in PdAce Molecule} = {M_{Pd,pure}}/{M_{Molecule}} \tag{7.14}$$

$$m_{PdAce} = \frac{m_{Pd,pure}}{M_{Pd,pure}/M_{Molecule}} = \frac{0.09001\text{g}}{106.42 \times 3/673.46} = 0.19152\text{g} \tag{7.15}$$

APPENDIX B: EDS DATA

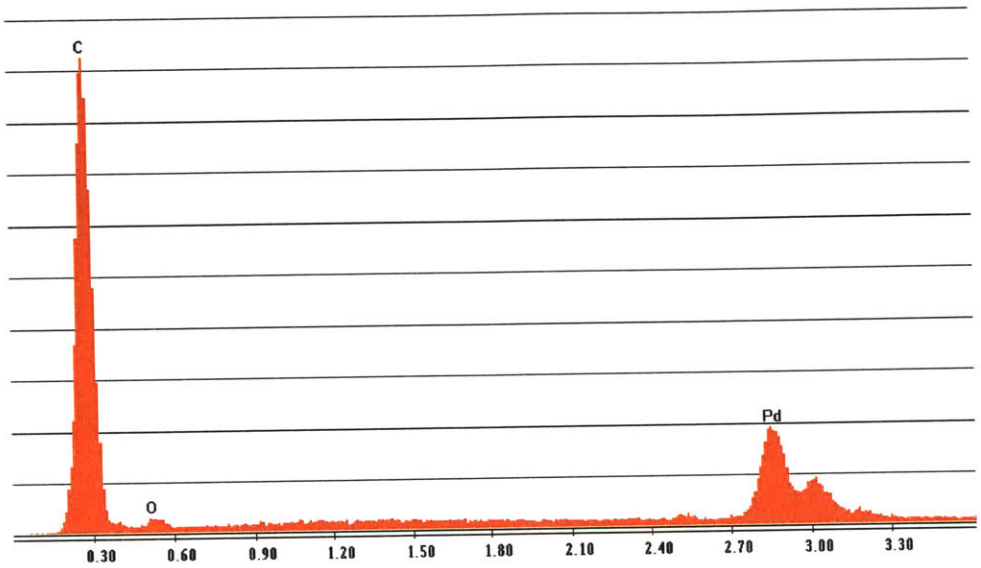

(a)

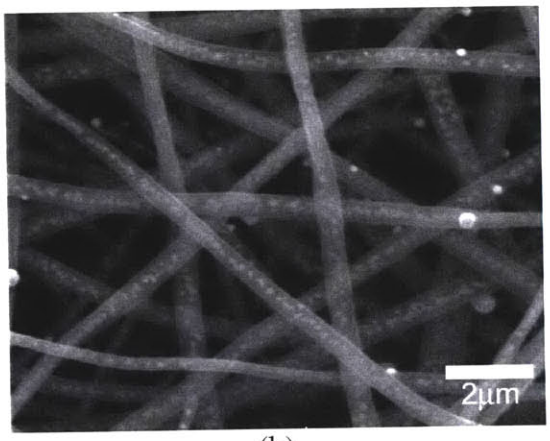

(b)

Figure 7-3(a,b): EDS Plot and image of selected area. The EDS plot shows that the only elements present in significant quantities are C, O, and Pd. Focusing on a single bright spot (particle) yields an EDS plot where the Pd peak is high.

APPENDIX C: ELECTROSPINNING DEFECTS UNDER SEM

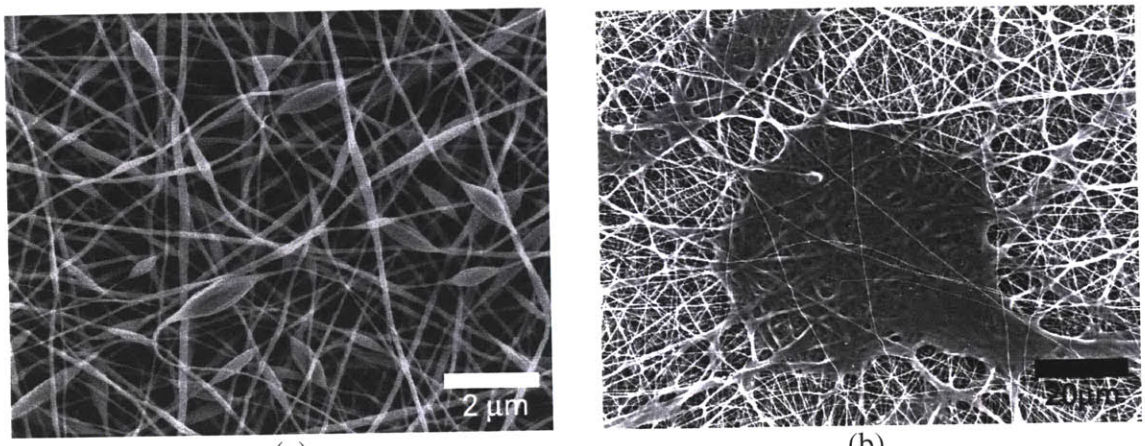

(a) (b)

Figure 7-4(a,b): Defects of electrospinning showing examples of fiber spindling or "beading" in (a) and the effects of spraying, when the jet becomes unstable and moves upwards into the capillary tube, in (b). These effects must be avoided to maximize carbon surface area.

APPENDIX D. ADDITIONAL XRD DATA

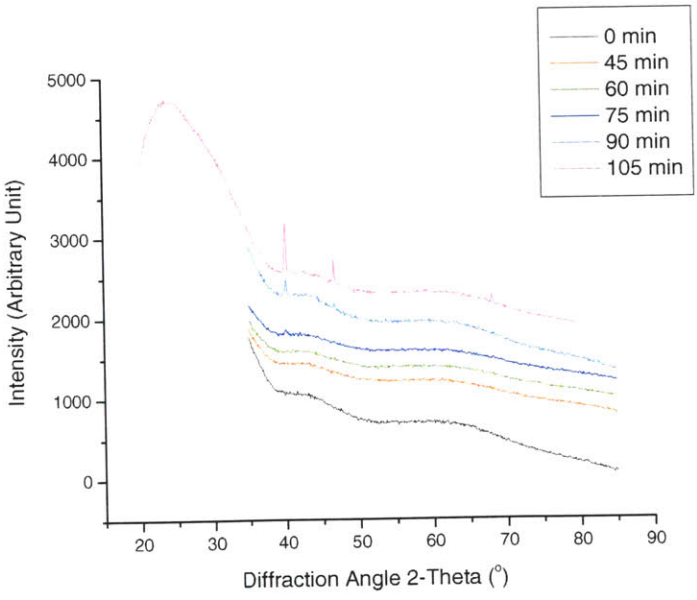

Figure 7-5: XRD scans of sample 8PAN-0.02488Pd/C-800-15min-0.03041mg/cm2-8 at 800°C for varying times.

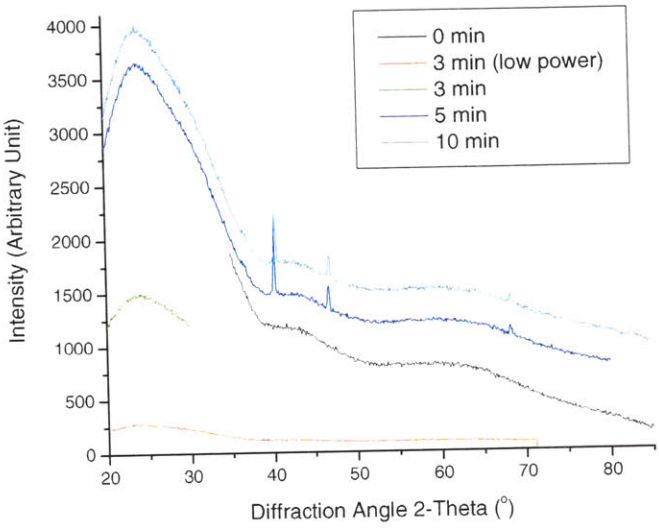

Figure 7-6. XRD scans of sample 8PAN-0.02488Pd/C-1000-15min-0.03041mg/cm2-8 at 1000°C for varying times.

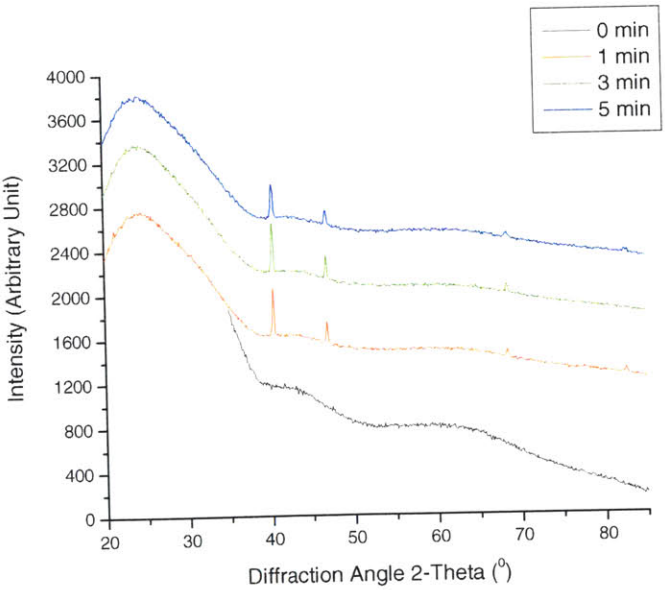

Figure 7-7. XRD scans of sample 8PAN-0.02488Pd/C-1100-Xmin-0.025913mg/cm2-5 at 1100°C for varying times.

APPENDIX E. TEM PARTICLE COUNTS

Data analysis of TEM images of sample 8PAN-0.02488Pd/C-900-Xmin-0.03041mg/cm2-8 yielded histograms of the number of particles in each quantized bin of particle diameters. The histograms were shown below in Figure 7-8.

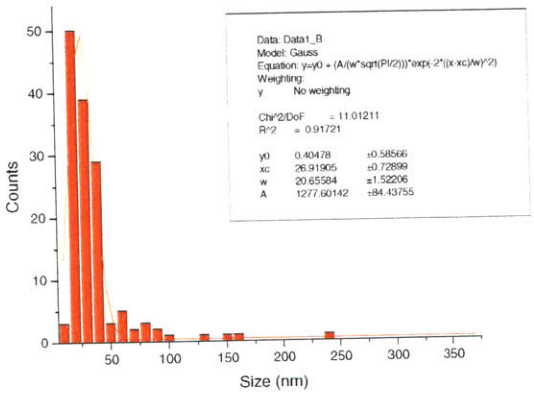

(a)

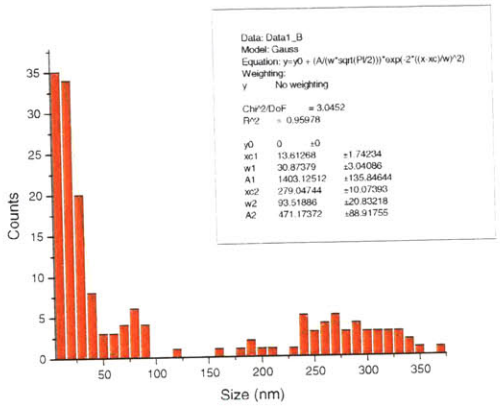

(b)

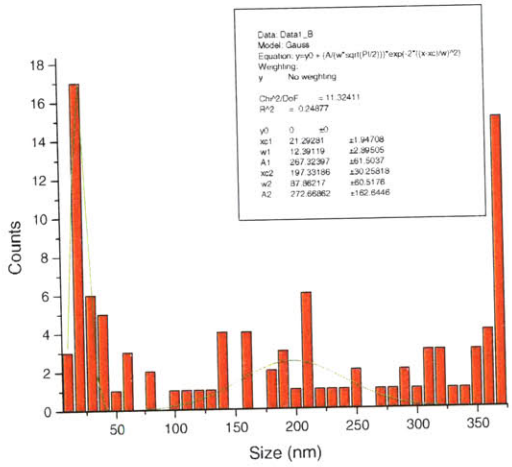

(c)

Figure 7-8 (a-c): Histogram plots of particle size counts for samples 8PAN-0.02488Pd/C-900-Xmin-0.03041mg/cm2-8 for increasing heat treatment times of 15, 30, and 45 minutes with bin sizes of 10nm. The data in (b) and (c) was fit with a bi-modal Gaussian curve. The last bar on the right side of the x-axis represented particles greater than 360nm in diameter. Particle counts below 10nm were not accurate. These plots correspond to the same sample in the XRD data represented by squares in Figure 4-8.

Trends showed that as heat treatment time increased from 15 to 30 minutes, a second Gaussian peak appeared with diameter greater than 100nm. After 30 minutes of heat treatment, a bi-modal distribution was distinct. After 45 minutes in the tube furnace, there were many larger particles, and the second distribution is less easily defined.

Table 7-2 summarizes the results of the analysis of average crystal sizes from sample 8PAN-0.02488Pd/C-900-Xmin-0.03041mg/cm2-8. The trend of increasing diameters as a function of heat treatment time is demonstrated and consistent.

Table 7-2: Table summarizing the calculated average diameters for sample 8PAN-0.02488Pd/C-900-Xmin-0.03041mg/cm2-8 at heat treatment times of 15, 30, and 45 minutes. The XRD Crystal Size (XS) data are from the sample represented with black squares in Figure 4-8.

HT Time (min	$d_{ave,n}$ (nm)	$d_{ave,vol}$ (nm)	XRD XS (nm)
15	30.865	165.35	55.29
30	93.018	297.03	59.16
45	185.47	365.89	64.09

There are several important points to note about the values in Table 7-2. Concerning the experimental error, the particle counts below 10nm were not reliable due to the non-optimized use to the TEM during imaging. The lack of high numbers of particles between 0-10nm in diameter shifted the calculated average diameters from particle counts to much greater values than what the actual value might be. Particles were found and imaged as randomly as possible. Larger values of average diameters from the histograms in Figure 7-8 were possibly the result because larger particles were easier to find and image under TEM. As demonstrated in the High Resolution TEM section, larger particles were often made up of multiple crystals.

In addition to misleading evidence due to particles of multiple crystal size, differences between reported average crystal sizes from XRD data and the calculated values of $d_{ave,n}$ and $d_{ave,vol}$ could be illustrated and explained by Figure 4-11 and the following example, using sample 9PAN-0.13416Pd/C-900-15min-0.07851mg/cm2.

The volume weighted average was always much greater than the numerical average, as seen in when comparing Equation (4.5) to Equation (4.7), as well as the values in Table 7-2. There were discrepancies between the XRD data and the calculated particle diameters. In sample 9PAN-0.13416Pd/C-900-15min-0.07851mg/cm2, the XRD result for average crystal size of 45nm was much closer to the volume weighted average, $d_{ave,vol}$, of 53.44nm. However, in sample 8PAN-0.02488Pd/C-900-Xmin-0.03041mg/cm2-8 as seen in Table 7-2, all of the values for $d_{ave,n}$ were closer to the XRD results. The difference between histograms of samples 9PAN-0.13416Pd/C-900-15min-0.07851mg/cm2 and 8PAN-0.02488Pd/C-900-Xmin-0.03041mg/cm2-8 was that the former had a large particle/small particle ratio of 1.474/1580 while the latter had ratios much higher. As seen in Figure 7-8a, small particle counts were around 50, while large particle counts were around 3, indicating a large particle/small particle ratio of 3/50.

One explanation for the data in Table 7-2 is that for samples with a greater large particle/small particle ratio, the average crystal size from XRD was smaller than the volume averaged diameter because large particles often were comprised of multiple

crystals. Large particles of multiple crystals increased the numerical average diameter, but did not increase the XRD average crystal size. This effect was not seen as significantly in sample 9PAN-0.13416Pd/C-900-15min-0.07851mg/cm2 in Figure 4-11 because of the overwhelmingly large number of particles with diameters around 10nm. However, in Table 7-2, as heat treatment time increases, numerical average particle diameter increases much faster than XRD average diameter.

APPENDIX F. CALCULATION OF CATALYST SURFACE AREA FROM CV

The following calculation exemplifies how to determine surface area per unit mass of catalyst. Origin 7 software was used in peak analysis and could calculate the area underneath the first hydrogen adsorption peak. The area in Figure 4-28 was:

$$Q = 1.063 \frac{mA}{cm^2} s = 1063 \mu C / cm^2 \tag{7.16}$$

where Q is the charge per unit area electrode. Assuming coverage of one hydrogen atom per palladium surface atom, the theoretical total amount of charge that can be held by pure, atomically smooth palladium, was 255 mC/cm^2, according to Wan et al. [66]. The roughness factor was defined as:

$$RF = \frac{\text{Area of Real Pd}}{\text{Area of Electrode}} = \frac{\text{Charge per Area of Real Pd}}{\text{Charge per Area of Theoretical Pd}} = \frac{Q}{255} \tag{7.17}$$

where Q is the charge per unit area electrode. The RF of sample 8PAN-0.22604Pd/C-900-30min-0.10368mg/cm2-6 was calculated as:

$$RF = \frac{1063 \mu C / cm^2}{255 \mu C / cm^2} = 4.17 \tag{7.18}$$

Knowing sample 8PAN-0.22604Pd/C-900-30min-0.10368mg/cm2-6 had a loading of 0.10368 mg/cm^2, the mass of noble metal on the electrode was:

$$m_{Pd} = (Loading) \times (ElectrodeArea) = \left(0.10368 \frac{mg}{cm^2 electrode}\right)\left(\pi * 0.25^2\right) cm^2 = 0.020357 mgPd \tag{7.19}$$

Finally, the roughness factor could be multiplied by the real area of the entire electrode to find the electrochemically active surface area, and then divided by the mass of palladium to find the active area per gram of catalyst:

$$\frac{RF \times ElectrodeArea}{m_{Pd}} = \frac{4.17 \times \pi (0.25cm)^2 \left(\frac{1m^2}{1 \times 10^4} \right)}{2.0357 \times 10^{-5} gPd} = 4.02 m^2 / gPd \qquad (7.20)$$

This result was reported in Table 4-1.

REFERENCES

1. D. Halliday, R. Resnick, J. Walker, *Fundamentals of Physics* (John Wiley & Sons, Inc., New York, ed. 5th, 1997), vol. 1.
2. *Electrical Energy*, http://en.wikipedia.org/wiki/Electrical_energy (2005).
3. *Annual Energy Review - Long Term History*, www.eia.doe.gov (2005).
4. L. Brush, in *EDN Power Technology*. (March 2005) pp. 8-10.
5. A. Bindra, *http://powerelectronics.com/news/power_fuel_cells_ready/* (Sept 16 2003).
6. J. Larmine, A. Dicks, *Fuel Cell Systems Explained* (John Wiley & Sons., West Sussex, England, ed. 2nd, 2003).
7. D. Linden, T. B. Reddy, *Handbook of Batteries* (McGraw Hill, New York, ed. 3rd, 2002).
8. E. Clive, D. S. Truck, *Modern Battery Technology* (1991).
9. K. Kinoshita, *Electrochemical Oxygen Technology* (John Wiley & Sons, Inc., New York, NY).
10. E. G. Services, I. Parsons, S. A. I. Corporation, *Fuel Cell Handbook* (DOE, Morgantown, West Virginia, ed. 5th, 2002).
11. Dupont, *http://www.dupont.com/fuelcells/products/nafion.html* (2004).
12. S. S. Kocha, in *Handbook of Fuel Cells - Fundamentals, Technology, and Applications* W. Vielstich, H. A. Gasteiger, A. Lamm, Eds. (John Wiley & Sons, Ltd., 2003), vol. 3.
13. S. R. Samms, S. Wasmus, R. F. Savinell, *Journal of the Electrochemical Society* **143**, 1498-1504 (MAY, 1996).
14. S. C. Barton, *Electrochimica Acta* **50**, 2145-2153 (MAR 15, 2005).
15. Kitco. (2004).
16. I. Ballard Power Systems, *Fuel Cell Technology road map* (http://www.ballard.com/be_informed/fuel_cell_technology/roadmap, 2004).
17. R. H. Borgwardt, *Transportation Research Part D-Transport and Environment* **6**, 199-207 (MAY, 2001).
18. TIAX, "Cost Analysis of Fuel Cell System for Transportation" (TIAX, LLC, 2001).
19. A. Formhals. (USA, 1934).
20. J. Doshi, D. H. Reneker, *Journal of Electrostatics* **35**, 151-160 (AUG, 1995).
21. I. Dogu, *Textile Research Journal* **45**, 521-532 (1975).
22. A. Frenot, I. S. Chronakis, *Current Opinion in Colloid & Interface Science* **8**, 64-75 (MAR, 2003).
23. E. W. Weisstein, in *http://scienceworld.wolfram.com/physics/EarnshawsTheorem.html*. (Wolfram Research, 2005), vol. 2005.
24. Y. M. Shin, M. M. Hohman, M. P. Brenner, G. C. Rutledge, *Polymer* **42**, 9955-9967 (DEC, 2001).
25. D. Halpern, J. B. Grotberg, *Journal of Fluid Mechanics* **492**, 251-270 (OCT 10, 2003).
26. M. M. Hohman, M. Shin, G. Rutledge, M. P. Brenner, *Physics of Fluids* **13**, 2201-2220 (AUG, 2001).

27. D. S. Lee, *Journal of Physics a-Mathematical and General* **36**, 573-583 (JAN 17, 2003).
28. G. Srinivasan, D. H. Reneker, *Polymer International* **36**, 195-201 (FEB, 1995).
29. J. M. Deitzel, J. Kleinmeyer, D. Harris, N. C. B. Tan, *Polymer* **42**, 261-272 (JAN, 2001).
30. W. S. Lee, S. M. Jo, S. G. Go, S. W. Chun. (Korea Institute of Science and Technology (Seoul, KR), US, 2003).
31. D. H. Reneker, H. Q. Hou, R. Rangkupan, J. D. Lennhoff, *Abstracts of Papers of the American Chemical Society* **226**, U425-U425 (SEP, 2003).
32. B. Chu, B. Hsiao, D. Fang. (The Research Foundation at State University of New York (Stony Brook, NY), USA, 2004).
33. D. H. Reneker. (The University of Akron (Akron, OH), USA, 2003).
34. Z. C. Sun, E. Zussman, A. L. Yarin, J. H. Wendorff, A. Greiner, *Advanced Materials* **15**, 1929-+ (NOV 17, 2003).
35. Z. H. Sun, D. H. Reneker, *Abstracts of Papers of the American Chemical Society* **225**, U662-U663 (MAR, 2003).
36. J. T. McCann, D. Li, Y. N. Xia, *Journal of Materials Chemistry* **15**, 735-738 (2005).
37. H. Fong, I. Chun, D. H. Reneker, *Polymer* **40**, 4585-4592 (JUL, 1999).
38. S. Koombhongse, W. X. Liu, D. H. Reneker, *Journal of Polymer Science Part B-Polymer Physics* **39**, 2598-2606 (NOV 1, 2001).
39. Y. S. Kang, H. Y. Kim, Y. J. Ryu, D. R. Lee, S. J. Park, *Polymer-Korea* **26**, 360-366 (MAY, 2002).
40. D. H. Reneker, I. Chun, *Nanotechnology* **7**, 216-223 (SEP, 1996).
41. X. Fang, D. H. Reneker, *Journal of Macromolecular Science-Physics* **B36**, 169-173 (1997).
42. S. Zarkoob, R. K. Eby, D. H. Reneker, S. D. Hudson, D. Ertley, W. W. Adams, *Polymer* **45**, 3973-3977 (MAY 13, 2004).
43. I. Chun, D. H. Reneker, H. Fong, X. Y. Fang, J. Dietzel, N. B. Tan, K. Kearns, *Journal of Advanced Materials* **31**, 36-41 (JAN, 1999).
44. H. Fong, D. H. Reneker, *Journal of Polymer Science Part B-Polymer Physics* **37**, 3488-3493 (DEC 15, 1999).
45. J. S. Kim, D. H. Reneker, *Polymer Engineering and Science* **39**, 849-854 (MAY, 1999).
46. D. J. Smith, D. H. Reneker. (The University of Akron (Akron, OH), USA, 2004).
47. Z. H. Chen, M. D. Foster, W. S. Zhou, H. Fong, D. H. Reneker, R. Resendes, I. Manners, *Macromolecules* **34**, 6156-6158 (AUG 28, 2001).
48. W. X. Liu, M. Graham, E. A. Evans, D. H. Reneker, *Journal of Materials Research* **17**, 3206-3212 (DEC, 2002).
49. D. H. Reneker, W. Kataphinan, A. Theron, E. Zussman, A. L. Yarin, *Polymer* **43**, 6785-6794 (DEC, 2002).
50. E. H. Sanders, K. A. McGrady, G. E. Wnek, C. A. Edmondson, J. M. Mueller, J. J. Fontanella, S. Suarez, S. G. Greenbaum, *Journal of Power Sources* **129**, 55-61 (APR 15, 2004).
51. G. L. Bowling, J. Matthews, D. G. Simpson, E. R. Kenawy, G. E. Wnek, paper presented at the The Fiber Society Spring 2001 Conference, Raleigh, NC 2001.

52. H. Q. Hou, D. H. Reneker, *Abstracts of Papers of the American Chemical Society* **225**, U662-U662 (MAR, 2003).
53. H. Q. Hou, D. H. Reneker, *Advanced Materials* **16**, 69-+ (JAN 5, 2004).
54. M. M. Demir, M. A. Gulgun, Y. Z. Menceloglu, B. Erman, S. S. Abramchuk, E. E. Makhaeva, A. R. Khokhlov, V. G. Matveeva, M. G. Sulman, *Macromolecules* **37**, 1787-1792 (MAR 9, 2004).
55. D. H. Reneker, G. Chase, D. J. Smith. (The University of Akron (Akron, OH), USA, 2003).
56. D. Ziegler, K. Senecal, C. Dew, L. Samuelson, paper presented at the The Fiber Society Spring 2001 Conference, Raleigh, NC 2001.
57. D. D. L. Chung, *Carbon Fiber Composites* (www.knovel.com, 1994).
58. M. Jain, A. Abhiraman, *Journal of Materials Science* **22**, 278-300 (1987, 1987).
59. T. H. Ko, S. C. Liau, M. F. Lin, *Journal of Materials Science* **27**, 6071-6078 (NOV 15, 1992).
60. Y. Wang, J. J. Santiago-Aviles, R. Furlan, I. Ramos, *Ieee Transactions on Nanotechnology* **2**, 39-43 (MAR, 2003).
61. P. K. Gallagher, M. E. Gross, *Journal of Thermal Analysis* **31**, 1231-1241 (1986).
62. B. D. Cullity, *Elements of X-Ray Diffraction* (Addison-Wesley Publishing Company, Inc., Reading, MA, ed. 2nd, 1978).
63. M. Islam, B. Ammundsen, D. Jones, J. Roziere, in *Materials for Lithium-Ion Batteries*. (Kluwer Academic Publishers, Netherlands, 2000) pp. 279-292.
64. C. Gabrielli, P. P. Grand, A. Lasia, H. Perrot, *Journal of the Electrochemical Society* **151**, A1937-A1942 (2004).
65. J. L. Fernandez, D. A. Walsh, A. J. Bard, *Journal of the American Chemical Society* **127**, 357-365 (JAN 12, 2005).
66. L. J. Wan, T. Suzuki, K. Sashikata, J. Okada, J. Inukai, K. Itaya, *Journal of Electroanalytical Chemistry* **484**, 189-193 (APR 17, 2000).